Dissertation zur Erlangung des Doktorgrades

der Fakultät für Chemie und Pharmazie

der Ludwig-Maximilians-Universität München

Beryllates as Functional Materials

Tobias Giftthaler

aus

Dingolfing, Deutschland

2023

Erklärung

Diese Dissertation wurde im Sinne von § 7 der Promotionsordnung vom 28. November 2011 von Herrn Prof. Dr. Wolfgang Schnick betreut.

Eidesstattliche Versicherung

Diese Dissertation wurde eigenständig und ohne unerlaubte Hilfe erarbeitet.

München, den 06.11.2023

.....

Tobias Giftthaler

Dissertation eingereicht am:	07.11.2023
1. Gutachter:	Prof. Dr. Wolfgang Schnick
2. Gutachter:	Prof. Dr. Hubert Huppertz
Mündliche Prüfung am:	06.12.2023

Für meine Familie

Aus niedriger Häuser dumpfen Gemächern,
Aus Handwerks- und Gewerbesbanden,
Aus dem Druck von Giebeln und Dächern,
Aus der Straßen quetschender Enge,
Aus der Kirchen ehrwürdiger Nacht
Sind sie alle ans Licht gebracht.

Johann Wolfgang von Goethe (Faust I)

Danksagung

Zunächst möchte ich mich bei Herrn Prof. Dr. Wolfgang Schnick bedanken, für die Möglichkeit, die vorliegende Arbeit in seinem Arbeitskreis anfertigen zu können. Die gegebene Freiheit, das Forschungsthema nach eigenen Vorstellungen zu gestalten und das Verständnis für spannende, aber riskante Synthesen sind nicht selbstverständlich. Die technische und analytische Umgebung bot die perfekte Basis zur Umsetzung neuer Ideen. Auch die Möglichkeit der Teilnahme an nationalen wie internationalen Tagungen war ein wichtiger Bestandteil dieser Promotion.
Insbesondere möchte ich mich aber für die menschliche und persönliche Unterstützung bedanken, ohne welche die Anfertigung der vorliegenden Arbeit schlichtweg nicht möglich gewesen wäre. Ihre fachliche Anleitung sowie Ihre unaufgeregte Art und Rücksichtnahme haben trotz aller Rückschläge meinen Glauben an dieses Projekt erhalten.

Bei Herrn Prof. Hubert Huppertz möchte ich mich für die Übernahme des Koreferats bedanken, sowie für die Gastfreundlichkeit auf dem Obergurgl-Seminar für Festkörperchemie. Das Anbieten dieser Tagung stellt eine tolle Chance für uns jungen Wissenschaftler dar, unsere Forschung in legerem Umfeld fachlich kompetent einordnen zu lassen.

Bei Herrn PD Dr. Constantin Hoch möchte ich mich sowohl für die Teilnahme am Rigorosum danken, als auch für die Betreuung der vorangegangenen Masterarbeit. Ich habe viel von Dir gelernt und bin Dir für jedes Gespräch, auch noch während der Promotion, sei es fachlich wie nicht fachlich, dankbar.

Herrn Prof. Oliver Oeckler danke ich für die Bereitschaft an der Prüfung teilzunehmen und für die stets positive Kooperation.

Herrn Prof. Hans-Christian Böttcher und Frau Prof. Silvija Markic möchte ich ebenso dafür danken, Teil meiner Prüfungskommission zu sein.

Des Weiteren danke ich meinen Kooperationspartnern, Dr. Philipp Strobel, Dr. Peter Schmidt, Volker Weiler, Dr. Arthur Haffner, Dr. Thomas Bräuniger, Robert Calaminus und Frau Prof. Bettina Lotsch, die einen wesentlichen Beitrag zu meiner Forschung geleistet haben.

Bei Herrn Christian Minke, Herrn Wolfgang Wünschheim, Herrn Thomas Miller, Dr. Dieter Rau, Dr. Peter Mayer, Herrn Michael Gayer und Frau Olga Lorenz möchte ich mich für die

Unterstützung im technischen und organisatorischen Bereich bedanken, sowie für die Anfertigung zahlreicher Analytik.

Bei meinen Praktikanten Herrn Sebastian Reiner, Herrn Andreas Neuer und Herrn Can Gülen möchte ich mich für ihren hervorragenden Beitrag zu meiner Arbeit bedanken. Ich wünsche Euch nur das Beste auf Eurem jeweiligen weiteren Weg.

Bei den Arbeitskreisen Schnick, Lotsch, Hoch und Johrendt möchte ich mich für die tolle Arbeitsumgebung und Stimmung während meiner gesamten Promotion bedanken. Es ist schön, nicht nur Arbeitskollegen, sondern Freunde um sich zu haben.

Mein besonderer Dank gilt diesbezüglich meinen Labor- und Schreibstubenkollegen Drs. Anna-Katharina Hatz, Eva-Maria Wendinger, Fabian Keßler Jonathan Sappl, Sascha Dums, Philipp Bielec, Timotheus Hohl, Lucien Eisenburger sowie Frau Amalina Buda, Frau Jennifer Steinadler, Herrn Reinhard Pritzl, Herrn Georg Krach, Herrn Sebastian Ambach und Herrn Marwin Dialer. Dazu natürlich auch den Drs. Lisa Gamperl, Christian Maak, Mathias Mallmann, Frau Mirjam Zipkat, Herrn Thanh Chau und Herrn Florian Engelsberger „von gegenüber“. Ich habe die Zusammenarbeit und auch das private Zusammensein mit Euch allen sehr genossen.

Frau Stefanie Schneider und Frau Sophia Wandelt danke ich für die Unterstützung im Rahmen des gemeinsamen Zieleinlaufs.

Bei Dr. Stefan Rudel und Dr. Simon Kloß möchte ich mich herzlich für die Freundschaft sowie für die fachliche Unterstützung deutlich über das normale Maß hinaus bedanken.

Dr. Peter Wagatha danke ich dafür, mir aktiv viele Fragen beantwortet zu haben, von denen ich nicht wusste, dass ich sie stellen muss und dafür auch nach der Promotion an mich gedacht zu haben.

Bei Dr. Sebastian Vogel und Dr. Sebastian Wendl möchte ich mich für die jahrelange Freundschaft und Begleitung auf diesem ganzen Lebensabschnitt bedanken. Vielleicht finden wir die Cenote Azul noch und vielleicht werden wir irgendwann einen schönen Wenz zu schätzen wissen. Die Hoffnung stirbt zuletzt. Viel Glück von Herzen, Euch und Euren Familien.

Stellvertretend für die Lehrkräfte, die mich für Naturwissenschaften begeistert haben, möchte ich mich bei Frau Petra Schupke, Herrn Mathias Bätz und Herrn Dr. Axel Goldberg bedanken.

Meinen Freunden und meiner „Zweit-Familie“, den Achatz, gilt ein besonderer Dank. Ihr seid mir immer eine Heimat.

Zuletzt bleibt mir, meinen größten Dank an meine Familie zu richten. Insbesondere an meine Großeltern Margot, Alfred, Monika und Rudolf sowie meine Eltern Monika und Alwin und meine Schwester Nicole. Ihr hab mir diesen Weg ermöglicht und steht mir jederzeit zur Seite. Euer Beitrag kann gar nicht überschätzt werden, dieses Werk ist zu schmal, um ihn zu fassen. Kristin, danke für alles, was ich bin und sein werde. Ich freue mich über jeden Tag mit Dir, alles gemeinsam Erlebte und auf unsere gemeinsame Zukunft.

Tobias

Table of Contents

1 Introduction

1.1 The necessity for new materials in distribution, conversion and storage of energy

In 2015, with the Paris climate agreement, 175 states have declared the intention to fight global warming cooperatively.[1] Herein, the main focus lies on the reduction of CO_2 emission to zero. A main component in the transformation to net zero emission economy is the energy sector. Currently, 86 % of the emitted CO_2 is caused by the burning of fossil fuels.[2] To reduce the emitted CO_2, the pathway is to replace existing energy provision and refine all processes involved in application. However, with modern renewable energy sources as an alternative to fossil fuels, major obstacles emerge in the distribution, storage and conversion of energy. Therefore, a set of uprising technologies will be applied to tackle these issues. With them comes an increasing demand for new materials.

In this context, three fields of technology will be of relevance for this contribution: indoor illumination, displays and solid state batteries.

In the illumination sector, currently responsible for 16 % of the used electricity in the US, the technology of choice is the light emitting diode (LED).[3] The most efficient form of LEDs for illumination application is the inorganic phosphor converted LED (pcLED). The applied phosphor materials, especially in the red spectral region, are subject to current research and represent a broad range of optimization possibilities.[4]

In displays for consumer electronics, of which smartphones account for over 7 billion worldwide, several competing technologies are applied to date.[5] One of these, the pcLED backlit LCD, might be the solution for the future. Here, in contrast to illumination, green emitting phosphors are the main objects of current research.[6, 7]

In 2022 11 % of the total electricity in Germany was provided by photovoltaics.[8] For the storage of renewable energy technologies, all solid state batteries gained traction in recent years. Particularly regarding the switch from lithium to the more earth-abundant sodium, this technology requires new, highly efficient electrolyte materials.[9, 10]

In all three fields, the necessity of new functional materials grows with increasing application. This, in turn, creates a demand for solid state compounds with new properties, which can be met by expanding the structural chemistry through the usage of additional elements. To address these challenges, an additional framework building cation can be introduced: Beryllium.

1.2 Beryllium – The Element of Choice

1.2.1 Natural occurrence, properties and technical relevance of beryllium

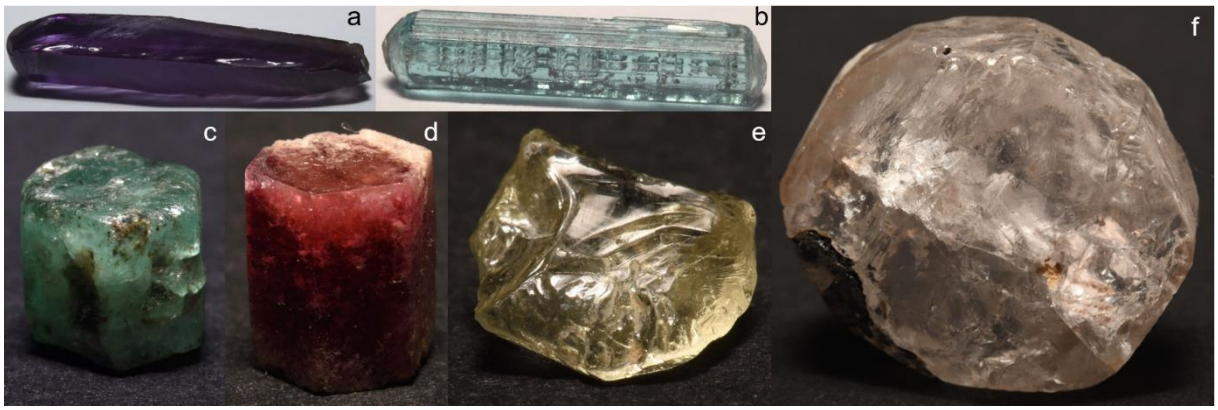

Figure 1 Pictures of selected beryllium containing gemstones. a Alexandrite, **b** Aquamarine, **c** Emerald, **d** Morganite, **e** Chrysoberyl, **f** Phenakite.

Why would one even want to deal with beryllium?
Beryllium, the fourth element of the periodic table, is neither very common, it makes up for only 46 ppbw of the earth, nor is it extremely high melting (Θ = 1287 °C) or of peculiar appearance.[11, 12] Nonetheless, it shows very distinctive properties making it suitable for high-tech applications. The technically most important one, its low density, is commonly utilized in aerospace. Combined with its high stiffness and low thermal expansion coefficient, this resulted in the notable application as mirror material of the James Webb Space Telescope.[13]
Because of the low X-ray absorption coefficient of elemental beryllium, it is also used as window material in X-ray tubes. Additionally, its large neutron scattering radius enables application as a neutron mirror in nuclear devices.[14, 15]

However, beryllium does not occur on earth in elemental form, due to its high oxygen affinity. Some of the most abundant beryllium containing minerals are the oxides beryl ($Be_3Al_2Si_6O_{18}$), bertrandite ($Be_4Si_2O_7(OH)_2$), phenakite (Be_2SiO_4) and chrysoberyl ($Al_2[BeO_4]$).[15] Furthermore, melilite ($(Ca,Na)_2(Mg,Al)[Si_2O_7]$) is known to incorporate larger quantities of beryllium substituting Mg or Al. As illustrated in Figure 1, the incorporation of color centers as $Fe^{2+/3+}$ and Cr^{3+} in beryllates leads to various color characteristics.[16] This makes beryllium containing minerals common gemstones.[14]

The oxide BeO is the most technical relevant Be containing compound. Its large band gap combined with high thermal conductivity makes it a suitable electric insulator for

miniaturized semiconductor elements. With respect to the large neutron scattering radius of Be atoms, BeO is applied as moderator material in nuclear reactors.[15]

1.2.2 Obstacles in Beryllium Application

Most chemists refrain from beryllium chemistry due to its characterization as one of the most toxic non-radioactive elements.[17] But, where does this evaluation come from and why could it be necessary to revisit beryllium and its supposed toxicity?
The toxicity of beryllium, its compounds and especially its dusts were subject to investigations due to two major beryllium induced medical conditions occurring subsequent to Be or BeO handling.[15] The first, acute pulmonary inflammation (pneumonitis), is presumably caused by exposition to high quantities of beryllium containing compounds. In particular, absorption of dusts is suspected to induce this severe inflammation of lung tissue, which can be fatal. The second, chronic beryllium disease (CBD or berylliosis), is assumably caused by either exposition to high doses of beryllium for a short period of time or lower doses over a long time. After years of latency, berylliosis leads to granulomatous changes in lung tissue, comparable to the effects of asbestos induced silicosis. Additionally to these main effects on the human health, beryllium is considered as a carcinogenic compound.

However, the toxicity of beryllium seems to be more complex than assumed. Recent studies on immune responses to beryllium and statistical analyses of beryllium expositions indicate that beryllium “toxicity” should rather be considered as an autoimmune condition or allergic hypersensitivity and find no evidence for acute toxicity.[18-21] The classification as carcinogenic is also being reevaluated, as beryllium shows no proven carcinogenicity in humans.[22]
Aggregated for preparative solid state chemistry, this is no deferral of basic safety techniques. This only shows that beryllium and its compounds must be handled with great precaution but can be applied in a safe manner. The preparative work in closed vessels under exclusion of air and moisture (*Schlenk*-technique) is a standardized method for solid state chemists.[23] It enables secure handling of low quantities of beryllium, as the risk of exposition is minimized.

In upscaling the production of beryllium containing compounds, an additional aspect has to be considered. The aforementioned large neutron scattering radius of beryllium and the resulting application in nuclear fusion ordnance (*H-bombs*) leads to an intentionally globally limited availability of beryllium metal. This can be circumvented by the usage of beryllium

oxide as a starting material, but is an obstacle in samples where beryllium nitride, synthesized from beryllium metal, is required.[24]

1.3 Beryllium and Silicon

When looking into a new or vastly unexplored substance class, it is worth finding analogies to well-established chemistry and application as a starting point.
As illustrated by the characterization of Be and Si as lithophile and therefore, the broad variety of minerals with Be^{2+} and Si^{4+} as interchangeable network building cations these two elements have a lot in common.[25] The main analogy in solid state chemistry is the nearly identical ionic radius of Be^{2+} and Si^{4+} in tetrahedral coordination.[26, 27]
To understand the possible structures, properties and applications of (nitrido-)beryllates, it is necessary to understand the chemistry behind the applications of related silicates.

1.3.1 (Oxo-)nitridosilicates as LED Phosphors

The technical relevance of (oxo-)nitridosilicates results mainly from their application as ceramic light converters, also known as phosphors, in LED devices. Phosphors are ceramics applied atop of light emitting semiconductor chips, as shown in Figure 2. These chips, mostly $Ga_{1-x}In_xN$, emit UV to blue light with high efficiency.[28]

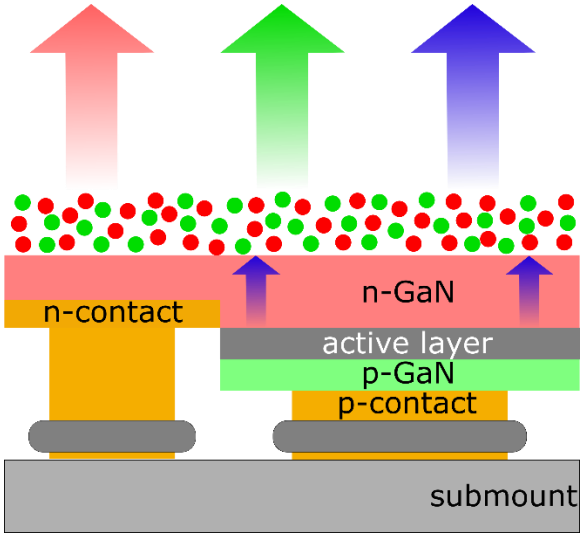

Figure 2 Schematic illustration of a state of the art 2pcLED. Blue light is emitted by a thin-film, flip-chip LED and converted by red and green phosphors. The blue, green and red emission add to a white color impression. Adapted from Ref.[6]

In most commercially available phosphors, an anionic network incorporates so called "activator ions". These ions, like $Eu^{2+/3+}$, Ce^{3+} or Mn^{4+}, absorb blue light, emitted by the LED chip itself and emit light with increased wavelengths.[29] The underlying process is illustrated in a configuration coordination diagram for the most commonly used activator Eu^{2+} (Figure 3).[30] The absorption of high-energy radiation, UV or blue light, leads to the excitation of electrons from a 4*f* ground level to an excited 5*d* level. From there, the electron can fall back to the ground state by emission of energy in a radiative or non-radiative manner. The desired radiative relaxation emits light of longer wavelength. Therefore, the absorbed high energetic light is converted to lower energies. The energy difference between excitation and emission is called Stokes shift and can be described by Equation 1.[31, 32]

$$E_{\text{Stokes}} = 2\,S \cdot \hbar\omega \qquad (1)$$

Accordingly, the Stokes shift is proportional to *S*, the Huang-Rhys parameter, and ω, the angular vibration frequency. ω is influenced by the molar mass of the host atoms. Typically, a higher mass leads to smaller frequencies. The Huang-Rhys parameter *S* is given by the number of phonons that are involved in the excitation and is therefore a measure of the electron-phonon coupling. It highly depends on the rigidity of a host structure. As shown in Figure 3, higher rigidity leads to smaller Stokes shifts and the technologically desired lowered probability of non-radiative decays.[30, 33]

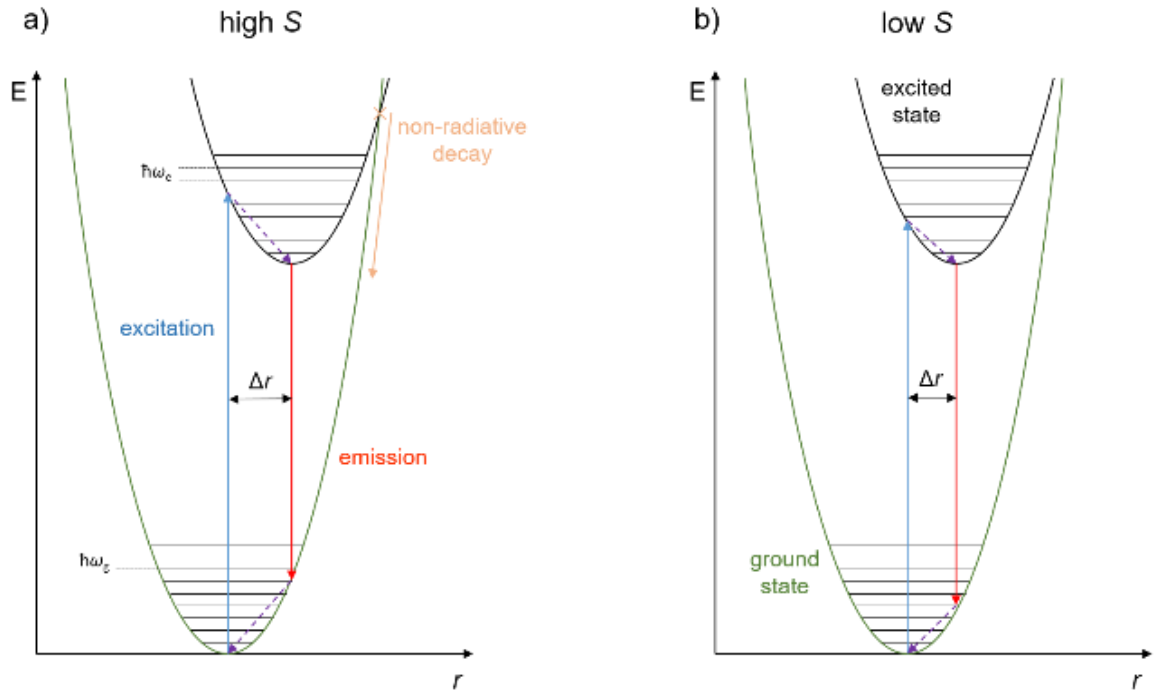

Figure 3 Configurational coordinate diagram. The configurational coordinate diagram shows electron energy in respect to a schematic coordinational radius, that represents the mean distance between an activator ion and its ligands. a) The absorption of a high energy photon leads to excitation (blue arrow) of an electron from the ground state (green parabola) to an excited state (black parabola). After subsequent vibrational relaxation of the electron (violet dotted arrow), a photon of lower energy is emitted and the electron relaxes to the ground state (red arrow). Alternatively, a non-radiative decay is possible at the parabola intersection (orange arrow). The shifted radius corresponding to energetic minima (Δr) leads to a lowered energy difference in emission compared to excitation, known as the Stokes shift. b) Lower S, corresponding to higher network rigidity, leads to a smaller parabola offset (Δr) and therefore to a smaller Stokes shift and lower probability of non-radiative decays as the parabolas intersect at higher energy.[30, 33]

In a solid state compound, the energy of 5*d* orbitals of the activator Eu^{2+} is largely reduced in comparison to a free ion by the formation of covalent bonds to coordinating atoms. This is called the nephelauxetic effect. Additionally, due to the different shapes of *d* orbitals, their spatial position in relation to the ligands and the respective coordination polyhedra, the energy of 5*d* orbitals splits in the surrounding crystal field.[34] Following the scheme in Figure 4, it is evident that the energy needed for the 4*f*→5*d* transition is reduced. Therefore, the difference between ground state and excited state is vastly influenced by the coordination environment of the activator ion.

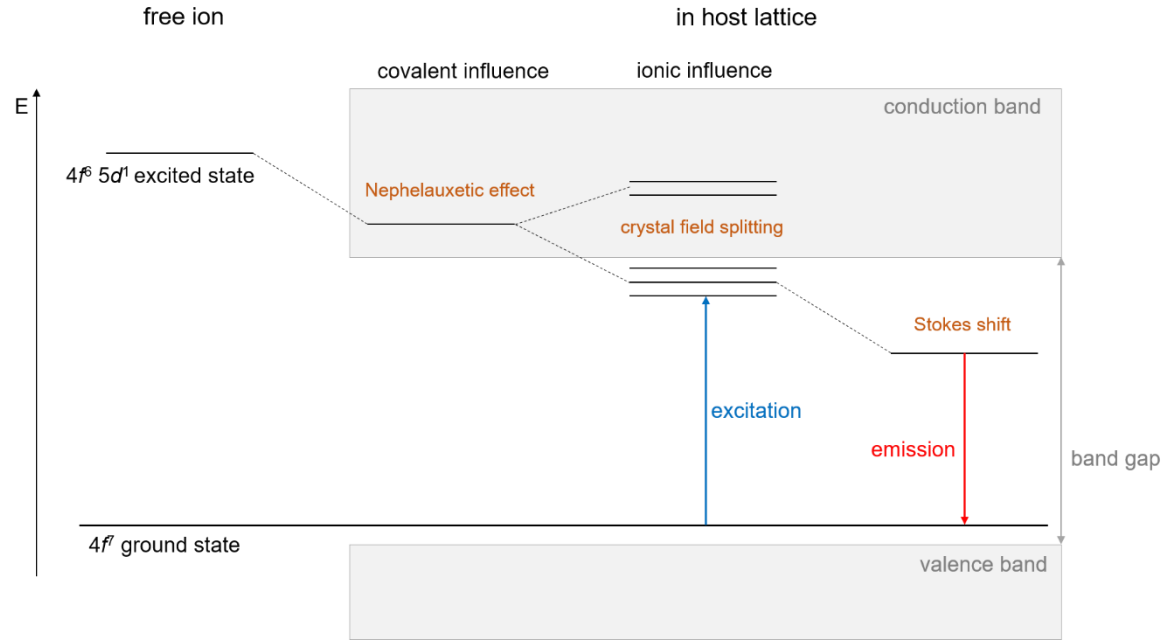

Figure 4 Schematic Eu^{2+} energy diagram. The energy difference between the $4f^7$ ground state and the $4f^6 5d^1$ excited state of a Eu^{2+} activator ion is reduced by a host lattice in comparison to a free ion.[35, 36]

The combination of highly symmetrical activator environments with coordination by N atoms, given in various nitridosilicates, leads to Eu^{2+} emission in the red spectral region. This spectral region was in focus of research for the last decade, as narrow band emitting red phosphors can contribute to better color rendition. This is quantified in a higher color rendering index (CRI). Coming from $Sr_2[Si_5N_8]:Eu^{2+}$, systems expressing the UCr_4C_4 structure type and therefore cuboidal N coordination of Eu^{2+} showed high potential for application.[37] $Sr[Mg_3SiN_4]:Eu^{2+}$ (SMS) as well as the derived $Sr[LiAl_3N_4]:Eu^{2+}$ (SLA) and $Sr[Li_2Al_2O_2N_2]:Eu^{2+}$ (SALON) show narrow band red emission with little to no infrared spillover, making them viable red phosphors for ambient lighting.[38-40] The latter already indicate the switch from Si to further network building cations as Al^{3+} and Li^+.

In comparison to LED devices for ambient lighting, displays require different emitters. The main objective is not to resemble sunlight as well as possible, quantified by a high CRI, but rather to be able to cover a large color gamut area (depicted in Figure 5). The color gamut represents all displayable colors by additive mixing of base emissions. It is commonly illustrated in a CIE 1931 or CIE 1976 diagram (*CIE – Commission internationale de l'éclairage*).[41] Hereby, the available color points of the LED span a triangular surface that covers the gamut area. Two of these color points, which are the blue light emitted by the

semiconductor chip itself as well as the red light converted by the phosphor $K_2SiF_6:Mn^{4+}$ (PSF), are already vastly optimized.[42] The third color point is generated by a green emitting phosphor. Here, widely used *β*-SiAlON:Eu^{2+} and green emitting $AESi_2O_2N_2:Eu^{2+}$(*AE* = Sr, Ba) showed applicability in displays.[43-46] However, their respective green emission leaves room for improvement. The desired, more saturated green light could be achieved by narrow-band emission at wavelengths around 525 nm.[6] This green emission and the resulting greater color gamut would cause a better color perception and thus a more vivid image representation.

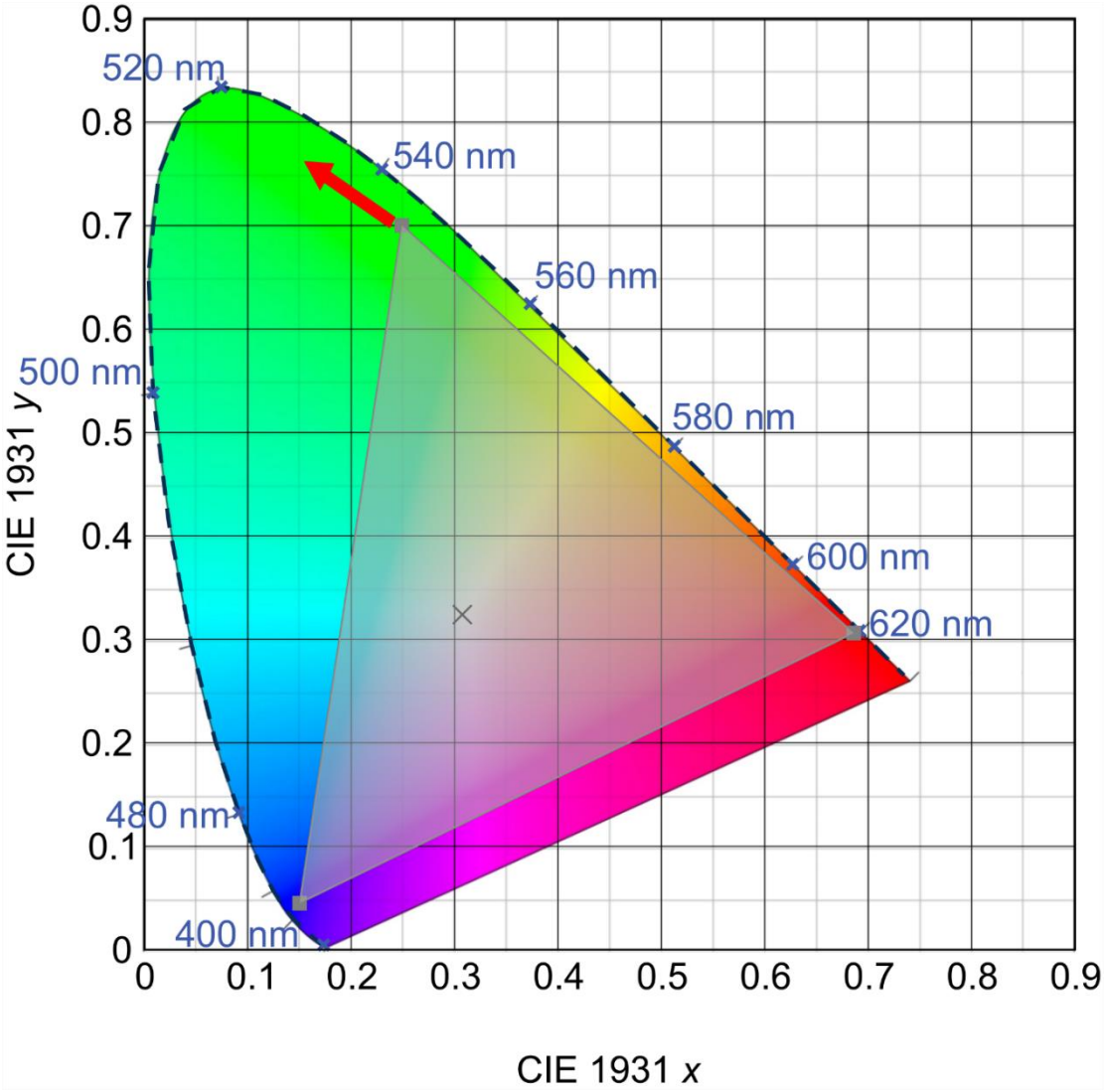

Figure 5 CIE 1931 Diagram. The color gamut (grey triangle) of a 2pcLED with PSF as red and *β*-SiAlON:Eu^{2+} as green phosphor. The covered area can be expanded in the green spectral region by application of an optimized green phosphor. The desired emission shift is highlighted by a red arrow.

1.3.2 Thiosilicates as Solid State Ion Conductors

Expanding the chemistry of silicates, the substitution of oxygen by the heavier homologue sulfur leads to thiosilicates. In analogy to many silicates and nitridosilicates, their sulfuric equivalents show luminescence upon doping with activator ions. However, due to their limited chemical stability, thiosilicates like $Ca_2SiS_4:Eu^{2+}$ and $BaLa_2Si_2S_8:Ce^{3+}$ have very limited industrial relevance.[47-49] Instead, the focus in thiosilicates is on the application as ion conductors. While silicates and nitridosilicates are investigated as high-temperature lithium ion conductors, thiosilicates like Li_2SiS_3 express lithium ion superconductivity at room temperature.[50-52] Following this pathway, related thiosilicates and –aluminates as $Li_{11}Si_2PS_{12}$ and $Li_{11}AlP_2S_{12}$ showed superionic conductivity as well.[53, 54] The in comparison to O^{2-} larger and therefore more polarizable anion S^{2-}, leads to a “softer” anionic network, which is discussed as beneficial for solid state ion conduction.[55, 56]

At the same time, the switch from lithium to more earth-abundant sodium as charge carrier leads to a demand of unprecedented solid electrolytes. Na_3PS_4 is characterized as one of the most promising materials in solid state sodium conduction.[57] In analogy to lithium ion conductors, the substitution of P by Si leads to Na_4SiS_4. In combination with the derived Na_5AlS_4, the system Na_4SiS_4-Na_5AlS_4 represents one of the latest steps towards softer host lattices in the expanded chemistry of thio-compounds.[58]

Obviously, a detailed oversight on solid state electrolytes is far beyond the scope of this chapter and can be found in literature.[59, 60] However, the requirement of solid state electrolytes with even softer, more polarizable lattices is evident. This can possibly be addressed by the usage of compared to Al^{3+}, Si^{4+} and P^{5+} lower charged Be^{2+} as a network building cation.

1.4 State of the Art in (Oxonitrido-)Beryllates

With the work of *Strobel* and *Elzer,* it was shown that beryllates could contribute to the class of LED phosphors.[61, 62] The trigonal planar coordination of Be^{2+}, as additional structural motif in comparison to Si^{4+} tetrahedra, combined with the lower charge of Be^{2+} enabled a variety of new, highly condensed structures. The highest achievable degree of condensation κ, representing the ratio of network building cation centers to surrounding anions, is given by the respective binary nitrides of network building cations. With κ (Si_3N_4) = 0.75 and κ (Be_3N_2) = 1.5, the condensation degree of $MBe_{20}N_{14}$ (κ = 1.43) shows the potential of beryllates to overcome nitridosilicates in terms of condensation. This high condensation resulted in a very rigid host lattice, and therefore in narrow, efficient luminescence of $AEBe_{20}N_{14}:Eu^{2+}$.[63] Even narrower emission could be achieved by the highly condensed $SrLi_2Be_4O_6:Eu^{2+}$.[64] Despite their high efficiency, either phosphors proved unfit for application, due to their relatively high beryllium content and the suboptimal emission wavelength. Therefore, the combination of beryllates and silicates, known from minerals, came to focus.

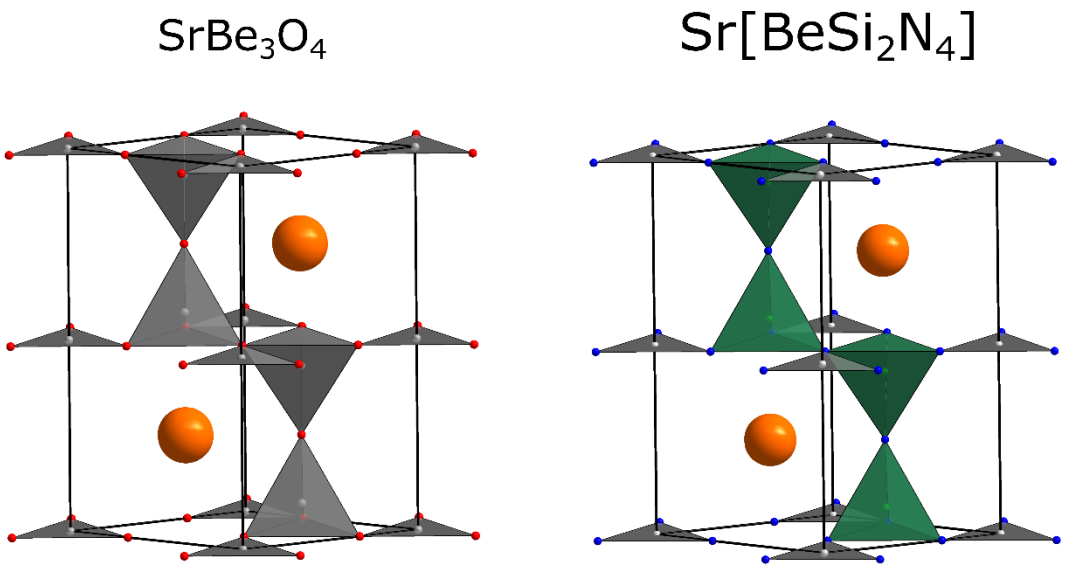

Figure 6 Crystal Structures of $SrBe_3O_4$ and the derived $Sr[BeSi_2N_4]$. The structure of $Sr[BeSi_2N_4]$ on the right is derived from $SrBe_3O_4$. Si^{4+} (green, in green tetrahedra) occupies the tetrahedral positions of Be^{2+} (grey, grey tetrahedra and triangles), while the trigonal planar coordinated sites remain exclusively Be^{2+}. O (red) is substituted by N (blue) for net charge neutrality. Sr (orange) is nine-fold coordinated in both compounds.

The nitridoberyllosilicate $Sr[BeSi_2N_4]:Eu^{2+}$ combines structural motifs from silicates and beryllates. It crystallizes in the $SrBe_3O_4$ structure type, with O substituted by N and Si occupying the tetrahedrally coordinated Be positions. $Sr[BeSi_2N_4]:Eu^{2+}$ shows anormal luminescence properties due to trapped exciton emission, making it a rather inefficient phosphor material.[65]

1.5 What can be realized with Beryllium? – Scope of this Thesis

Within this work, the focus lies on explorative solid state chemistry, using beryllium as a network building cation. New compounds were synthesized, characterized and their properties examined.

The Chapters 2 to 5 focus on the structural expansion of oxonitridosilicates by formal substitution of silicon by beryllium.
In Chapter 2 an unprecedented phosphor, $Ba[BeSiON_2]:Eu^{2+}$, is presented. Its structure is elucidated by a combination of analytical methods, in particular single crystal X-ray diffraction and solid state nuclear magnetic resonance spectroscopy. The subsequent discussion of applicability as green emitting phosphor in backlighting of liquid crystal displays is backed by a manufactured LED device and simulated color gamut coverage.
The third chapter is used to present $Sr[BeSi_2O_3N_2]:Eu^{2+}$, the second overall SiBeON phosphor. Its luminescence properties as well as its structure in the $LaSi_3N_5$ structure type are examined.
Chapter 4 deals with the system $AE[BeSi_2N_4]$ (*AE* = Ca, Sr, Ba) and the structural relations between the phases. Diffraction methods including X-ray diffraction on powder samples and single crystals as well as synchrotron radiation experiments are used to elucidate the structural impact of differently sized cations.
In Chapter 5 the oxoberyllate $Sr_3Be_2O_5$ is presented and the chemical relation to other strontium beryllates is discussed.
Chapter 6, however, introduces the unprecedented class of ternary thioberyllates with its first member Na_2BeS_2. The analogy between silicon and beryllium is expanded into sulfidic chemistry. Na_2BeS_2 is characterized and mixed electronic ionic conduction properties are measured.

Overall, this work aims to combine the realms of solid state chemistry: synthesis, crystallography and application with different emphasis in the respective chapters.

1.6 References

[1] United Nations Climate Change Conference, *Paris Agreement*, **2015**.

[2] P. Friedlingstein, M. O'Sullivan, M. W. Jones, R. M. Andrew, J. Hauck, A. Olsen, . . . S. Zaehle; Global Carbon Budget 2020, *Earth System Science Data* **2020**, *12*, 3269, doi:10.5194/essd-12-3269-2020.

[3] C. Elliott, M. Yamada, J. Penning, S. Schober, K. Lee, *Energy Savings Forecast of Solid-State Lighting in General Illumination Applications*, U.S. Department of Energy, Office of Energy Efficiency and Renewable Energy, Building Technologies Office, Washington, D.C., 2019.

[4] M. Pattison, M. Hansen, N. Bardsley, C. Elliott, K. Lee, L. Pattison, J. Tsao, *2019 Lighting R&D Opportunities*, U.S. Department of Energy, Office of Energy Efficiency and Renewable Energy, Building Technologies Office, Washington, D.C., **2020**.

[5] Radicati Group, *Mobile Statistics Report, 2021-2025*, **2021**.

[6] P. Pust, P. J. Schmidt and W. Schnick; A revolution in lighting, *Nat. Mater.* **2015**, *14*, 454, doi:10.1038/nmat4270.

[7] X. Zhang, H.-C. Wang, A.-C. Tang, S.-Y. Lin, H.-C. Tong, C.-Y. Chen, . . . R.-S. Liu; Robust and Stable Narrow-Band Green Emitter: An Option for Advanced Wide-Color-Gamut Backlight Display, *Chem. Mater.* **2016**, *28*, 8493, doi:10.1021/acs.chemmater.6b04107.

[8] Statistisches Bundesamt, Informationsportal Erneuerbare Energien, *Aktuelle Informationen: Erneuerbare Energien im Jahr 2022*, **2023**.

[9] J. B. Goodenough; Rechargeable batteries: challenges old and new, *J. Solid State Electrochem.* **2012**, *16*, 2019, doi:10.1007/s10008-012-1751-2.

[10] T. L. Kulova and A. M. Skundin; From lithium-ion to sodium-ion battery, *Russ. Chem. Bull.* **2017**, *66*, 1329, doi:10.1007/s11172-017-1896-3.

[11] N. Wiberg, E. Wiberg and A. F. Holleman, *Anorganische Chemie -Band 1 Grundlagen und Hauptgruppenelemente, Vol. 103*, De Gruyter, Berlin, **2016**, ISBN:978-3-11-026932-1

[12] C. Allègre, G. Manhès and É. Lewin; Chemical composition of the Earth and the volatility control on planetary genetics, *Earth. Planet. Sci. Lett.* **2001**, *185*, 49, doi:10.1016/s0012-821x(00)00359-9.

[13] NASA, https://webb.nasa.gov/content/about/faqs/facts.html, **2021**, (accessed: 20.10.2023).

[14] R. Puchta; A brighter beryllium, *Nat Chem* **2011**, *3*, 416, doi:10.1038/nchem.1033.

[15] K. A. Walsh, *Beryllium Chemistry and Processing*, ASM International, Materials Park, OH, **2009**, ISBN:0-87170-721-7

[16] H.-R. Wenk and A. Bulakh, *Minerals - Their Constitution and Origin*, Cambridge University Press, Cambridge, **2006**, ISBN: 978-0-521-82238-1

[17] O. Kumberger and H. Schmidbaur; Warum ist Beryllium so toxisch?, *Chem. Unserer Zeit* **1993**, *27*, 310, doi:10.1002/ciuz.19930270611.

[18] C. Strupp; Beryllium metal II. a review of the available toxicity data, *Ann. Occup. Hyg.* **2011**, *55*, 43, doi:10.1093/annhyg/meq073.

[19] A. P. Fontenot, M. T. Falta, J. W. Kappler, S. Dai and A. S. McKee; Beryllium-Induced Hypersensitivity: Genetic Susceptibility and Neoantigen Generation, *J. Immunol.* **2016**, *196*, 22, doi:10.4049/jimmunol.1502011.

[20] R. J. F. Berger, P. Håkansson and R. Mera-Adasme; A consistent model for the key complex in chronic beryllium disease, *Z. Naturforsch., B* **2020**, *75*, 413, doi:10.1515/znb-2020-0010.

[21] G. M. Clayton, Y. Wang, F. Crawford, A. Novikov, B. T. Wimberly, J. S. Kieft, . . . J. W. Kappler; Structural basis of chronic beryllium disease: linking allergic hypersensitivity and autoimmunity, *Cell* **2014**, *158*, 132, doi:10.1016/j.cell.2014.04.048.

[22] P. Boffetta, J. P. Fryzek and J. S. Mandel; Occupational exposure to beryllium and cancer risk: a review of the epidemiologic evidence, *Crit. Rev. Toxicol.* **2012**, *42*, 107, doi:10.3109/10408444.2011.631898.

[23] W. Schlenk and A. Thal; Über Metallketyle, eine große Klasse von Verbindungen mit dreiwertigem Kohlenstoff II, *Ber. Dtsch. Chem. Ges.* **1913**, *46*, 2840, doi:10.1002/cber.19130460356.

[24] M. v. Stackelberg and R. Paulus; Untersuchungen über die Kristallstruktur der Nitride und Phosphide zweiwertiger Metalle, *Z. Phys. Chem.* **1933**, *22B*, 305, doi:10.1515/zpch-1933-2226.

[25] V. M. Goldschmidt; The principles of distribution of chemical elements in minerals and rocks, *J. Chem. Soc.* **1937**, *0*, 655, doi:10.1039/jr9370000655.

[26] R. D. Shannon; Revised effective ionic radii and systematic studies of interatomic distances in halides and chalcogenides, *Acta Crystallogr., Sect. A* **1976**, *32*, 751, doi:10.1107/s0567739476001551.

[27] W. H. Baur; Effective Ionic Radii in Nitrides, *Crystallography Reviews* **1987**, *1*, 59, doi:10.1080/08893118708081679.

[28] N. C. George, K. A. Denault and R. Seshadri; Phosphors for Solid-State White Lighting, *Annual Review of Materials Research* **2013**, *43*, 481, doi:10.1146/annurev-matsci-073012-125702.

[29] C. C. Lin and R. S. Liu; Advances in Phosphors for Light-emitting Diodes, *J Phys Chem Lett* **2011**, *2*, 1268, doi:10.1021/jz2002452.

[30] W. M. Yen, S. Shionoya and H. Yamamoto, *Phosphor Handbook*, Taylor & Francis Group, Boca Raton, **2007**, ISBN:0-8493-3564-7

[31] G. G. Stokes; On the change of refrangibility of light, *Philos. Trans. R. Soc. London* **1852**, *142*, 463, doi:10.1098/rstl.1852.0022.

[32] M. de Jong, L. Seijo, A. Meijerink and F. T. Rabouw; Resolving the ambiguity in the relation between Stokes shift and Huang-Rhys parameter, *Phys. Chem. Chem. Phys.* **2015**, *17*, 16959, doi:10.1039/c5cp02093j.

[33] G. Blasse; On the Nature of the Eu^{2+} Luminescence, *Phys. Stat. Sol. (B)* **1973**, *55*.

[34] B. N. Figgis and M. A. Hitchman, *Ligand Field Theory and Its Applications*, Wiley, New York, **2000**, ISBN:978-81-265-2845-5

[35] S. Schmiechen, P. Pust, P. J. Schmidt and W. Schnick; Weißes Licht aus Nitriden, *Nachrichten aus der Chemie* **2014**, *62*, 847, doi:10.1002/nadc.201490285.

[36] L. Wang, R. J. Xie, T. Suehiro, T. Takeda and N. Hirosaki; Down-Conversion Nitride Materials for Solid State Lighting: Recent Advances and Perspectives, *Chem. Rev.* **2018**, *118*, 1951, doi:10.1021/acs.chemrev.7b00284.

[37] H. A. Höppe, H. Lutz, P. Morys, W. Schnick and A. Seilmeier; Luminescence in Eu^{2+}-doped $Ba_2Si_5N_8$: fluorescence, thermoluminescence, and upconversion, *J. Phys. Chem. Solids* **2000**, *61*, 2001, doi:10.1016/s0022-3697(00)00194-3.

[38] S. Schmiechen, H. Schneider, P. Wagatha, C. Hecht, P. J. Schmidt and W. Schnick; Toward New Phosphors for Application in Illumination-Grade White pc-LEDs: The Nitridomagnesosilicates $Ca[Mg_3SiN_4]:Ce^{3+}$, $Sr[Mg_3SiN_4]:Eu^{2+}$, and $Eu[Mg_3SiN_4]$, *Chem. Mater.* **2014**, *26*, 2712, doi:10.1021/cm500610v.

[39] P. Pust, V. Weiler, C. Hecht, A. Tucks, A. S. Wochnik, A. K. Henss, . . . W. Schnick; Narrow-band red-emitting $Sr[LiAl_3N_4]:Eu^{2+}$ as a next-generation LED-phosphor material, *Nat. Mater.* **2014**, *13*, 891, doi:10.1038/nmat4012.

[40] G. J. Hoerder, M. Seibald, D. Baumann, T. Schroder, S. Peschke, P. C. Schmid, . . . H. Huppertz; $Sr[Li_2Al_2O_2N_2]:Eu^{2+}$-A high performance red phosphor to brighten the future, *Nat. Commun.* **2019**, *10*, 1824, doi:10.1038/s41467-019-09632-w.

[41] Commission Internationale De L'Eclairage, *CIE 15:2004-Colorimetry*, **2004**. ISBN: 3-901906-33-9.

[42] L. Lv, X. Jiang, S. Huang, X. a. Chen and Y. Pan; The formation mechanism, improved photoluminescence and LED applications of red phosphor $K_2SiF_6:Mn^{4+}$, *J. Mater. Chem. C* **2014**, *2*, 3879, doi:10.1039/c4tc00087k.

[43] N. Hirosaki, R.-J. Xie, K. Kimoto, T. Sekiguchi, Y. Yamamoto, T. Suehiro and M. Mitomo; Characterization and properties of green-emitting β-SiAlON:Eu2+ powder phosphors for white light-emitting diodes, *Appl. Phys. Lett.* **2005**, *86*, 211905, doi:10.1063/1.1935027.

[44] J. Niu, G. Saito and T. Akiyama; A New Route to Synthesize β-SiAlON:Eu2+Phosphors for White Light-Emitting Diodes, *Applied Physics Express* **2013**, *6*, 042105, doi:10.7567/apex.6.042105.

[45] V. Bachmann, C. Ronda, O. Oeckler, W. Schnick and A. Meijerink; Color Point Tuning for $(Sr,Ca,Ba)Si_2O_2N_2:Eu^{2+}$ for White Light LEDs, *Chem. Mater.* **2009**, *21*, 316, doi:10.1021/cm802394w.

[46] J. A. Kechele, O. Oeckler, F. Stadler and W. Schnick; Structure elucidation of $BaSi_2O_2N_2$ – A host lattice for rare-earth doped luminescent materials in phosphor-converted (pc)-LEDs, *Solid State Sci.* **2009**, *11*, 537, doi:10.1016/j.solidstatesciences.2008.06.014.

[47] Y. Nanai, Y. Sakamoto and T. Okuno; Luminescence Properties of Rare-Earth-Doped Thiosilicate Phosphors on Silicon Substrate, *Jpn. J. Appl. Phys.* **2013**, *52*, doi:10.7567/jjap.52.04cg15.

[48] S. P. Lee, C. H. Huang, T. S. Chan and T. M. Chen; New Ce^{3+}-activated thiosilicate phosphor for LED lighting-synthesis, luminescence studies, and applications, *ACS Appl. Mater. Interfaces* **2014**, *6*, 7260, doi:10.1021/am500483j

[49] P. F. Smet, I. Moreels, Z. Hens and D. Poelman; Luminescence in Sulfides: A Rich History and a Bright Future, *Materials* **2010**, *3*, 2834, doi:10.3390/ma3042834.

[50] H. Yamane; Preparation of lithium silicon nitrides and their lithium ion conductivity, *Solid State Ionics* **1987**, *25*, 183, doi:10.1016/0167-2738(87)90119-6.

[51] A. D. Robertson, A. R. West and A. G. Ritchie; Review of crystalline lithium-ion conductors suitable for high temperature battery applications, *Solid State Ionics* **1997**, *104*, 1, doi:10.1016/s0167-2738(97)00429-3.

[52] W. Huang, N. Matsui, S. Hori, K. Suzuki, M. Hirayama, M. Yonemura, . . . R. Kanno; Anomalously High Ionic Conductivity of Li_2SiS_3-Type Conductors, *J. Am. Chem. Soc.* **2022**, *144*, 4989, doi:10.1021/jacs.1c13178.

[53] A. Kuhn, O. Gerbig, C. Zhu, F. Falkenberg, J. Maier and B. V. Lotsch; A new ultrafast superionic Li-conductor: ion dynamics in $Li_{11}Si_2PS_{12}$ and comparison with other

tetragonal LGPS-type electrolytes, *Phys. Chem. Chem. Phys.* **2014**, *16*, 14669, doi:10.1039/c4cp02046d.

[54] P. Zhou, J. Wang, F. Cheng, F. Li and J. Chen; A solid lithium superionic conductor Li11AlP2S12 with a thio-LISICON analogous structure, *Chemical Communications (Cambridge)* **2016**, *52*, 6091, doi:10.1039/c6cc02131j.

[55] K. Wakamura; Roles of phonon amplitude and low-energy optical phonons on superionic conduction, *Phys. Rev. B* **1997**, *56*, 11593, doi:10.1103/PhysRevB.56.11593.

[56] J. Souquet, E. Robinel, B. Barrau and M. Ribes; Glass formation and ionic conduction in the M_2SGeS_2 (*M* = Li, Na, Ag) systems, *Solid State Ionics* **1981**, *3-4*, 317, doi:10.1016/0167-2738(81)90105-3.

[57] M. Jansen and U. Henseler; Synthesis, structure determination, and ionic conductivity of sodium tetrathiophosphate, *J. Solid State Chem.* **1992**, *99*, 110, doi:10.1016/0022-4596(92)90295-7.

[58] S. Harm, A. K. Hatz, C. Schneider, C. Hoefer, C. Hoch and B. V. Lotsch; Finding the Right Blend: Interplay Between Structure and Sodium Ion Conductivity in the System Na_5AlS_4-Na_4SiS_4, *Front. Chem.* **2020**, *8*, 90, doi:10.3389/fchem.2020.00090.

[59] M. Ma, M. Zhang, B. Jiang, Y. Du, B. Hu and C. Sun; A review of all-solid-state electrolytes for lithium batteries: high-voltage cathode materials, solid-state electrolytes and electrode–electrolyte interfaces, *Mater. Chem. Front.* **2023**, *7*, 1268, doi:10.1039/d2qm01071b.

[60] Y. Zheng, Y. Yao, J. Ou, M. Li, D. Luo, H. Dou, . . . Z. Chen; A review of composite solid-state electrolytes for lithium batteries: fundamentals, key materials and advanced structures, *Chem. Soc. Rev.* **2020**, *49*, 8790, doi:10.1039/d0cs00305k.

[61] P. Strobel, *Narrow-band Emitting Phosphors for Solid-State Lighting*, LMU München, München, **2018**

[62] E. Elzer, *Nitridoberyllates and Nitridoberylloaluminates for Slid-State Lighting*, LMU München, München, **2022**

[63] E. Elzer, R. Niklaus, P. J. Strobel, V. Weiler, P. J. Schmidt and W. Schnick; $M Be_{20}N_{14}:Eu^{2+}$ (*M* = Sr, Ba): Highly Condensed Nitridoberyllates with Exceptional Highly Energetic Eu^{2+} Luminescence, *Chem. Mater.* **2019**, *31*, 3174, doi:10.1021/acs.chemmater.8b05133.

[64] P. Strobel, C. Maak, V. Weiler, P. J. Schmidt and W. Schnick; Ultra-Narrow-Band Blue-Emitting Oxoberyllates $AELi_2[Be_4O_6]:Eu^{2+}$ (*AE*=Sr,Ba) Paving the Way to Efficient RGB pc-LEDs, *Angew. Chem. Int. Ed.* **2018**, *57*, 8739, doi:10.1002/anie.201804721.

[65] P. Strobel, V. Weiler, P. J. Schmidt and W. Schnick; $Sr[BeSi_2N_4]:Eu^{2+}/Ce^{3+}$ and $Eu[BeSi_2N_4]$: Nontypical Luminescence in Highly Condensed Nitridoberyllosilicates, *Chem. Eur. J.* **2018**, *24*, 7243, doi:10.1002/chem.201800912.

2 Green-Emitting Oxonitridoberyllosilicate $Ba[BeSiON_2]:Eu^{2+}$ for Wide Gamut Displays

Tobias Giftthaler, Philipp Strobel, Volker Weiler, Arthur Haffner, Andreas Neuer, Jennifer Steinadler, Thomas Bräuniger, Simon D. Kloß, Stefan Rudel, Peter J. Schmidt and Wolfgang Schnick

Abstract: Light-emitting diodes (LEDs) producing pure, highly saturated colors are the industry standard for efficient backlighting of high-color gamut displays. Vivid color reproduction, matching the eye's perception of nature, is the central paradigm in the design of narrow-band emitting phosphors. To cover a wide range of naturally occurring color tones, expansion of the color gamut in the green spectral region, and therefore an advanced applicable green phosphor, is highly desired. Herein, the oxonitridoberyllosilicate $Ba[BeSiON_2]:Eu^{2+}$ showing outstanding narrow-band green emission (λ_{max} ≈526 nm with FWHM ≈1600 cm^{-1} (≈45 nm), $x = 0.212$, $y = 0.715$) when excited with InGaN-based blue LEDs is presented. High quantum efficiency and low thermal quenching (>90% rel. quantum efficiency at 100 °C) as well as excellent scalability make the material suitable for industrial application in high color-gamut LED displays. A prototype phosphor-converted-LED (pc-LED), with green-emitting $Ba[BeSiON_2]:Eu^{2+}$ and $K_2SiF_6:Mn^{4+}$ as red phosphor shows an extraordinary coverage in the CIE 1931 color space of 109% compared to the DCI-P3 standard, topping the widely applied β-SiAlON:Eu^{2+} phosphor (104%), making it suitable for use in phone displays, monitors, and television screens.

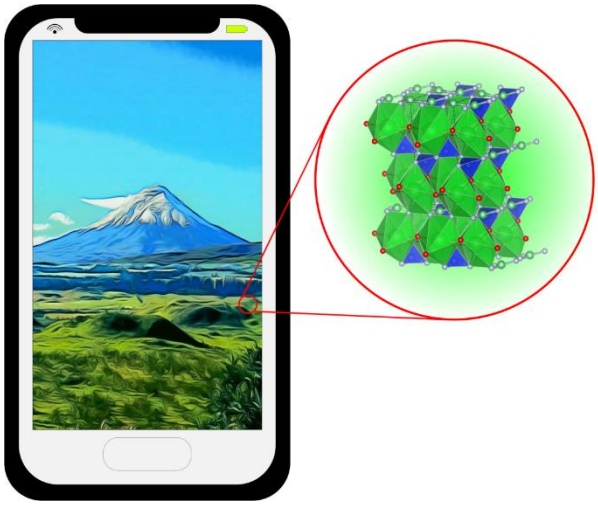

2.1 Introduction

In search for next generation displaying technologies direct emitting LEDs as organic LEDs (OLED) and inorganic mini and micro LEDs as well as quantum dot converted inorganic LEDs (QLED) and phosphor converted inorganic LEDs (pcLED) are competing for the lead in overall applicability. While organic-LED-based displays feature high color gamuts and are therefore often used in miniaturized displays, they have major drawbacks such as rather high energy consumption, limited luminance, and reduced front of screen brightness.[1-4] In contrast, inorganic semiconductor-based LEDs have a comparably low energy consumption and long lifespan, and are increasingly available as mini and micro LEDs either as direct emitters or as backlight for liquid crystal displays (LCD), which makes them suitable for miniaturized pixelated displays.[5-11] In application are either a combination of primary red, green, and blue LEDs or, more efficiently, a blue LED combined with color down-converters. In the latter, color conversion is usually achieved with quantum dots, which suffer from reliability challenges and achievable brightness, or with inorganic phosphors, which have high efficacies and are thus used in illumination devices.[12, 13] Commonly used phosphor converters are though broad band emitters and hence not all specific colors can be targeted individually at high efficiency, reducing color saturation.[14-18]

This leads to limited color gamuts in display technology making them inadequate for application, where the currently most advantageous combination for backlit LC displays, as defined above, features blue emitting InGaN primary LEDs with a combination of *β*-$SiAlON:Eu^{2+}$ phosphor for green emission and $K_2SiF_6:Mn^{4+}$ (PSF) for red emission.[19, 20] This combination still lacks in coverage of common standardized color spaces and Pointer's gamut, the representation of natural occurring colors, as well as in efficiency. Therefore, the development of green phosphors combining high quantum efficiency (QE) with strong blue light absorption and a narrow band emission with a maximum in the region of 530 nm is imperative to increase the gamut and color saturation enabling it to compete with current state-of-the-art displaying devices. Currently, no commercialized green phosphor fulfills all criteria and candidate materials under investigation such as Eu^{2+} doped oxonitridosilicates, lithosilicates, borates, alumolithonitridosilicates or manganese doped aluminates each suffer from low efficiency, insufficient stability, demanding synthetic accessibility or emission mismatch and are therefore not suitable to replace *β*-$SiAlON:Eu^{2+}$ in application.[21-33]

In the design of a new Eu^{2+}-based phosphor, the focus lies on the activator's coordination geometry and type of ligand, as it defines the desired excitation and emission

wavelengths.[34] The most promising materials classes in this field, i.e., silicates, alumosilicates, and lithosilicates, show a distinct structural motif in building corner sharing MO_4 tetrahedra connected via bridging O atoms. This leads to a broad diversity of possible structures, as linkages can be found in one, two, or all three dimensions resulting in chains, layers, or interconnected networks. The incorporation of nitrogen in silicates, hence, going from silicates to nitridosilicates, expands the variety of possible linkages from twofold coordinated oxygen to threefold or even higher coordinated nitrogen. Adding Be^{2+}, similar sized to Si^{4+}, increases the structural variety even further, as their coordination in either tetrahedral [BeX_4] or trigonal planar [BeX_3] building blocks create new structural motifs and hereby, new coordination geometries for activator ions, in this case, Eu^{2+}.[35-37] Generally, in coordination of Eu^{2+}, smaller distances, and ligands with stronger ligand fields typically lead to higher energetic splitting Eu:*5d* states and therefore, to lower energetic absorption transitions. This adds to the nephelauxetic effect, lowering the energies of Eu:*5d* states due to more covalent bonding characteristics. In this case, the substitution of O by N in a coordination sphere eventually leads to an emission shift towards the red spectral region for a given Stokes shift.

Here, we report the novel green emitting oxonitridoberyllosilicate phosphor $Ba[BeSiON_2]:Eu^{2+}$ (BBS), which we characterize regarding it's luminescence properties, chemical composition, and structure, showing that it is suitable for LEDs with high color gamut.

2.2 Results and Discussion

Synthesis and Chemical Analysis

The high-temperature synthesis of $Ba[BeSiON_2]:Eu^{2+}$ (BBS) yields an air and moisture resistant yellow-greenish powder, which dissolves slowly in diluted hydrochloric acid. The structure of BBS was solved and refined based on single-crystal X-ray diffraction data (SCXRD) and confirmed with Rietveld refinement of powder X-ray diffraction data (PXRD, Figure S1, Tables S1,S2, Supporting Information). The chemical composition was confirmed by a combination of energy dispersive X-ray spectroscopy (EDS) (averaged over eight datapoints: $Ba_{1.0}[BeSi_{0.9(1)}O_{1.1(3)}N_{2.0(5)}]$) and nuclear magnetic resonance spectroscopy (NMR) data. Since Be is hardly detectable by EDS, its presence was verified by NMR

measurements. The observed characteristic line shape of the central transition broadened by the quadrupolar interaction is in good agreement with the structural motif of trigonal planar coordination for the Be-site (details in Supporting Information).

Crystal Structure Determination

Ba[BeSiON$_2$] crystallizes in the orthorhombic space group Ama2 (no. 40) with lattice parameters a = 5.6366(3), b = 11.6363(7) and c = 4.9295(3) Å.[38] It exhibits [BeSiON$_2$]$^{2-}$ layers built by alternating chains of condensed trigonal planar [BeN$_3$]$^{7-}$ units and [SiON$_3$]$^{7-}$ tetrahedra. These tetrahedral chains show a strictly alternating up-down-up-down sequence, as shown in Figure 1. The chemically preferred occupation of the terminal position by O was also indicated by SCXRD refinement, as given with smaller interatomic distances compared to N-occupied positions.[39] All Ba^{2+} ions share one crystallographic site located between the [BeSiON$_2$]$^{2-}$ layers, sevenfold coordinated by four O and three N atoms forming a distorted pentagonal bipyramid. The interatomic distances are found between 2.64 and 2.83 Å for Ba–O and 2.95–2.99 Å for Ba–N, respectively. Further crystallographic details are given in the Tables S3,S4 (Supporting Information).

The crystal structure is closely related to that of Ba[Si$_2$O$_2$N$_2$] crystallizing in space group *Pbcn*, as shown in Figure 1.[40] but in Ba[BeSiON$_2$] every second [SiON$_3$]$^{7-}$ tetrahedron is replaced by a [BeN$_3$]$^{7-}$ unit.

The substitution leads to a reduction of the Si–Si distance between respective layers from 7.2 to 5.8 Å, while the degree of condensation κ (atomic ratio of tetrahedral centers to coordinating atoms) rises from 1/2 to 2/3. The coordination of Ba significantly changes from a cuboid shaped eightfold coordination by O in Ba[Si$_2$O$_2$N$_2$] to irregularly sevenfold coordination by O and N in BBS.

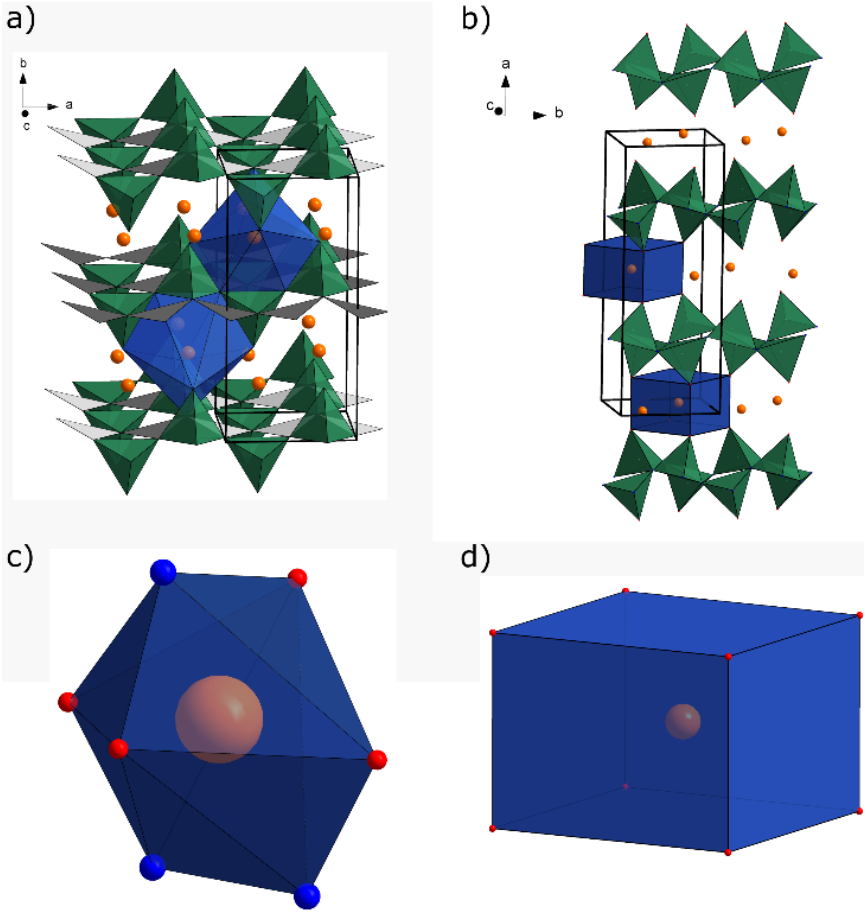

Figure 1. Comparison of schematic crystal structures of $Ba[BeSiON_2]:Eu^{2+}$ (left) to $BaSi_2O_2N_2$ (right). a) Layers of $[SiON_3]$-tetrahedra (green) and trigonal planar $[BeN_3]$-units (gray) stacked along [010] with Ba ions (orange) and their respective coordinational environment ions (blue), b) Layers of $[SiON_3]$-tetrahedra (green) stacked along [100] with Ba ions (orange) and their respective coordinational environment ions (blue), c) Sevenfold oxygen (red) and nitrogen (blue) coordinated Ba ions (orange) and their coordinational environment (blue) d) Eightfold oxygen (red) coordinated Ba ions (orange) and their coordinational environment (blue).

UV/Vis Spectroscopy

Diffuse reflectance UV-vis spectra of undoped samples were collected to determine the optical band gap of BBS. The collected reflectance spectra were converted to pseudo absorption spectra using the Kubelka-Munk-theory and displayed in a Tauc-plot (see Figure S5, Supporting Information).[41-42] The zero point of a linear data fit on the infliction point determined the, assumed direct, band gap to be around 4.0 eV. This is within the usual range for (oxo-)nitridic phosphors, but smaller than the band gap of $Ba[Si_2O_2N_2]$ at 4.8 eV.[40, 43]

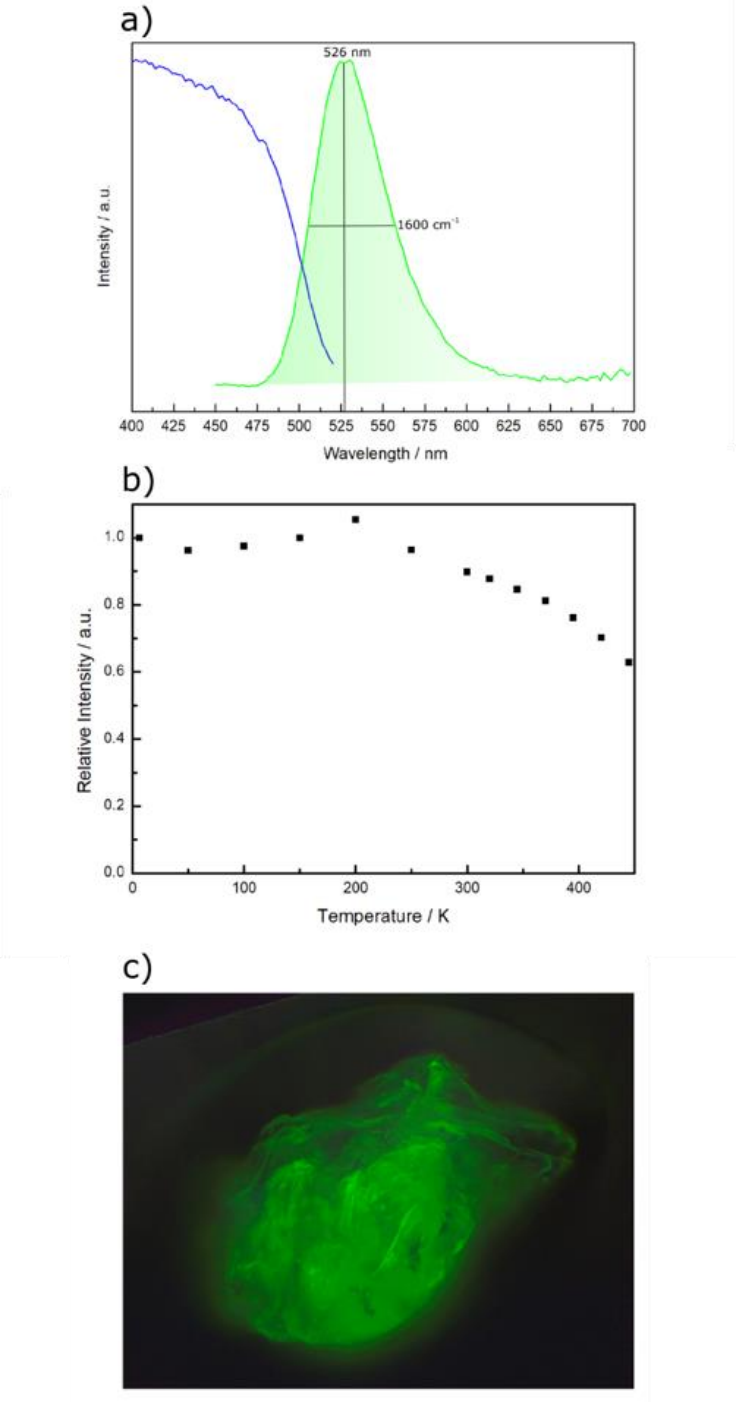

Figure 2. Luminescence of $Ba[BeSiON_2]:Eu^{2+}$. a) Excitation (blue) and emission (green) curves of selected particles of $Ba[BeSiON_2]:Eu^{2+}$, b) Thermal quenching behavior of $Ba[BeSiON_2]:Eu^{2+}$, normalized on the intensity at 6 K, c) Microscopic image of agglomerated crystals of $a[BeSiON_2]:Eu^{2+}$ under UV light.

Luminescence

The different coordination environments of Ba between $Ba[Si_2O_2N_2]$ and BBS, as shown in Figure S2 (Supporting Information), lead to different luminescence properties, as Eu^{2+} is assumed to replace Ba^{2+} statistically. BBS shows an emission maximum at a longer wavelength (526 nm) compared to 490 nm of $Ba[Si_2O_2N_2]:Eu^{2+}$, and therefore emits green light.[44]

BBS shows green luminescence under irradiation of UV to blue light, due to the Eu^{2+} $4f^7(^8S_{7/2})\rightarrow 4f^6(^7F)5d^1$ transition (see **Figure** 2c). Accordingly, the emission shows a maximum at 526 nm with a full width at half maximum (FWHM) of 45 nm (≈1600 cm^{-1}), as given in Figure 2a for BBS with 0.75% nominal dopant concentration. The additionally shown excitation curve drops significantly only in the spectral region beyond 475 nm. Thus, efficient excitation can be obtained with blue emitting primary LEDs. And the ideal excitation can be realized with an UV- or a blue LED chip (≈450 nm), as required for display backlighting applications. A variation of the dopant concentration leads to an emission shift (see Figure S6, Supporting Information), likely due to the influence of the different ionic radii of Eu^{2+} and Ba^{2+} on the host lattice.[35]

As given in Figure 2b the temperature-dependent photoluminescence emission intensity of BBS, defined as the ratio of emitted to absorbed photons normalized to the value at 6 K, decreases with temperature. With a maximum at 200 K, the relative QE is still above 90% at 300 K compared to the low temperature QE and contains more than 70% up to 400 K. The emission wavelength does not change during heating. Temperature dependent spectra are given in the supporting information (Figures S7,S8, Supporting Information). The internal quantum efficiency (IQE), representing the ratio of emitted to absorbed photons, was found to be up to 43% for as-synthesized samples. This can be further increased for industrial application by optimization of the synthetic process, as variation of the thermal parameters and mechanical treatment are highly influential on crystallite growth and therefore absorption and emission.

A green LED suitable for display backlighting application was built (depicted in **Figure** 3b) and relevant luminescence properties were measured. Hereby, the standard design for backlight LEDs was used. A blue emitting InGaN LED acts as primary emitter covered with a green emitting phosphor, in this case $BaBeSiON_2:Eu^{2+}$. For demonstration of applicability a simulation of the emitted light and applied filters is used to obtain the individual RGB spectra (see Figure S9, Supporting Information). Every given color displayable by this setup can be described as a combination of the three individually emitted color points via a coordinate in a CIE color diagram. The main goal in application is to widen the so-called

color gamut, hence, the coverage of predefined color spaces, focusing on the green spectral region, where a wider gamut is most beneficial. The color spaces used for benchmarking are the established NTSC color space developed for TV applications as well as the newer DCI-P3 and Rec.2020 focusing on modern displays.[45, 46]

When BBS (x = 0.212, y = 0.715) is used in combination with a blue emitting LED chip with PSF as red phosphor, the color gamut covers the visible spectrum (see Figure 3a) as well as 109.0% of the DCI-P3 standard (108.3% compared to NTSC, 80.2% to Rec.2020), as shown in Figure 3c. This marks a major increase compared to the 104.4% (103.7% NTSC) of the widely used standard green emitting phosphor *β*-SiAlON:Eu^{2+} in an equivalent configuration. This increase is due to coverage of a significantly wider variety of colors in the turquoise-green spectral region.

2.3 Conclusions

In conclusion, combination of narrow green emission (526 nm peak emission, FWHM = 1600 cm^{-1}) with chemical and thermal stability, as provided by Ba[BeSiON$_2$]:Eu^{2+}, is unmatched in phosphors for application in inorganic LED backlit LC displays with high color gamut. The straightforward synthesis from commercially available starting materials meets industrial requirements and gives room for even further improvements regarding the crystallite growth and therefore, the already outstanding emission properties. For further understanding of these emission properties, theoretical and detailed experimental examinations of the electronic structure will be reported in the near future.

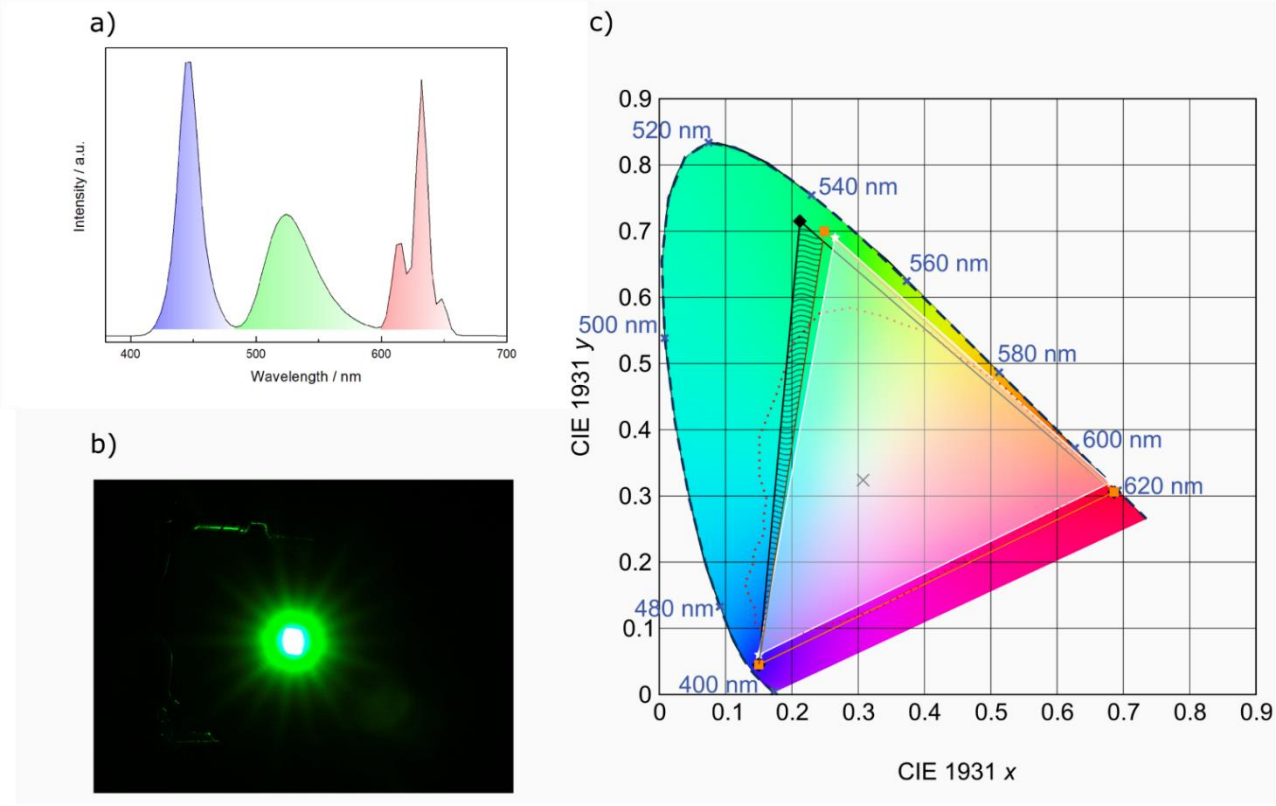

Figure 3. Emission of a LED chip with $Ba[BeSiON_2]:Eu^{2+}$. a) Simulated emission diagram of a InGaN LED (blue) with $Ba[BeSiON_2]:Eu^{2+}$ (green) and PSF (red). b) Image of a InGaN pcLED with $Ba[BeSiON_2]:Eu^{2+}$ c) CIE 1931 diagram of a display with a pcLED (BBS+PSF) as background light source. The black triangle being the covered gamut area, the orange triangle the covered area with *β*-SiAlON as green phosphor. The gained gamut coverage is given as the striped area. For reference Pointer's gamut (red dotted area) and DCI-P3 standard (white triangle) are given.

As energy consumption and longevity of electronics are a major concern, displays using mini-LED backlighting systems are advantageous compared to other backlighting technologies. However, already commercially available displays leave room for improvement regarding chromaticity and energy efficiency. Our material can help to improve the next generation of these displays, by reducing the percentage of color-filter erased wavelengths and therefore the overall energy loss. Furthermore, it expands the possible display color gamut especially in the very relevant green spectral region. This is crucial, as the human eye's sensitivity for green color shades is high and a variety of natural colors relies on an expanded green gamut for natural representation and leads to possible applications in displays, as in automotive or handheld devices, where wide gamut and natural color representation are highly desired. This is of particular significance, i.e., for photography and cinematography, which require high quality wide gamut displays.

In general, the incorporation of Be^{2+} as network building ion gives room for expanded research in phosphor materials, applying diversified structural motifs as a combination of trigonal planar and tetrahedral units and will prove beneficial in future phosphor design.

Further details of the crystal structure investigation(s) may be obtained from the Fachinformationszentrum Karlsruhe, 76344 Eggenstein-Leopoldshafen (Germany), on quoting the depository number CSD-2191356.

2.4 Acknowledgements

The authors thank *Dr. Constantin Hoch* for recording the single-crystal X-ray data, Dr. *Lisa Gamperl* for SEM imaging, *Mirjam Zipkat* for assistance and *Christian Minke* for performing the solid-state NMR as well as the EDS measurements (all at Department of Chemistry at LMU Munich). We thank *Hans-Helmut Bechtel* (Lumileds) for spectral analysis.

2.5 References

[1] R. Gomez-Bombarelli, J. Aguilera-Iparraguirre, T. D. Hirzel, D. Duvenaud, D. Maclaurin, M. A. Blood-Forsythe, H. S. Chae, M. Einzinger, D. G. Ha, T. Wu, G. Markopoulos, S. Jeon, H. Kang, H. Miyazaki, M. Numata, S. Kim, W. Huang, S. I. Hong, M. Baldo, R. P. Adams, A. Aspuru-Guzik, *Nat. Mater.* **2016**, *15*, 1120-1127.

[2] X. Tang, L. S. Cui, H. C. Li, A. J. Gillett, F. Auras, Y. K. Qu, C. Zhong, S. T. E. Jones, Z. Q. Jiang, R. H. Friend, L. S. Liao, *Nat. Mater.* **2020**, *19*, 1332-1338.

[3] C. W. Tang, S. A. VanSlyke, *Appl. Phys. Lett.* **1987**, *51*, 913-915.

[4] C. Féry, B. Racine, D. Vaufrey, H. Doyeux, S. Cinà, *Appl. Phys. Lett.* **2005**, *87*.

[5] V. W. Lee, N. Twu, I. Kymissis, *Inf. Disp.* **2016**, *32*, 16-23.

[6] T. Zhan, K. Yin, J. Xiong, Z. He, S. T. Wu, *iScience* **2020**, *23*, 101397.

[7] E. Quesnel, A. Lagrange, M. Vigier, M. Consonni, M. Tournaire, V. Le Marchand, A. Suhm, P. Demars, J. C. Pillet, B. Ben Bakir, N. Olivier, E. Feltin, J. M. Lamy, M. D'Amico, E. Cao, G. Haas, L. Charrier, P. Coni, *J. Soc. Inf. Disp.* **2020**, *29*, 3-16.

[8] Y. Huang, G. Tan, F. Gou, M.-C. Li, S.-L. Lee, S.-T. Wu, *J. Soc. Inf. Disp.* **2019**, *27*, 387-401.

[9] K. Behrman, I. Kymissis, *Nat. Electron.* **2022**, *5*, 564-573.

[10] J. Shin, H. Kim, S. Sundaram, J. Jeong, B. I. Park, C. S. Chang, J. Choi, T. Kim, M. Saravanapavanantham, K. Lu, S. Kim, J. M. Suh, K. S. Kim, M. K. Song, Y. Liu, K. Qiao, J. H. Kim, Y. Kim, J. H. Kang, J. Kim, D. Lee, J. Lee, J. S. Kim, H. E. Lee, H. Yeon, H. S. Kum, S. H. Bae, V. Bulovic, K. J. Yu, K. Lee, K. Chung, Y. J. Hong, A. Ougazzaden, J. Kim, *Nature* **2023**, *614*, 81-87.

[11] Y. Wu, J. Ma, P. Su, L. Zhang, B. Xia, *Nanomaterials (Basel)* **2020**, *10*.

[12] E. Jang, S. Jun, H. Jang, J. Lim, B. Kim, Y. Kim, *Adv. Mater.* **2010**, *22*, 3076-3080.

[13] P. Pust, P. J. Schmidt, W. Schnick, *Nat. Mater.* **2015**, *14*, 454-458.

[14] P. Pust, V. Weiler, C. Hecht, A. Tucks, A. S. Wochnik, A. K. Henss, D. Wiechert, C. Scheu, P. J. Schmidt, W. Schnick, *Nat. Mater.* **2014**, *13*, 891-896.

[15] Z. Xia, A. Meijerink, *Chem. Soc. Rev.* **2017**, *46*, 275-299.

[16] K. Uheda, N. Hirosaki, Y. Yamamoto, A. Naito, T. Nakajima, H. Yamamoto, *Electrochem. Solid-State Lett.* **2006**, *9*, H22.

[17] H. Watanabe, N. Kijima, *J. Alloys Compd.* **2009**, *475*, 434-439.

[18] M. Zeuner, P. J. Schmidt, W. Schnick, *Chem. Mater.* **2009**, *21*, 2467-2473.

[19] X. Zhang, M.-H. Fang, Y.-T. Tsai, A. Lazarowska, S. Mahlik, T. Lesniewski, M. Grinberg, W. K. Pang, F. Pan, C. Liang, W. Zhou, J. Wang, J.-F. Lee, B.-M. Cheng, T.-L. Hung, Y.-Y. Chen, R.-S. Liu, *Chem. Mater.* **2017**, *29*, 6781-6792.

[20] H. S. Kim, K.-i. Machida, M. Itoh, H. Hanzawa, *ECS J. Solid State Sci. Technol.* **2014**, *3*, R234-R237.

[21] M.-H. Fang, C. O. M. Mariano, K.-C. Chen, J.-C. Lin, Z. Bao, S. Mahlik, T. Lesniewski, K.-M. Lu, Y.-R. Lu, Y.-J. Wu, H.-S. Sheu, J.-F. Lee, S.-F. Hu, R.-S. Liu, J. P. Attfield, *Chem. Mater.* **2021**, *33*, 1893-1899.

[22] M.-H. Fang, C. O. M. Mariano, P.-Y. Chen, S.-F. Hu, R.-S. Liu, *Chem. Mater.* **2020**, *32*, 1748-1759.

[23] H. Liao, M. Zhao, Y. Zhou, M. S. Molokeev, Q. Liu, Q. Zhang, Z. Xia, *Adv. Funct. Mater.* **2019**, *29*, 1901988.

[24] E. H. Song, Y. Y. Zhou, Y. Wei, X. X. Han, Z. R. Tao, R. L. Qiu, Z. G. Xia, Q. Y. Zhang, *J. Mater. Chem. C* **2019**, *7*, 8192-8198.

[25] X. Wang, E. Song, L. Qin, D. Gui, Z. Xu, J. Xie, M. Lei, H. Zhang, Y. Wang, Y. Wang, Z. Xia, W. Liu, W. Du, S. Wang, *Chem. Mater.* **2021**, *33*, 6329-6337.

[26] T. Takeda, N. Hirosaki, S. Funahshi, R.-J. Xie, *Chem. Mater.* **2015**, *27*, 5892-5898.

[27] D. S. Wimmer, M. Seibald, D. Baumann, S. Peschke, K. Wurst, G. Heymann, D. Dutzler, A. Garcia-Fuente, W. Urland, H. Huppertz, *Eur. J. Inorg. Chem.* **2021**, *2021*, 4470-4481.

[28] Y. Zhu, Y. Liang, S. Liu, H. Li, J. Chen, *Adv. Opt. Mater.* **2019**, *7*, 1801419.

[29] Y. Zhuo, S. Hariyani, J. Zhong, J. Brgoch, *Chem. Mater.* **2021**, *33*, 3304-3311.

[30] K. Yoshimura, H. Fukunaga, M. Izumi, K. Takahashi, R.-J. Xie, N. Hirosaki, *Jpn. J. Appl. Phys.* **2017**, *56*, 0417011-0417015.

[31] P. Strobel, S. Schmiechen, M. Siegert, A. Tücks, P. J. Schmidt, W. Schnick, *Chem. Mater.* **2015**, *27*, 6109-6115.

[32] M. Zhang, J. Wang, Q. Zhang, W. Ding, Q. Su, *Mater. Res. Bull.* **2007**, *42*, 33-39.

[33] X. Zhang, H.-C. Wang, A.-C. Tang, S.-Y. Lin, H.-C. Tong, C.-Y. Chen, Y.-C. Lee, T.-L. Tsai, R.-S. Liu, *Chem. Mater.* **2016**, *28*, 8493-8497.

[34] R. Shafei, D. Maganas, P. J. Strobel, P. J. Schmidt, W. Schnick, F. Neese, *J. Am. Chem. Soc.* **2022**, *144*, 8038-8053.

[35] R. D. Shannon, *Acta Crystallogr., Sect. A* **1976**, *32*, 751-767.

[36] P. Strobel, V. Weiler, P. J. Schmidt, W. Schnick, *Chem. Eur. J.* **2018**, *24*, 7243-7249.

[37] L. A. Harris, H. L. Yakel, *Acta Crystallogr., Sect. B: Struct. Crystallogr. Cryst. Chem.* **1969**, *25*, 1647-1651.

[38] Deposition number 2191356 contains the supplementary crystallographic data for this paper. These data are provided free of charge by the joint Cambridge Crystallographic Data Centre and Fachinformationszentrum Karlsruhe Access Structures service.

[39] P. E. D. Morgan, *J. Mater. Sci.* **1986**, *21*, 4305-4309.

[40] V. Bachmann, C. Ronda, O. Oeckler, W. Schnick, A. Meijerink, *Chem. Mater.* **2009**, *21*, 316-325.

[41] J. Tauc, *Mater. Res. Bull.* **1968**, *3*, 37-46.

[42] P. Kubelka, F. Munk, *Z. Tech. Phys.* **1931**, *IIa*, 593–601.

[43] X. Wang, Z. Zhao, Q. Wu, Y. Li, C. Wang, A. Mao, Y. Wang, *Dalton Trans.* **2015**, *44*, 11057-11066.

[44] Y. Q. Li, A. C. A. Delsing, G. de With, H. T. Hintzen, *Chem. Mater.* **2005**, *17*, 3242-3248.

[45] Digital Cinema Initiatives, LLC, Digital Cinema System Specification V1.0, Digital Cinema Initiatives, LLC Member Representatives Committee, **2005**.

[46] International Telecommunication Union, Recommendation ITU-R BT.2020, **2012**.

3 Blue Emitting $SrBe_{1-x}Si_{2+x}O_{3-2x}N_{2+2x}:Eu^{2+}$ ($x \approx 0.1$)

Tobias Giftthaler, Marwin Dialer, Philipp Strobel, Peter J. Schmidt and Wolfgang Schnick

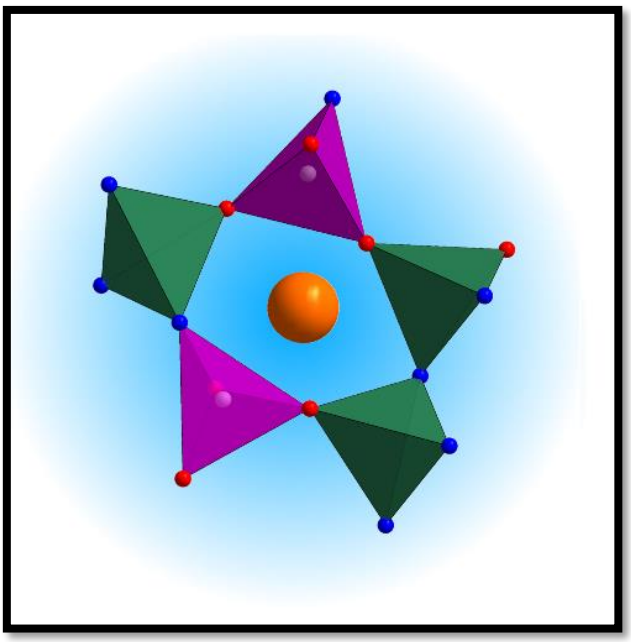

Abstract: In the search for materials for high-efficiency lighting applications, the color-point tuning of phosphors for inorganic phosphor converted LEDs (pcLEDs) is of special interest. We expand the recently explored phosphor class of SiBeONs (oxinitridoberyllosilicates) by the synthesis and characterization of $SrBe_{1-x}Si_{2+x}O_{3-2x}N_{2+2x}:Eu^{2+}$. High temperature synthesis, starting from Sr_2N, BeO, SiO_2 and Si_3N_4, yields the target phase as the main product. Upon doping with Eu^{2+}, the pale blue crystals exhibit blue luminescence with emission at 456 nm and a full width at half maximum (*fwhm*) of 66 nm / 3108 cm^{-1}. The structure is an ordered variant of the $LaSi_3N_5$ structure type and was elucidated by single-crystal X-ray diffraction data. The network in $SrBe_{1-x}Si_{2+x}O_{3-2x}N_{2+2x}:Eu^{2+}$ is highly condensed with a condensation degree of $\kappa = 0.6$ comprising corner-sharing $[MX_4]$ (M = Be, Si; X = O, N) tetrahedra, with mixed occupancies on both the ligand and central metal sites.

3.1 Introduction

As part of environmental efforts to save energy, solid-state lighting using phosphor-converted LEDs (pcLEDs) can contribute to a more energy-efficient future. In white emitting pcLEDs, ultraviolet (UV) or blue light emitted from a semiconductor chip is partially converted by ceramic phosphors to reproduce the spectral power distribution of natural white light in the visible spectral range. Hereby, the chemical tunability of applied phosphors is essential to achieve the desired emission. The luminescence of widely used aluminates and silicates, as well as their respective nitride equivalents, is conventionally tuned by substitution of the cations on the doped site. Industrially, this is applied in the red spectral region by emission optimization in $AE_2Si_5N_8:Eu^{2+}$ (*AE* = Ca, Sr, Ba) or $Ca_{1-x}Sr_xAlSiN_3:Eu^{2+}$ and in the green spectral region in $RE_{3-x}Al_{5-y}Ga_yO_{12}:Ce_x$.[1-5]
As shown by the substitution of Si^{4+} by Al^{3+} or Li^+, elemental substitutions at the network-building positions can also alter the emission of doped phosphors. In this case, charge neutrality is maintained by O/N/F substitution on the anion sites, which changes the coordination environment of the emitter.[6-7] Due to the nephelauxetic effect and crystal field splitting this leads to a change in emission wavelengths. Based on the comparable sizes of Be^{2+} and Si^{4+} cations (0.27 Å and 0.26 Å respectively, in tetrahedral coordination), beryllates in general are closely related to silicates and their respective nitride derivatives.[8-12] Hence, replacing Al/Li/Si by Be can potentially be used as a third substitution pathway to target selected spectral regions more efficiently without altering the formal anionic composition.

An established cyan emitting phosphor is $SrSiAl_2O_3N_2:Eu^{2+}$, which has an emission maximum at ~487 nm with an *fwhm* greater than 85 nm, while spectral properties depend on the dopant concentration.[13-15]
In this context, we report here on the derived, blue emitting phosphor $SrBe_{1-x}Si_{2+x}O_{3-2x}N_{2+2x}:Eu^{2+}$(SBS).

3.2 Results and Discussion

High temperature synthesis of $SrBe_{1-x}Si_{2+x}O_{3-2x}N_{2+2x}:Eu^{2+}$ starting from Sr_2N, BeO, SiO_2, Si_3N_4 and EuF_3 yielded an air- and moisture-insensitive pale blue powder. Powder X-ray diffraction (PXRD) experiments confirmed SBS as the main product phase (> 80 wt%) with $SrBeSiO_4$, Sr_2SiO_4 and $BeSiN_2$ as minor side-products (see Figure S2). SBS crystallizes in the orthorhombic space group $P2_12_12_1$ (no. 19) with cell parameters a = 4.7671(2), b = 7.7683(2) and c = 10.9364(3) Å and is an ordered variant of the $LaSi_3N_5$ structure type.[16] The chemical composition of the target phase was confirmed by EDS (averaged

over seven data points; $Sr_{1.0}BeSi_{2.8(2)}O_{3.3(1)}N_{2.3(3)}$; see table S1).

Details of the crystal structure and product phase determination are given in the Supporting Information (tables S2-S5).

As shown in Figure 1, in SBS O and N coordinate Be and Si in corner sharing tetrahedra. This results in a highly condensed network with a degree of condensation $\kappa = 0.6$. Sr is (8+2)-fold coordinated by O and N in a distorted double capped square antiprism (Johnson polyhedron 17). Hereby, N sites are fully occupied, whereas two of three O sites are occupied by both O and N. The O sites and those with mixed occupancy can be identified by significantly shorter interatomic distances compared to the N sites in $[MX_4]$ (M = Be, Si X = N, O) tetrahedra. Charge neutrality is maintained, by a mixed occupation of the single Be site by Be and Si. Both Si sites are fully occupied. Tetrahedra form *fünfer*-rings with channels along [100].[17]

BVS and CHARDI calculations corroborate the proposed structure model and the

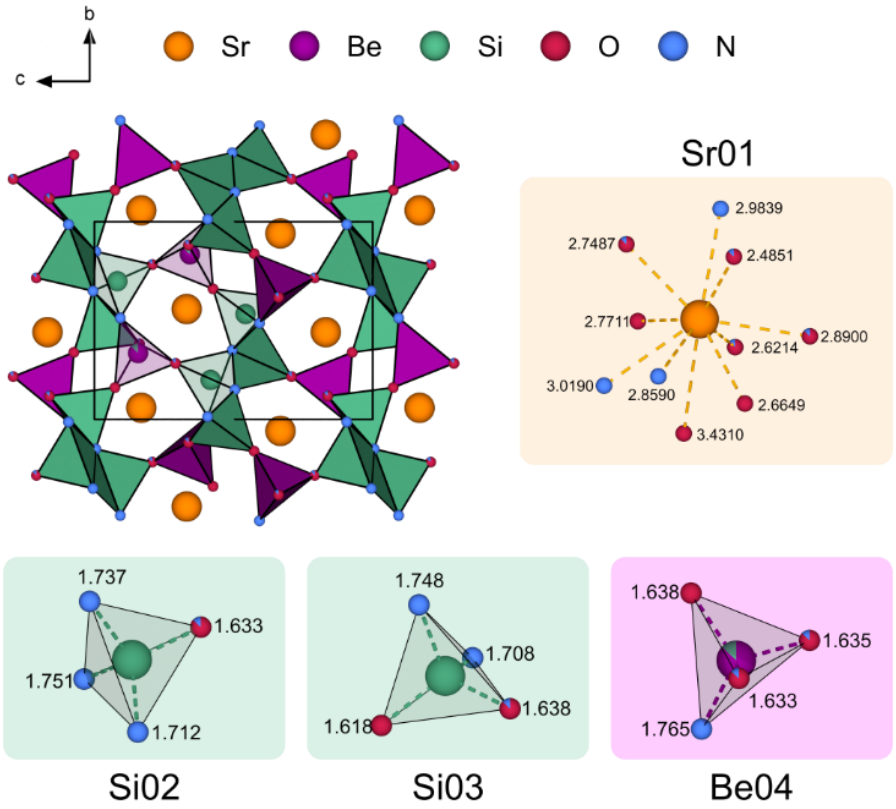

assignment of mixed occupancies (see table S6).[18-20]

Figure 1. Structure of $SrBe_{1-x}Si_{2+x}O_{3-2x}N_{2+2x}:Eu^{2+}$. Sr orange, Be and $[BeO_3N]$ tetrahedra purple, Si and $[SiON_3]$/$[SiO_2N_2]$ tetrahedra green, O red, N blue; crystal structure projection along [100]; corner-sharing tetrahedra connected *via* O/N; coordination environments of the cations by O and N with atomic distances given in Å.

Upon doping with Eu^{2+} and excitation with radiation wavelengths shorter than 400 nm, the target phase exhibits blue luminescence. Single crystal luminescence experiments showed a maximum emission at 456 nm and *fwhm* of 66 nm / 3108 cm^{-1} (Figure 2). Compared to the structurally closely related $SrSiAl_2O_3N_2:Eu^{2+}$, SBS emits a narrower emission spectrum at shorter wavelengths. The slightly changed emission properties are likely due to a change in the orientation of Eu^{2+} 5*d* orbitals relative to their coordination sphere. The shorter average distances in SBS to the ligands and the smaller coordination polyhedron with respect to $SrSiAl_2O_3N_2:Eu^{2+}$ are typically not expected to result in shorter emission wavelengths.[21] A similar anomaly has been observed in $Sr_{1-x}Ba_xSiAl_2O_3N_2:Eu^{2+}$, where chemical pressure of the second and third coordination sphere was used as an explanation. [15] The difference is, that in SBS the coordination sphere increases compared to the respective reference and therefore other mechanisms must determine the emission. Hence, theoretical calculations of the crystal fields and excited states of Eu^{2+} ($4f^6 5d^1$) are necessary for further clarification.[22]

The system $SrSiAl_2O_3N_2:Eu^{2+}$/ $SrBe_{1-x}Si_{2+x}O_{3-2x}N_{2+2x}:Eu^{2+}$ can be an example of color point tuning of phosphors by Be substitution. However, due to the presence of minor phases and the use of toxic BeO as a precursor, industrial application of SBS is currently not a main focus. Instead, the route of using beryllium as an additional or substituting network building cation proves promising to enable activator sites in next generation luminescent materials with further optimized performance.

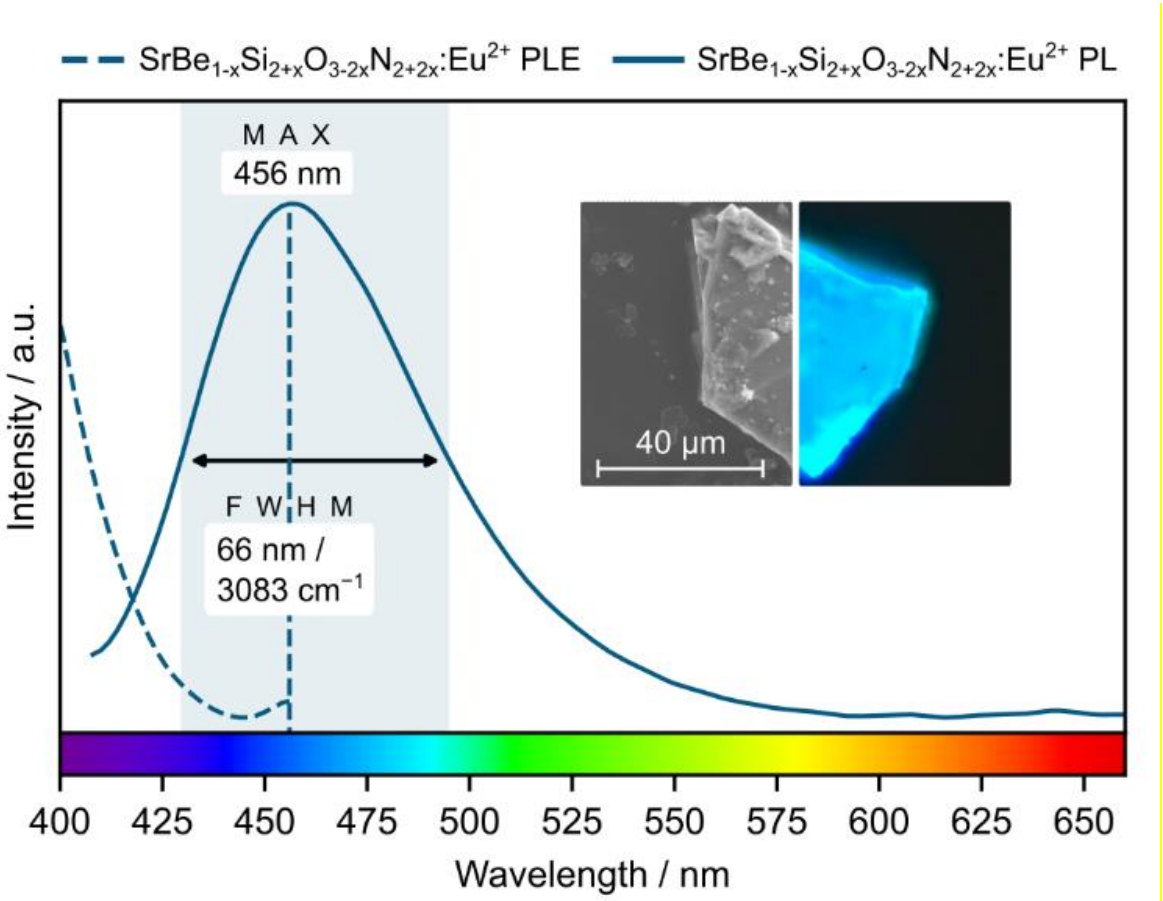

Figure 2. Luminescence spectrum of $SrBe_{1-x}Si_{2+x}O_{3-2x}N_{2+2x}:Eu^{2+}$. The excitation (blue dashed line) and emission of SBS under UV irradiation (blue line) with an emission maximum at 456 nm and a *fwhm* of 66 nm; selected particle of SBS in an optical and a scanning electron microscope.

3.3 Conclusion and Outlook

The luminescent properties of $SrBe_{1-x}Si_{2+x}O_{3-2x}N_{2+2x}:Eu^{2+}$ illustrate the potential of SiBeONs for application as phosphor materials. It is shown that substitution of Be^{2+} for the known network-building cations Al^{3+} and Si^{4+} enables comparatively narrow-band emission. For further investigations, phase pure samples can be beneficial to determine quantum efficiencies as well as electronic properties like the band structure and gap. For further elucidation of mixed occupations, neutron scattering experiments could provide new insights.

SiBeONs in general can help to achieve desired emission characteristics in future phosphor applications, especially those containing low quantities of beryllium.

3.4 Experimental Section

Safety Precautions.

BeO is characterized as toxic and was therefore exclusively handled in closed systems, under Schlenk conditions or inside a glovebox. [23-24] For safety precautions the product was also handled under closed conditions, although, chemically stable multinary beryllates as the mineral beryl are not known to be harmful.

Synthesis.

The starting materials Sr_2N (synthesized from Sr, *Sigma Aldrich*, 99.99%) BeO (*Alfa Aesar*, 99.95%), SiO_2 (*Acros Organics*, 60 A) and Si_3N_4 (*UBE*, SNA-00) were ground in a tungsten carbide mortar inside a glovebox (Unilab, *MBraun*, Garching; O_2<0.1 ppm, H_2O <0.1 ppm) together with EuF_3 (Sigma-Aldrich, 99.99%) for luminescence experiments and transferred to a W crucible. Reactions were carried out in a radio frequency furnace (TIG 10/100; Hüttinger Elektronik Freiburg, Germany) under dried N_2 atmosphere. For the reaction the crucible was heated to 1600 °C in 30 minutes, the temperature was held for further 30 minutes, cooled down in 30 minutes to 600 °C and then quenched to room temperature by turning off the heating.

Singe-Crystal X-ray diffraction.

Data of micromount fixed single crystals of $SrBe_{1-x}Si_{2+x}O_{3-2x}N_{2+2x}:Eu^{2+}$ were collected on a Bruker D8 Venture rotary anode diffractometer with Mo-Kα radiation (λ = 0.71073 Å), that was focused with a Goebel mirror. The collected data was integrated and absorption corrected with APEX3.[25] Structures were solved by direct methods with SHELXS and refined with SHELXL, applying the full-matrix least square method.[26-27]

Powder X-ray diffraction.

Powder samples were ground in a tungsten carbide mortar and sealed in glass capillaries (*Hilgenberg*, *d* = 0.5 mm). Measurements were carried out on a rotary head STOE STADI P diffractometer (Cu-$K\alpha_1$ radiation, Ge(111) monochromator, Mythen 1k detector) with

modified Debye-Scherrer geometry. The TOPAS 6 software package was used for Rietveld refinement and determining of the given phase composition.[28]

Elemental analysis.

To determine the elemental composition of $SrBe_{1-x}Si_{2+x}O_{3-2x}N_{2+2x}:Eu^{2+}$, energy dispersive X-ray spectroscopy (EDS) on a Dualbeam Helios Nanolab G3 UC scanning electron microscope (SEM, FEI) with X-Max 80 SDD detector (Oxford Instruments) was applied. Data of a selected particle were collected at an acceleration voltage of 25 kV.

Luminescence.

Luminescence data of selected particles and single crystals were obtained on an Olympus BX51 microscope with a HORIBA Fluoromax4 spectrofluorimeter system attached. Particle and single crystal images were taken on a ZEISS AXIO imager M1m microscope.

3.5 Acknowledgements

The authors thank Dr. Peter Mayer and Reinhard Pritzl for collecting single-crystal data as well as Christian Minke (all at Department of Chemistry, LMU Munich) for EDS measurements.

3.6 References

[1] O. M. ten Kate, Z. Zhang, P. Dorenbos, H. T. Hintzen, E. van der Kolk, *J. Solid State Chem.* **2013**, *197*, 209-217.

[2] T. Schlieper, W. Milius, W. Schnick, *Z. Anorg. Allg. Chem.* **1995**, *621*, 1380-1384.

[3] H. Watanabe, N. Kijima, *J. Alloys Compd.* **2009**, *475*, 434-439.

[4] J. M. Ogieglo, A. Katelnikovas, A. Zych, T. Justel, A. Meijerink, C. R. Ronda, *J. Phys. Chem. A* **2013**, *117*, 2479-2484.

[5] D. Nakauchi, Y. Yoshida, N. Kawaguchi, T. Yanagida, *J. Mater. Sci. - Mater. Electron.* **2019**, *30*, 14085-14090.

[6] P. Pust, V. Weiler, C. Hecht, A. Tucks, A. S. Wochnik, A. K. Henss, D. Wiechert, C. Scheu, P. J. Schmidt, W. Schnick, *Nat. Mater.* **2014**, *13*, 891-896.

[7] G. J. Hoerder, M. Seibald, D. Baumann, T. Schröder, S. Peschke, P. C. Schmid, T. Tyborski, P. Pust, I. Stoll, M. Bergler, C. Patzig, S. Reissaus, M. Krause, L. Berthold, T. Hoche, D. Johrendt, H. Huppertz, *Nat. Commun.* **2019**, *10*, 1824.

[8] L. Eisenburger, O. Oeckler, W. Schnick, *Chem. Eur. J.* **2021**, *27*, 4461-4465.

[9] S. Merlino, C. Biagioni, E. Bonaccorsi, N. V. Chukanov, I. V. Pekov, S. V. Krivovichev, V. N. Yakovenchuk, T. Armbruster, *Mineral. Mag.* **2018**, *79*, 145-155.

[10] L. A. Harris, H. L. Yakel, *Acta Crystallogr., Sect. B: Struct. Crystallogr. Cryst. Chem.* **1969**, *25*, 1647-1651.

[11] P. Strobel, V. Weiler, P. J. Schmidt, W. Schnick, *Chem. Eur. J.* **2018**, *24*, 7243-7249.

[12] N. Krishna Rao, T. Sreenivas, *Miner. Process. Extr. Metall. Rev.* **1994**, *13*, 19-42.

[13] R. Lauterbach, W. Schnick, *Z. Anorg. Allg. Chem.* **1998**, *624*, 1154-1158.

[14] X. Wang, Z. Zhao, Q. Wu, Y. Li, C. Wang, A. Mao, Y. Wang, *Dalton Trans.* **2015**, *44*, 11057-11066.

[15] W.-Y. Huang, F. Yoshimura, K. Ueda, Y. Shimomura, H.-S. Sheu, T.-S. Chan, C.-Y. Chiang, W. Zhou, R.-S. Liu, *Chem. Mater.* **2014**, *26*, 2075-2085.

[16] Z. Inoue, M. Mitomo, N. Ii, *J. Mater. Sci.* **1980**, *15*, 2915-2920.

[17] F. Liebau, *Structural Chemistry of Silicates*, Springer, Berlin, Heidelberg, **1985**. The term "*fünfer ring*", as defined by Liebau, describes a ring of five tetrahedra and is derived from the german word *fünf* – five.

[18] N. E. Brese, M. O'Keeffe, *Acta Crystallogr. Sect. B: Struct. Sci.* **1991**, *47*, 192-197.

[19] I. D. Brown, D. Altermatt, *Acta Crystallogr. Sect. B: Struct. Sci.* **1985**, *41*, 244-247.

[20] R. Hoppe, S. Voigt, H. Glaum, J. Kissel, H. P. Müller, K. Bernet, *J. Less Common Met.* **1989**, *156*, 105-122.

[21] M.-H. Fang, C. O. M. Mariano, P.-Y. Chen, S.-F. Hu, R.-S. Liu, *Chem. Mater.* **2020**, *32*, 1748-1759.

[22] R. Shafei, D. Maganas, P. J. Strobel, P. J. Schmidt, W. Schnick, F. Neese, *J. Am. Chem. Soc.* **2022**, *144*, 8038-8053.

[23] O. Kumberger, H. Schmidbaur, *Chem. Unserer Zeit* **1993**, *27*, 310-316.

[24] D. Naglav, M. R. Buchner, G. Bendt, F. Kraus, S. Schulz, *Angew. Chem. Int. Ed.* **2016**, *55*, 10562-10576.

[25] BrukerAXS, Billerica, **2016**.

[26] G. M. Sheldrick, *Acta Crystallogr., Sect. C: Struct. Chem.* **2015**, *71*, 3-8.

[27] G. M. Sheldrick, *Acta Crystallogr. Sect. A* **2008**, *64*, 112-122.

[28] A. A. Coelho, in *TOPAS Academic*, 6 ed., Brisbane (Australia), **2016**.

4 The Nitridoberyllosilicate System *AE*$BeSi_2N_4$ (*AE* = Ca, Ba)

Tobias Giftthaler, Philipp Strobel, Lucien Eisenburger, Oliver Oeckler and Wolfgang Schnick

Abstract: The structural relations between different alkaline-earth containing nitridosilicates have been extensively studied due to their application as LED phosphors. This contribution focuses on the related, recently explored compound class of nitridoberyllosilicates, with only two previously known phases. The class is expanded by the presented $CaBeSi_2N_4$ and $BaBeSi_2N_4$. The structural relations between these two phases and the pre-existent $SrBeSi_2N_4$ are viewed in detail. All three alkaline earth nitridoberyllosilicates express trigonal-planar [BeN_3] and double-tetrahedral [Si_2N_7] units. In comparison to the Sr phase, the double tetrahedra units are bent in the Ca and tilted in the Ba phase. This adaptation to the respective cationic radii leads to altered luminescent properties, as known from nitridosilicates.

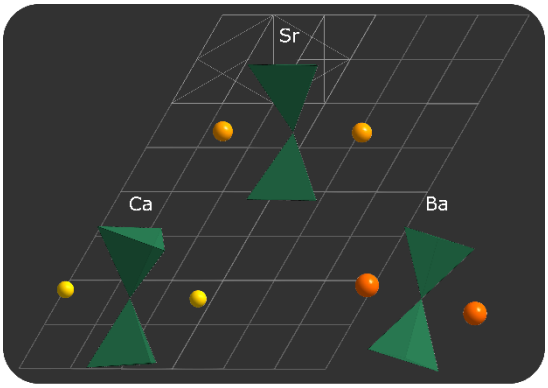

4.1 Introduction

The broadly investigated material class of nitridosilicates raised attention in recent years, as many of them show luminescence upon Eu^{2+} doping. Therefore, various nitridosilicates found application as phosphors in inorganic phosphor converted light emitting diodes (pcLEDs).[1-4] The structures of nitridosilicates are closely related to silicates, but the introduction of nitrogen allows for unprecedented motifs as nitrogen can connect three or more tetrahedral centers. In analogy to silicates, the structural variety of nitridosilicates is expanded by the introduction of additional network building cations, as Al^{3+}, Li^{+} and Be^{2+}.[5-7] Hereby, the similar to Si^{4+} sized Be^{2+} can be coordinated tetrahedral or trigonal planar. These coordinations are expressed in the double nitride $BeSiN_2$ (tetrahedral) and the nitridoberyllosilicate $Sr[BeSi_2N_4]$ (trigonal planar).[8, 9]

This expansion of possible structural motifs raises the question, if a nitridoberyllosilicate system shows adaption to cationic radii in analogy to nitridosilicates and related nitride compound classes. These can show adjustment of structural motifs to given cations, while the structures of compounds with similar degree of condensation are commonly closely related. An effect, well understood in the systems $M_2Si_5N_8$ and $M[Mg_3SiN_4]$.[1, 10-12] Especially the therefore changed symmetry of cationic sites can be highly influential on luminescence properties.[13]

The adaption of $Sr[BeSi_2N_4]$ to different alkaline earth cations can be subject to closer investigation, as the only other Be–Si–N compound $Eu[BeSi_2N_4]$ expresses an isotypic structure, due to the similar radii of Sr^{2+} and Eu^{2+}.[9]

$Sr[BeSi_2N_4]$ exhibits vertex sharing $[Si_2N_7]$ double tetrahedra with Si–N–Si angles of 180° and connecting $[BeN_3]$ trigonal planary units.[9] Herein we present the adaption of this network and the expressed structural motifs to the smaller radius of Ca^{2+} as well as the larger radius of Ba^{2+} and elucidate the symmetry changes in cationic positions of the alkaline earth ions.

4.2 Results and Discussion

Synthesis and Elemental Analysis

The high temperature syntheses of $Ca[BeSiN_2]$ and $Ba[BeSi_2N_4]$ yields pale yellow powders. Eu^{2+} doped $Ba[BeSi_2N_4]$ exhibits an orange body color. All products are stable towards air and moisture and crystallize in microcrystalline plate like morphology (See Figures S4/5). Energy dispersive X-ray spectroscopy (EDS) confirmed the chemical composition ($Ca_{1.0}BeSi_{2.1}N_4$, $Ba_{1.0}BeSi_{2.0}N_{3.7}$). Beryllium can not be quantified by this method.

Crystal Structure Determination

The existing structure model of $Sr[BeSi_2N_4]$ in $P\bar{6}2c$ (no. 190) was used as a starting model to understand the structure of $Ca[BeSi_2N_4]$, as the degree of condensation κ, the ratio of network building cations to anions, remains unchanged at 3/4. However, PXRD data indicated significant structural differences between the compounds, but showed insufficient for elucidation of the correct crystal structure. Due to the lack of large single crystals, micro focused synchrotron radiation was used for structure elucidation. In contrast, the structure of $Ba[BeSI_2N_4]$ could be solved and refined from data of larger single crystals. Powder X-ray diffraction data corroborates to the respective structural models.

Crystal Structure Description

$Ca[BeSi_2N_4]$ crystallizes in the hexagonal space group $P\bar{6}$ (no. 174) with lattice parameters $a = b = 8.369(1)$ Å and $c = 9.190(1)$ Å.

$Ba[BeSi_2N_4]$ crystallizes in the orthorhombic space group *Ama*2 (no. 40) with lattice parameters $a = 8.1314(4)$ Å, $b = 9.9947(6)$ Å and $c = 4.8017(3)$ Å. Further details regarding the structure elucidation in the supporting information.

The structures of $Ca[BeSi_2N_4]$ and $Ba[BeSi_2N_4]$ are closely related to the structure of $Sr[BeSi_2N_4]$. All exhibit layers of vertex sharing trigonal-planar $[BeN_3]$ and tetrahedral $[SiN_4]$ units. The layers are connected by vertices of $[SiN_4]$ units, eventually forming $[Si_2N_7]$ double tetrahedra.

In Ca[$BeSi_2N_4$] however, due to the comparatively smaller size of Ca^{2+}, the layers contract by reduction of the Si-N-Si angles (152 and 156° as given in Figure 2) along stacking direction [001], resulting in reduced unit cell parameter *c* of 9.19 Å in the Ca phase compared to 9.42 Å in the Sr phase. Subsequently, [Si_2N_7] double tetrahedral units are bent with resulting Si–N–Si angles of.

In contrast, the larger size of Ba^{2+} cations results in layers tilted from [010] not being parallel to the stacking direction anymore and therefore an expanded *b* axis ([010] in the orthorhombic crystal system) of 10.0 Å. The [Si_2N_7] double tetrahedral units are tilted, while the Si–N–Si angles are slightly reduced to 174° (also see Figure 2).

Since the differing ionic cation radii mainly effect the distance between respective layers, the lattice parameters primarily change in one crystallographic direction. Hence, for better understanding of the symmetry relations between the three structures a 2*D*–projection of the unit cells, along the stacking direction, as given in Figure 1 is beneficial. The Ca[$BeSi_2N_4$] cell is a $\sqrt{3} \times \sqrt{3}\, R30$ super cell to the unit cell of Sr[$BeSi_2N_4$]. Herein, the vector a_{Ca} with a length of 8.37 Å is shorter than the comparable vector $a_{ortho,\,Sr}$ in Sr[$BeSi_2N_4$] with 8.42 Å (shown in Figure 1 as dashed red line) but longer than the respective vector a_{Ba} of Ba[$BeSi_2N_4$] with 8.13 Å. The c_{Ba} vector in Ba[$BeSi_2N_4$] with 4.80 Å is also shorter than the respective a_{Sr} vector in Sr[$BeSi_2N_4$] with 4.86 Å and 1/3 of the corresponding $a_{ortho,\,Ca}$ in Ca[$BeSi_2N_4$] with 4.83 Å (shown in Figure 1 as dashed black line). The respective lattice parameters of Ca[$BeSi_2N_4$] as well as of Ba[$BeSi_2N_4$] contract slightly in the *ab* plane (*ac* for Ba[$BeSi_2N_4$]) compared to Sr[$BeSi_2N_4$]. The main difference in cell volume per formula unit is therefore found in the respective orthogonal axis, *c* for Ca[$BeSi_2N_4$] and Sr[$BeSi_2N_4$] and *b* for Ba[$BeSi_2N_4$].

Subsequently the symmetry of the alkaline earth cationic site is changed from a 2*d* position in Sr[$BeSi_2N_4$] to 3*j* and 3*k* positions in Ca[$BeSi_2N_4$] and a 4*b* position in Ba[$BeSi_2N_4$].

Further structural details are given in the *Bärnighausen* tree in the supporting information (Figure S3).

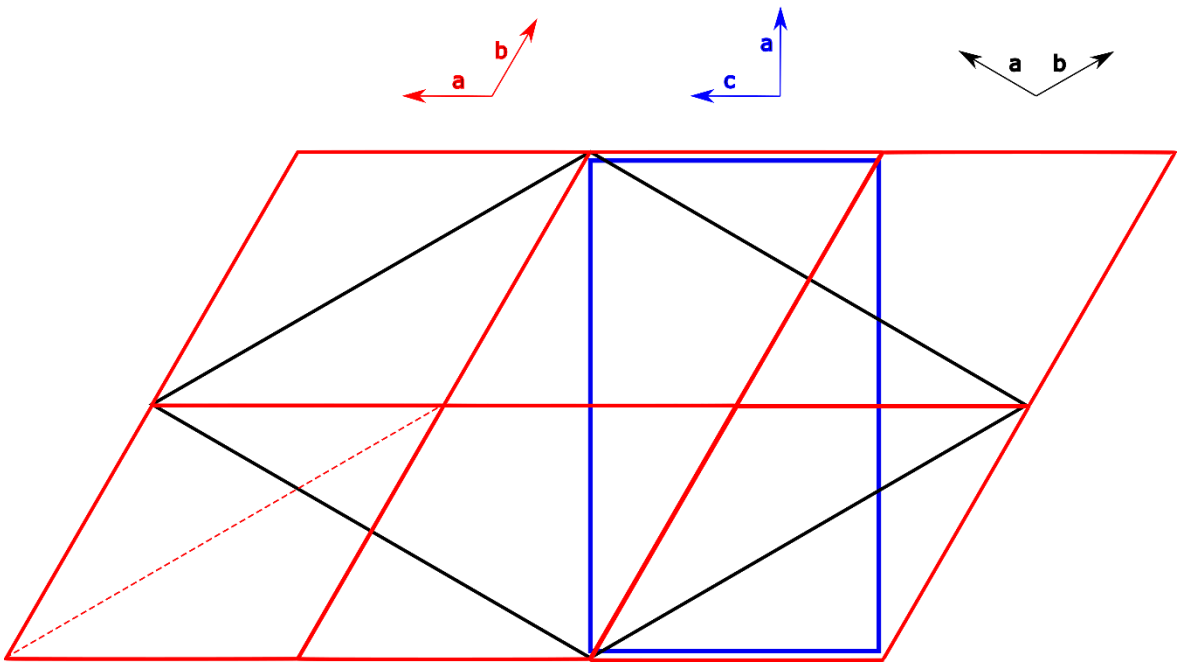

Figure 1. Relation of lattice parameters of *AE*[$BeSi_2N_4$] (*AE* = Ca, Sr, Ba). The unit cells of Ca[$BeSi_2N_4$] (black), Sr[$BeSi_2N_4$] (red) and Ba[$BeSi_2N_4$] (blue) in respective orientation. The red dashed line represents the length of the orthohexagonal $a_{ortho,\ Sr}$ vector, the black dashed line the length of $a_{ortho,\ Ca}$. All unit cells are shown to scale.

Table 1. Lattice parameters of *AE*[$BeSi_2N_4$] (*AE* = Ca, Sr, Ba).

	Ca[$BeSi_2N_4$]	Sr[$BeSi_2N_4$]	Ba[$BeSi_2N_4$]
a / Å	8.369(1)	4.861(2)	8.1314(4)
b / Å	8.369(1)	4.861(2)	9.9947(6)
c / Å	9.190(1)	9.423(4)	4.8017(3)
a_{ortho}		$\sqrt{3}a$ = 8.420	
$\frac{1}{3}a_{ortho}$	$\frac{a}{\sqrt{3}}$ = 4.831		
V / Å^3	557.43(15)	192.807(1)	390.24(4)
Z	6	2	4
V / *Z*	92.905	96.4035	97.56

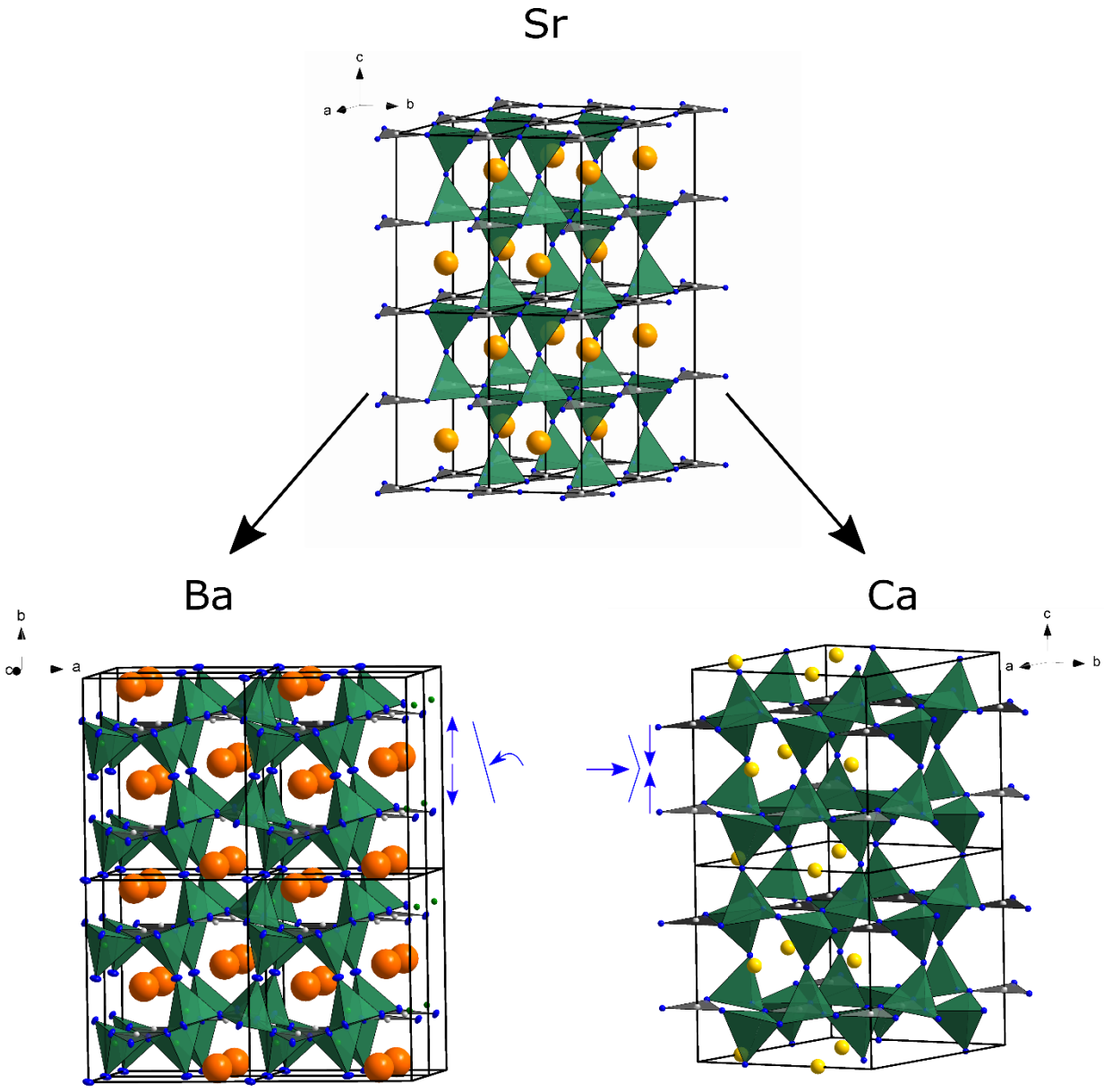

Figure 2. Crystal strutures of *AE*[$BeSi_2N_4$] (*AE* = Ca, Sr, Ba). The structures of Ca[$BeSi_2N_4$] and Ba[$BeSi_2N_4$] derived from Sr[$BeSi_2N_4$] . Ca (yellow), Sr (bright orange), Ba (dark orange), Be (grey), Si (green), N (blue). [BeN_3] trigonal-planary units in grey and [SiN_4] tetrahedra in green. [Si_2N_7] double tetrahedra are tilted in Ba[$BeSi_2N_4$], the layers diverge, in contrast [Si_2N_7] double tetrahedra are bent in Ca[$BeSi_2N_4$], the layers converge.

Luminescence of $Ba[BeSi_2N_4]:Eu^{2+}$.

Upon doping with Eu^{2+},$Ba[BeSi_2N_4]$ shows orange luminescence under irradiation with blue light. The maximum emission wavelength λ_{max} is 596 nm and the full width at half maximum *fwhm* = 100 nm / 2806 cm^{-1} (spectra see Figure S6). Due to the larger coordination polyhedron of Ba^{2+} compared to Sr^{2+} and the therefore lowered nephelauxetic effect, emission at increased wavelengths is expected. However, as $Sr[BeSi_2N_4]:Eu^{2+}$ shows nontypical emission properties, the emission is not directly comparable. $Ca[BeSi_2N_4]$ shows no luminescence upon doping with Eu^{2+}.

4.3 Conclusions

The system *AE*$[BeSi_2N_4]$ (*AE* = Ca, Sr, Ba) shows the adaption of an anionic host lattice to the ionic radius of its counter cation. While the cell parameters, with respect to *Z* and the cell symmetry,
mainly adjust along the stacking direction (*c* in the hexagonal, *b* in the orthorhombic system), the structural motifs are altered slightly. This adaption leads to changed symmetry of the alkaline earth site and therefore changed luminescence properties as well. A detailed elucidation of luminescence and electronic properties of the *AE*$[BeSi_2N_4]$ (*AE* = Ca, Sr, Ba) system is subject to investigation and will be published separately.

4.4 Experimental Section

Safety Precautions.

All tasks were performed in closed systems, like Schlenk-lines and gloveboxes to minimize the risk of exposure. This is necessary because Be is considered a highly hazardous element. Especially Be containing dusts are known to cause various medical conditions as CBD (chronic beryllium disease) and might be carcinogenic.[14-15]

Synthesis.

Due to their sensitivity towards moisture and oxygen, as well as the toxicity of Be and most Be containing compounds, all starting materials were handled under argon atmosphere in

a glovebox (Unilab, *MBraun*; O_2<0.1 ppm, H_2O <0.1 ppm). The experiments were carried out in a RF-furnace attached to a Schlenk-type vacuum line (10^{-3} mbar) under dried N_2 (*Air Liquid*, 5.0). The atmosphere was purified by passage through columns filled with KOH (*Merck*, ≥85%), silica gel (*Merck*), molecular sieve (*Fluka*, 4 Å), P_4O_{10} (*Roth*, ≥99%) and BTS catalyst.

Samples of Ca[$BeSi_2N_4$] were obtained by reaction of $Ca(NH_2)_2$ (synthesized from Ca (*Alfa Aesar*, 99.98%) in an autoclav under NH_3 atmosphere at 200 °C), Be_3N_2 (synthesized from Be (*ABCR*, 99%) in an rf-furnace under N_2 atmosphere at 1300 °C) and "$Si(NH)_2$" (from $SiCl_4$ in liquid NH_3) in a rf-furnace under N_2 atmosphere at 1400 °C. After mixing the starting materials in a tungsten carbide mortar and transferring the mixture into a W crucible, it was heated to 1400 °C in 0.75 h. This temperature was kept for 6 h, then the crucible was cooled to 700 °C in 10 h and subsequently to room temperature by shutting off the heating. Samples of Ba[$BeSi_2N_4$] were obtained by reaction of Ba_2N (synthesized from Ba (*Alfa Aesar*, 99.9%) under N_2 flow at 830 °C)[16], Be_3N_2 (see above) and Si_3N_4 (UBE, SNA-00) by identical method. Ba[$BeSi_2N_4$]:Eu^{2+} was synthesized accordingly, with EuF_2 as additional precursor.

Electron microscopy.

Energy dispersive X-ray spectroscopy (EDS) was used to determine the elemental composition of *AE*$BeSi_2N_4$. The data was obtained at an accelerating voltage of 20 kV on a Dualbeam *Helios Nanolab* G3 UC scanning electron microscope (SEM, FEI) with X-Max 80 SDD detector (*Oxford Instruments*) from several particles. Crystal images were taken on the given electron microscope as well.

Single-crystal X-ray diffraction.

Single crystals of Ba[$BeSi_2N_4$] were selected and mounted on the loop of MicroMounts (*MiTeGen*). Data was collected on a *Bruker* D8 Venture diffractometer with Mo–K_α radiation and a graphite monochromator. The APEX 3 program package was used for integration and multi-scan absorption correction.[17] The structure was solved with SHELXS applying direct methods and refined against F^2 with SHELXL by the full-matrix least squares method.[18, 19]

Data of single microcrystals of Ca[$BeSi_2N_4$] were collected on beamline ID11 of the ESRF (Grenoble, France). The TEM grid was mounted on a Symétrie Hexapods Nanopos device. A Ca[$BeSi_2N_4$] crystal of about 6 μm^3 in size was recovered at beamline ID11 (λ=0.309 Å, ESRF, Grenoble) by a telescope with large magnification, using the copper crossbars of the grid as landmarks. The crystallite was centred using Ca X-ray fluorescence scans. The

single-crystal data set was then collected using a microfocused synchrotron beam of 1×2 µm. CrysAlisPro and SADABS were used for the integration and the semiempirical absorption correction of the data. The incomplete absorption of X-ray radiation in the CCD phosphor was corrected. The crystal structure was solved by direct methods and refined by least-squares methods with SHELX-2014.

Powder X-ray diffraction.

Samples of *AE*$BeSi_2N_4$ were ground and sealed in glass capillaries (*Hilgenberg*, *d* = 0.2 mm for Ca, d = 0.3 mm or Ba) and mounted on a rotary head in a *STOE* STADI P diffractometer (Cu–$K\alpha_1$ radiation for Ca, Ag–K_α radiation for Ba, Ge(111) monochromator, Mythen 1k detector) with modified Debye-Scherrer geometry. The TOPAS 6 program package was used for Rietveld refinement.

Luminescence.

The luminescence of single particles of $Ba[BeSi_2N_4]:Eu^{2+}$ was measured on an *Olympus* BX51 microscope with attached *HORIBA* Fluoromax4 spectrofluorimeter system. The excitation was carried out by blue light with a wavelength of 420 nm and a spectral width of 10 nm. The emission spectrum was measured from 480 to 820 nm with a step size of 1 nm.

Transmission electron microscopy (TEM):

The sample was ground in an agate mortar, suspended in ethanol and drop-cast on a copper grid with holey carbon film (S160NH2C, Plano GmbH, Wetzlar, Germany). The grid was mounted on a double-tilt holder and isolated crystallites of $Ca[BeSi_2N_4]$ were identified by EDX and electron diffraction using a FEI Tecnai G20 transmission electron microscope (TEM) with a thermal emitter (LaB_6) operated at 200 keV. Selected area electron diffraction patterns and bright-field images were recorded using a TVIPS camera (TemCam F216, Tietz) with a resolution of 2048×2048 pixels.

4.5 Acknowledgements

The authors thank Dr. Peter Mayer and Dr. Constantin Hoch for collecting single-crystal data as well as Amalina Buda and Christian Minke (all at Department of Chemistry, LMU Munich) for EDS measurements. Furthermore, we are thankful for beamtime at the ESRF for the acquisition of microfocused single-crystal diffraction data (project CH-5140).

4.6 References

[1] H. A. Höppe, H. Lutz, P. Morys, W. Schnick and A. Seilmeier; Luminescence in Eu^{2+}-doped $Ba_2Si_5N_8$: fluorescence, thermoluminescence, and upconversion, *J. Phys. Chem. Solids* **2000**, *61*, 2001, doi:10.1016/s0022-3697(00)00194-3.

[2] R. Mueller-Mach, G. Mueller, M. R. Krames, H. A. Höppe, F. Stadler, W. Schnick, . . . P. Schmidt; Highly efficient all-nitride phosphor-converted white light emitting diode, *Phys. Stat. Sol. (A)* **2005**, *202*, 1727, doi:10.1002/pssa.200520045.

[3] L. Wang, R. J. Xie, T. Suehiro, T. Takeda and N. Hirosaki; Down-Conversion Nitride Materials for Solid State Lighting: Recent Advances and Perspectives, *Chem. Rev.* **2018**, *118*, 1951, doi:10.1021/acs.chemrev.7b00284.

[4] S. Schmiechen, P. Pust, P. J. Schmidt and W. Schnick; Weißes Licht aus Nitriden, *Nachrichten aus der Chemie* **2014**, *62*, 847, doi:10.1002/nadc.201490285.

[5] M. Zeuner, S. Pagano and W. Schnick; Nitridosilicates and oxonitridosilicates: from ceramic materials to structural and functional diversity, *Angew. Chem. Int. Ed.* **2011**, *50*, 7754, doi:10.1002/anie.201005755.

[6] P. Strobel, S. Schmiechen, M. Siegert, A. Tücks, P. J. Schmidt and W. Schnick; Narrow-Band Green Emitting Nitridolithoalumosilicate $Ba[Li_2(Al_2Si_2)N_6]:Eu^{2+}$ with Framework Topology *whj* for LED/LCD-Backlighting Applications, *Chem. Mater.* **2015**, *27*, 6109, doi:10.1021/acs.chemmater.5b02702.

[7] K. Uheda, N. Hirosaki, Y. Yamamoto, A. Naito, T. Nakajima and H. Yamamoto; Luminescence Properties of a Red Phosphor, $CaAlSiN_3:Eu^{2+}$, for White Light-Emitting Diodes, *Electrochem. Solid-State Lett.* **2006**, *9*, H22, doi:10.1149/1.2173192.

[8] P. Eckerlin; Zur Kenntnis des Systems Be_3N_2-Si_3N_4, IV. Die Kristallstruktur von $BeSiN_2$, *Z. Anorg. Allg. Chem.* **1967**, *353*, 225, doi:10.1002/zaac.19673530502.

[9] P. Strobel, V. Weiler, P. J. Schmidt and W. Schnick; $Sr[BeSi_2N_4]:Eu^{2+}/Ce^{3+}$ and $Eu[BeSi_2N_4]$: Nontypical Luminescence in Highly Condensed Nitridoberyllosilicates, *Chem. Eur. J.* **2018**, *24*, 7243, doi:10.1002/chem.201800912.

[10] P. Bielec and W. Schnick; Increased Synthetic Control-Gaining Access to Predicted $Mg_2Si_5N_8$ and beta-$Ca_2Si_5N_8$, *Angew. Chem. Int. Ed.* **2017**, *56*, 4810, doi:10.1002/anie.201701361.

[11] S. Schmiechen, H. Schneider, P. Wagatha, C. Hecht, P. J. Schmidt and W. Schnick; Toward New Phosphors for Application in Illumination-Grade White pc-LEDs: The Nitridomagnesosilicates $Ca[Mg_3SiN_4]:Ce^{3+}$, $Sr[Mg_3SiN_4]:Eu^{2+}$, and $Eu[Mg_3SiN_4]$, *Chem. Mater.* **2014**, *26*, 2712, doi:10.1021/cm500610v.

[12] S. Schmiechen, P. Strobel, C. Hecht, T. Reith, M. Siegert, P. J. Schmidt, . . . W. Schnick; Nitridomagnesosilicate $Ba[Mg_3SiN_4]:Eu^{2+}$ and Structure–Property Relations of Similar Narrow-Band Red Nitride Phosphors, *Chem. Mater.* **2015**, *27*, 1780, doi:10.1021/cm504604d.

[13] R. Shafei, D. Maganas, P. J. Strobel, P. J. Schmidt, W. Schnick and F. Neese; Electronic and Optical Properties of Eu^{2+}-Activated Narrow-Band Phosphors for Phosphor-Converted Light-Emitting Diode Applications: Insights from a Theoretical Spectroscopy Perspective, *J. Am. Chem. Soc.* **2022**, *144*, 8038, doi:10.1021/jacs.2c00218.

[14] O. Kumberger and H. Schmidbaur; Warum ist Beryllium so toxisch?, *Chem. Unserer Zeit* **1993**, *27*, 310, doi:10.1002/ciuz.19930270611.

[15] D. Naglav, M. R. Buchner, G. Bendt, F. Kraus and S. Schulz; Off the Beaten Track-A Hitchhiker's Guide to Beryllium Chemistry, *Angew. Chem. Int. Ed.* **2016**, *55*, 10562, doi:10.1002/anie.201601809.

[16] O. Reckeweg and F. J. DiSalvo; Alkaline earth metal nitride compounds with the composition M_2NX (*M*=Ca, Sr, Ba; *X*=□, H, Cl or Br), *Solid State Sci.* **2002**, *4*, 575, doi:10.1016/s1293-2558(02)01300-6.

[17] BrukerAXS, Billerica, **2016**.

[18] G. M. Sheldrick; Crystal structure refinement with SHELXL, *Acta Crystallogr., Sect. C: Struct. Chem.* **2015**, *71*, 3, doi:10.1107/S2053229614024218.

[19] G. M. Sheldrick; A short history of SHELX, *Acta Crystallogr. Sect. A* **2008**, *64*, 112, doi:10.1107/S0108767307043930.

5 Synthesis and Crystal Structure of the Strontium Beryllate $Sr_3Be_2O_5$

Tobias Giftthaler, Philipp Strobel and Wolfgang Schnick

Abstract: Beryllates show an interesting and diverse structural chemistry, resembling that of well-investigated silicates. The coexistence of tetrahedral and trigonal coordination of Be by O atoms in oxoberyllates allows for an even broader variety of structural motives and implies a plurality of possible atomic ratios Be:O in ternary or higher compounds. We have now synthesized the novel strontium oxoberyllate $Sr_3Be_2O_5$ via a high-temperature high-pressure reaction and have structurally characterized the ternary oxide by single-crystal and powder X-ray diffraction analysis. $Sr_3Be_2O_5$, a low condensed oxoberyllate, contains unprecedented $[Be_2O_5]^{6-}$ double triangles and Sr atoms in both double-capped trigonal-prismatic and octahedral coordination. These motifs show striking resemblance to α-$SrBeO_2$ and SrO, combining their structural properties. Lattice energy (MAPLE) calculations corroborate found parallels to the known phases SrO and α-$SrBeO_2$.

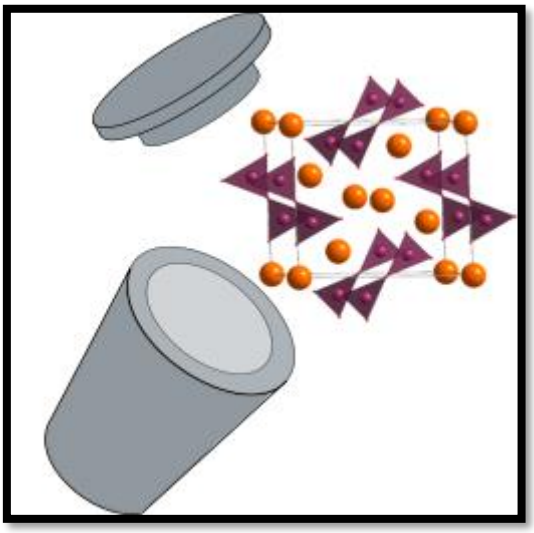

5.1 Introduction

Albeit their structural diversity, matching well-investigated silicates, the chemistry of beryllates is widely unexplored. [1-4] $SrBe_3O_4$, published in 1969, was the only identified ternary phase in the system SrO-BeO until recently.[5-7] This rarity of ternary phases is quite surprising due to the vast amount of structural possibilities and possible compositions allowed by a combination of an anionic $Be_xO_y^{z-}$-network with suitable counterions. As the Be coordination can either be tetrahedral, e.g. in $Sr_{12}Be_{17}O_{29}$, trigonal as in $SrBe_3O_4$ or 3+1 as in BeO, a broad variety of structural motifs is accessible by combination of the different Be-O polyhedra.[8] This diversity is well known from borates, where a variety of ternary compounds with resembling structural motifs has been observed.[9, 10] New compounds are therefore expected to combine these known structural motifs to unrevealed structures.
Herein, we report on the so far least condensed strontium beryllate, namely $Sr_3Be_2O_5$ exhibiting hitherto unknown $[Be_2O_5]^{6-}$ units. The crystal structure was solved and refined from single-crystal X-ray diffraction data and confirmed by Rietveld analysis of powder X-ray diffraction data.

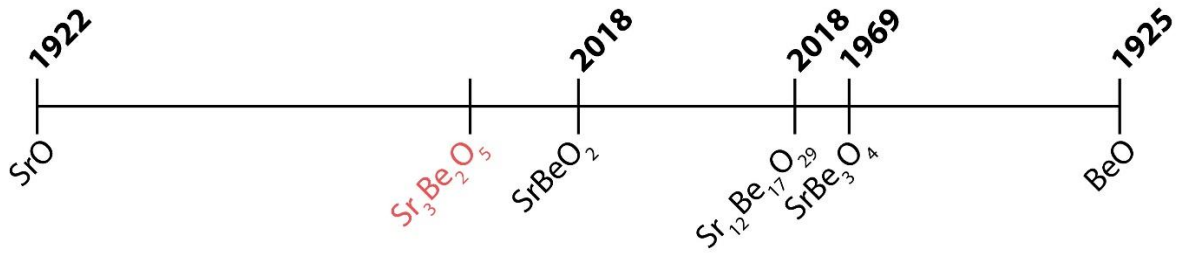

Scheme 1. Hitherto known ternary strontium beryllates in the quasi binary system SrO-BeO with year of first publication.[5, 6, 8]

5.2 Results and Discussion

$Sr_3Be_2O_5$ was synthesized under nitrogen pressure in a hot isostatic press (HIP) starting from SrO and BeO. The target phase could not be obtained by reaction of stoichiometric amounts of SrO and BeO at ambient pressure. Doping with 1 mol% (Eu) resulted in orange crystallites, showing no luminescence at ambient temperature. Non-doped $Sr_3Be_2O_5$ is colorless and transparent.

Rietveld refinement of powder X-ray diffraction data showed a product composition of ≈80 wt.-% $Sr_3Be_2O_5$, ≈20 wt.-% SrO and traces of α/β-$SrBeO_2$, respectively (Fig.1). $Sr_3Be_2O_5$ crystallizes in space group $P2_1/c$ (no. 14). Single crystal structure determination resulted in a monoclinic cell with lattice parameters a = 3.7000(7), b = 9.600(2) and c = 7.900(2) Å, β = 99.00(3)°, Z = 2 and V = 277.15(10) Å^3. Rietveld refinement confirmed the metrics (a = 3.70237(6), b = 9.6069(2) and c = 7.9004(1) Å, β = 99.0076(4)°, V = 277.539(8) Å^3).The structure is illustrated in Figure 2, coordination polyhedra are depicted in Figure 3.

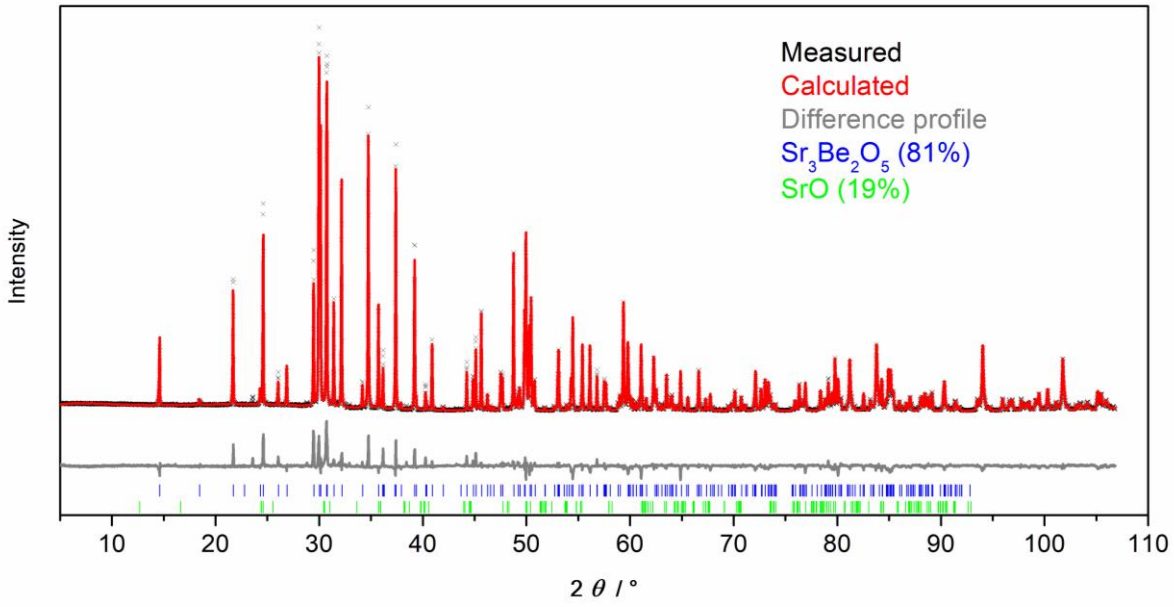

Figure 1. Result of the Rietveld refinement of $Sr_3Be_2O_5$. Powder X-ray diffraction diagram of $Sr_3Be_2O_5$ with the measured data (black crossmarks), pattern based on Rietveld refinement data (red line), difference curve (gray line) and position of allowed Bragg reflections (blue and green bars). Crystallographic data shown in supporting information.

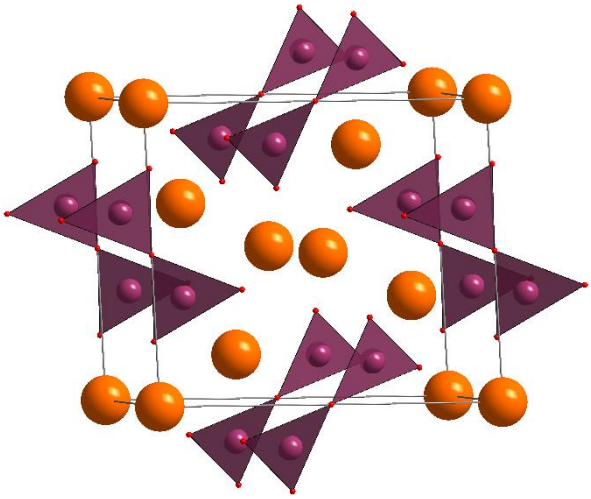

Figure 2. Crystal structure of $Sr_3Be_2O_5$. Sr (orange), Be (violet), O (red).

Two corner sharing BeO_3 triangles form a $[Be_2O_5]^{6-}$ unit with a torsion angle of 9.2°. Sr1 is coordinated by 6+2 O atoms forming a doubly capped trigonal prism. Sr2 is coordinated by six O atoms in a slightly distorted octahedron. The similarity of coordination of Sr1 and Be in $Sr_3Be_2O_5$ to the ones found in α-$SrBeO_2$ and Sr2 in SrO become obvious in direct comparison (Fig.3). Isolated $[Be_2O_5]^{6-}$ units (a) can be seen as sections of the infinite *zweier* single chains of BeO_3-units (b). The Be-O distances of both species are identical within the limits of accuracy and vary between 1.545 and 1.549 Å. Furthermore, corresponding angles differ only slightly. For $Sr_3Be_2O_5$ the corresponding angles vary in the range 118-122° and 113-123° for α-$SrBeO_2$. The 6+2 coordination of Sr1 as found in $Sr_3Be_2O_5$ (c) resembles the Sr coordination in α-$SrBeO_2$ (d). The octahedral coordination of Sr2 by O (e) resembles the surrounding of Sr in SrO (f). While the Sr- O distances in Sr_3BeO_2 are 3-5% smaller at 2.480-2.532 Å compared to 2.605 Å in SrO, the coordination octahedron is distorted. Bond angles are between 84 and 96°. Selected distances and angles are given in the supporting information.

Table 1. MAPLE data of selected Sr-Be-O phases in kj/mol

	$Sr_3Be_2O_5$	α-$SrBeO_2$	SrO
Sr^{2+}	1776-1969	1818	1864
Be^{2+}	2936	2951	
O^{2-}	2155-2464	2160-2458	1864
Total	22495	9387	3727

2 α-$SrBeO_2$ + SrO = 22501 kJ/mol, Δ = 0.3‰

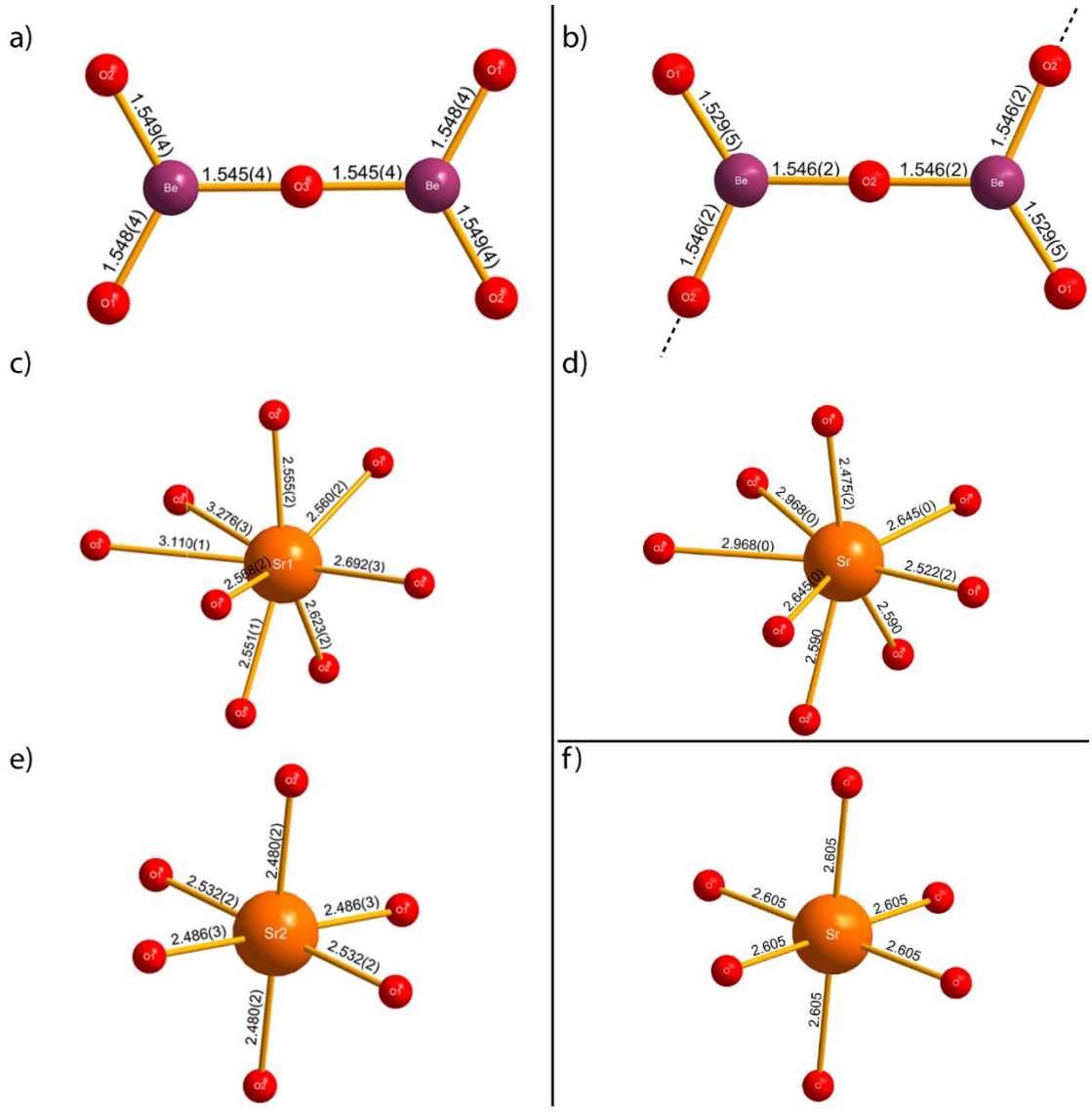

Figure 3. Comparison of cation coordination between $Sr_3Be_2O_5$ (a, c, e) and α-$SrBeO_2$ (b, d)/SrO (f). Sr (orange), Be (violet), O (red). Distances are given in Å.

5.3 Conclusions

Single crystals of $Sr_3Be_2O_5$ were obtained by high-pressure high-temperature synthesis starting from the respective binary oxides in a hot isostatic press. The crystal structure of strontium beryllate $Sr_3Be_2O_5$ contains unprecedented isolated $[Be_2O_5]^{6-}$ units. Surprisingly, oxoberyllates represent a largely unexplored substance class that could exhibit a broad spectrum of unexpected structural features and properties. Besides $[BeO_4]^{6-}$ tetrahedra, especially non-condensed trigonal planar $[BeO_3]^{4-}$ ions are expected to occur.

5.4 Experimental Section

Safety Precautions. Be is considered a highly hazardous element.[14] Be containing dusts are known to cause CBD (chronic beryllium disease) and might be carcinogenic.[15] To minimize the risk of exposure, all operations were performed in closed systems, like Schlenk-lines and gloveboxes.

Synthesis. All starting materials were handled under argon atmosphere in a glovebox (Unilab, MBraun, Garching; O_2<1 ppm, H_2O <1 ppm) due to their moisture sensitivity and the toxicity of Be and most Be containing compounds. The experiments were carried out in a rf-furnace attached to a Schlenk-type vacuum line (10^{-3} mbar) under dried Ar (Air Liquid, 5.0). The atmosphere was purified by passage through columns filled with KOH (Merck, ≥85%), silica gel (Merck), molecular sieve (Fluka, 4 Å), P_4O_{10} (Roth, ≥99%), and titanium sponge (Johnsen Matthey, 99.5%), heated to 730 °C. Crystals of $Sr_3Be_2O_5$ were obtained by reaction of SrO (Alfa Aesar, 46.6 mg, 0.45mmol, 99.5%) and BeO (Alfa Aesar, 7.5 mg, 0.3 mmol, 99.95%) in a hot isostatic press (American Isostatic Presses) under 150 MPa of N_2 atmosphere at 1200 °C. After mixing the starting materials in a tungsten carbide mortar and transferring the mixture into W crucibles it was heated to 1200 °C in 4 h. This temperature was kept for 5 h, then the crucible was cooled to room temperature in 6 h.

Single-crystal X-ray diffraction. Single crystals of $Sr_3Be_2O_5$ were selected and fixed on a micromount. X-ray diffraction data was collected on a Bruker D8 Venture rotary anode diffractometer with Goebel mirror optics for selection and focussing of Mo-Kα radiation (λ = 0.71073 Å, T = 297(2) K). APEX3[16] was used for integration and absorption correction. The crystal structures were solved by Direct Methods (SHELXS)[17] and refined by full-matrix least-squares methods (SHELXL)[18, 19]

Powder X-ray diffraction. The sample was ground and sealed in a glass capillary (Hilgenberg, d = 0.3 mm) and mounted on a rotary head in a STOE STADI P diffractometer (Cu-$K\alpha_1$ radiation, Ge(111) monochromator, Mythen 1k detector) with modified Debye-Scherrer geometry. TOPAS 6 was used for Rietveld refinement.[20]

Elemental analysis. The elemental composition of $Sr_3Be_2O_5$ was determined by energy dispersive X-ray spectroscopy (EDS) on a Dualbeam Helios Nanolab G3 UC scanning electron microscope (SEM, FEI) with X-Max 80 SDD detector (Oxford Instruments). EDS data was obtained at an accelerating voltage of 25 kV from several particles.

5.5 Acknowledgements

We thank Dr. Peter Mayer for collecting single-crystal data, and Christian Minke and Lisa Gamperl (all at Department of Chemistry, LMU Munich) for EDS measurements. Financial support by the Fonds der Chemischen Industrie (FCI) is gratefully acknowledged.

5.6 References

[1] R. Czaya; Refinement of the structure of γ-Ca_2SiO_4, *Acta Crystallogr., Sect. B: Struct. Crystallogr. Cryst. Chem.* **1971**, *27*, 848, doi:10.1107/s0567740871003030.

[2] E. F. Farrell, J. H. Fang and R. E. Newnham; Refinement of the chrysoberyl structure, *Am. Mineral.*, *48*, 804.

[3] F. Liebau, *Structural Chemistry of Silicates*, Springer, Berlin, Heidelberg, **1985**, ISBN:978-3-642-50078-7978-3-642-50076-3

[4] F. Liebau; Silicate und Perowskite: zwei Themen mit Variationen, *Angew. Chem.* **1999**, *111*, 1845, doi:10.1002/(sici)1521-3757(19990614)111:12<1845::Aid-ange1845>3.0.Co;2-4.

[5] L. A. Harris and H. L. Yakel; The crystal structure of $SrBe_3O_4$, *Acta Crystallogr., Sect. B: Struct. Crystallogr. Cryst. Chem.* **1969**, *25*, 1647, doi:doi.org/10.1107/S0567740869004468.

[6] W. Gerlach; Die Gitterstruktur der Erdalkalioxyde, *Z. Phys.* **1922**, 184.

[7] L. A. Harris, R. A. Potter and H. L. Yakel; Preliminary observations of mixed oxide compounds containing BeO, *Acta Crystallogr.* **1962**, *15*, 615, doi:10.1107/s0365110x62001577.

[8] P. Strobel, R. Niklaus, P. J. Schmidt and W. Schnick; Oxoberyllates $SrBeO_2$ and $Sr_{12}Be_{17}O_{29}$ as Novel Host Materials for Eu^{2+} Luminescence, *Chem. - Eur. J.* **2018**, *24*, 12678, doi:10.1002/chem.201801951.

[9] H. Bartl and W. Schuckmann; Zur Struktur des Strontium-Pyroborates $Sr_2B_2O_5$., *Neues Jahrb. Mineral., Monatsh.* **1966**, 253.

[10] J. B. Kim, K. S. Lee, I. H. Suh, J. H. Lee, J. R. Park and Y. H. Shin; Strontium Metaborate, SrB_2O_4, *Acta Crystallogr. Sect. C: Cryst. Struct. Commun.* **1996**, *52*, 498, doi:doi.org/10.1107/S0108270195010341.

[11] R. Hoppe; Madelung Constants, *Angew. Chem. Int. Ed. Engl.* **1966**, *5*, 95, doi:10.1002/anie.196600951.

[12] R. Hübenthal, in *Maple, Program for the Calculation of MAPLE values* 4ed., University of Gießen, Gießen (Germany), **1993**.

[13] R. D. Shannon; Revised effective ionic radii and systematic studies of interatomic distances in halides and chalcogenides, *Acta Crystallogr., Sect. A* **1976**, *32*, 751, doi:10.1107/s0567739476001551.

[14] O. Kumberger and H. Schmidbaur; Warum ist Beryllium so toxisch?, *Chem. Unserer Zeit* **1993**, *27*, 310, doi:10.1002/ciuz.19930270611.

[15] D. Naglav, M. R. Buchner, G. Bendt, F. Kraus and S. Schulz; Off the Beaten Track-A Hitchhiker's Guide to Beryllium Chemistry, *Angew. Chem. Int. Ed.* **2016**, *55*, 10562, doi:10.1002/anie.201601809.

[16] BrukerAXS, Billerica, **2016**.

[17] G. M. Sheldrick, University of Göttingen **1997**.

[18] G. M. Sheldrick; Crystal structure refinement with SHELXL, *Acta Crystallogr., Sect. C: Struct. Chem.* **2015**, *71*, 3, doi:10.1107/S2053229614024218.

[19] G. M. Sheldrick, University of Göttingen **1997**.

[20] A. A. Coelho, in *TOPAS Academic*, 6 ed., Brisbane (Australia), **2016**.

6 Introducing Ternary Thioberyllates – Na_2BeS_2

Tobias Giftthaler, Robert Calaminus, Sascha Harm, Bettina V. Lotsch and Wolfgang Schnick*[a]

Abstract: Sodium ion conduction has become a focal point of battery cell research. Especially, sulfides show remarkable potential for this application. However, thioberyllates were mostly neglected, due to the toxicity of beryllium. In this contribution we characterize Na_2BeS_2, the first member of the compound class of ternary thioberyllates. Synthesized from the respective sulfides in a high-temperature reaction, Na_2BeS_2 was obtained as yellow crystals. It crystallizes in the K_2SiP_2 structure type, as shown by single-crystal and powder X-ray diffraction experiments. Na_2BeS_2 is a mixed ionic – electronic conductor with a transference number of 0.67 and a sodium ion conductivity of $3.3 \cdot 10^{-9}$ S/cm at 25 °C, which makes the substance class of thioberyllates interesting candidates of future research in fields where Na transport is an asset.

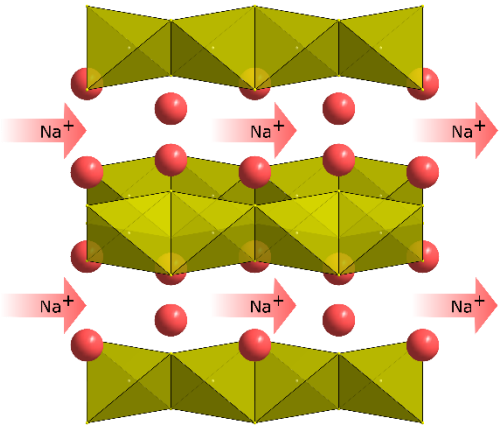

6.1 Introducing Ternary Thioberyllates – Na_2BeS_2

Mixed ionic – electronic conductors (MIEC) gained increasing attention in recent years. Their multiple applications in energy conversion and storage, memory devices and sensing put them in the focus of current research.[1-2]
Especially combined with the turn from lithium to sodium as the more sustainable material, this can reduce the technological reliance on limited resources and focus on a more earth-abundant element.[3-4] However, the usage of sodium requires powerful sodium-based MIECs.[5-6] In search for sodium conducting materials sulfides and thio-compounds such as the ortho-thiophosphate Na_3PS_4 show high potential.[7] The ion conductivity of ortho-thiophosphate can even be enhanced by aliovalent substitution of P by Al or Si, as this can influence diffusion pathways as well as the charge carrier concentration and the polarizability of the overall lattice. For example, this was shown by and studied with the synthesis and characterization of Na_5AlS_4 and Na_4SiS_4.[8] Given the fact that so far Be and its thio-compounds were mostly neglected in research due to their toxicity, the motivation for a search for a beryllium analog was evident.[9] Beryllium, as known from its oxides and nitrides, can be found in either trigonal planar or tetrahedral coordination, which can possibly expand the structural variety in thio-compounds.[10-11] Furthermore, the desired "Na_6BeS_4" was expected to improve ion conductivity compared to related Si or Al ortho-thio-compounds, as Be^{2+} carries a smaller charge compared to Al^{3+} and Si^{4+} and therefore increases the charge carrier concentration of the mobile ion, the lattice polarizability, and therefore, the lattice softness.
In search for the suspected "Na_6BeS_4" with a degree of condensation of $\kappa = 0.25$, we found the higher condensed Na_2BeS_2 with a degree of condensation of $\kappa = 0.5$.[12]

$$Na_2S + Be + S \rightarrow Na_2BeS_2 \qquad \text{(Eq 1)}$$

Na_2BeS_2 was obtained as a yellow powder and is sensitive towards air and moisture. It was synthesized starting from Be, S and Na_2S, as given in the chemical equation Eq1. The precursors were finely ground with a 10% excess of S and heated to 600 °C for 72 h. Detailed information regarding the synthesis can be found in the supporting information.

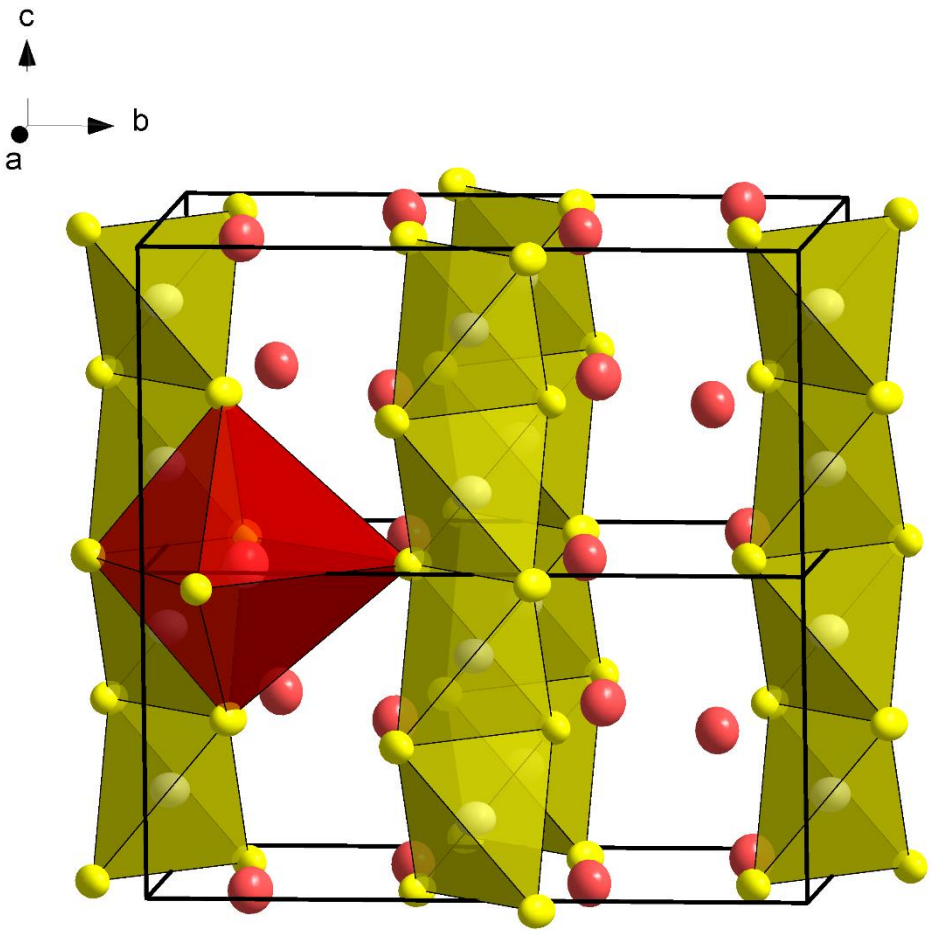

Figure 1. Crystal structure of Na_2BeS_2. Two units cells of the crystal structure of Na_2BeS_2, S (yellow) forms octahedral coordination of Na (red) and tetrahedral coordination of Be (gray). Columns of edge sharing $[BeS_4]$-tetrahedra along [001]. All atoms are depicted as ellipsoids at 95% probability level.

The crystal structure of Na_2BeS_2 was solved and refined based on single-crystal X-ray diffraction data (R_1 = 0.037, details in supporting information) and confirmed by Rietveld refinement (see supporting information Table S5, Figure S2).[13-16] Na_2BeS_2 crystallizes in the orthorhombic space group *Ibam*.[17] It is isotypic to K_2SiP_2, with a measure of similarity (Δ) of 0.042.[18-19] The unit cell with lattice parameters *a* = 6.0015(4), *b* = 11.1701(7) and *c* = 5.5179(4) Å contains four formula units. It exhibits columns of edge sharing $[BeS_4]^{6-}$ tetrahedra, running along *c*. The small measure of similarity, showing small deviation of atomic parameters from the aristotype, indicates structure direction by the Be–S columns, as the difference in ionic radii between Na^+ (in Na_2BeS_2) and K^+ (in K_2SiP_2) has minor influence on the crystal structure. With respect to the tetrahedral coordination of Be and the given structure direction by Be–S columns, Na_2BeS_2 can be characterized as the first ternary thioberyllate.

Na atoms are found in largely distorted [NaS_6] octahedra in between the columns. These octahedra can also be described as a 5+2+1 coordination by 5 close-by S^{2-} ions, with 2 Be^{2+} and 1 further S^{2-} atom in the second coordination sphere. According to Pauling's second rule, this might reduce the bond energy and subsequently lead to the observed sensitivity towards air and moisture.[20-21]

The characterization as a thioberyllate is supported by calculation of the Madelung part of lattice energy, which was found to be 6679.9 kJ/mol, deviating just 1.7% from the sum of Madelung lattice energies of the respective binary sulfides BeS and Na_2S. Due to the known side phases BeO and BeS, bulk composition analysis *via* CHNS or ICP gives no further information on the composition of the targeted phase. Additionally, the given moisture sensitivity and potential toxicity disqualifies EDS and NMR, as the sample is briefly exposed to air during sample transfer.

The applicability of Na_2BeS_2 for sodium ion conduction was determined by electrochemical impedance spectroscopy as well as chronopotentiometry.

Electrochemical impedance spectroscopy of a cold-pressed sample of Na_2BeS_2 shows that the sample is a mixed ionic electronic conductor (ionic transference number t_{ion} = 0.67). This is evident in the Nyquist diagram (Figure 2) by the presence of a semicircle with simultaneous absence of a polarisation tail.[22] Therefore, an equivalent circuit comprising an ionic and electronic conduction process was used for fitting, resulting in a total ionic conductivity of $\sigma_{ion} = 3.3 \cdot 10^{-9}$ S/cm and an electronic conductivity of $\sigma_{eon} = 1.6 \cdot 10^{-9}$ S/cm at 25 °C. These values are in good agreement with those obtained from chronopotentiometry (Figure S3, $\sigma_{eon} \leq 1.2 \cdot 10^{-9}$ S/cm, $\sigma_{total} = 2.3 \cdot 10^{-9}$ S/cm and $\sigma_{ion} \geq 1.2 \cdot 10^{-9}$ S/cm). Since no steady state was achieved during the measurement, the electronic conductivity derived from chronopotentiometry can be seen as the upper limit.

Temperature-dependent EIS measurements (Figure 2) allow the calculation of activation energies of $E_{a,ion}$ = 0.092(±0.010) eV for the ionic conductivity and $E_{a,eon}$ = 0.599(±0.013) eV for the electronic conductivity using the Arrhenius equation. The activation energy of the ionic conduction is surprisingly low. While the measurements seem consistent, it cannot be ruled out with absolute certainty that the value is influenced by overlap of bulk and grain boundary processes, a measuring error, or a fitting error.

Although being over one order of magnitude smaller than comparable thiosilicates and –aluminates, the ionic conductivity shows the potential of thioberyllates as mixed or purely ionic conductors in general. However, it has to be considered that ionic conductivities are difficult to compare between different classes of compounds because they are influenced by several factors, including particle size, measurement method and even measurement setup.[23] Nevertheless, iso- and especially aliovalent substitutions and alternative synthetic

routes such as ball-milling are expected to be expedient strategies to further systematically optimize the ionic conductivity.

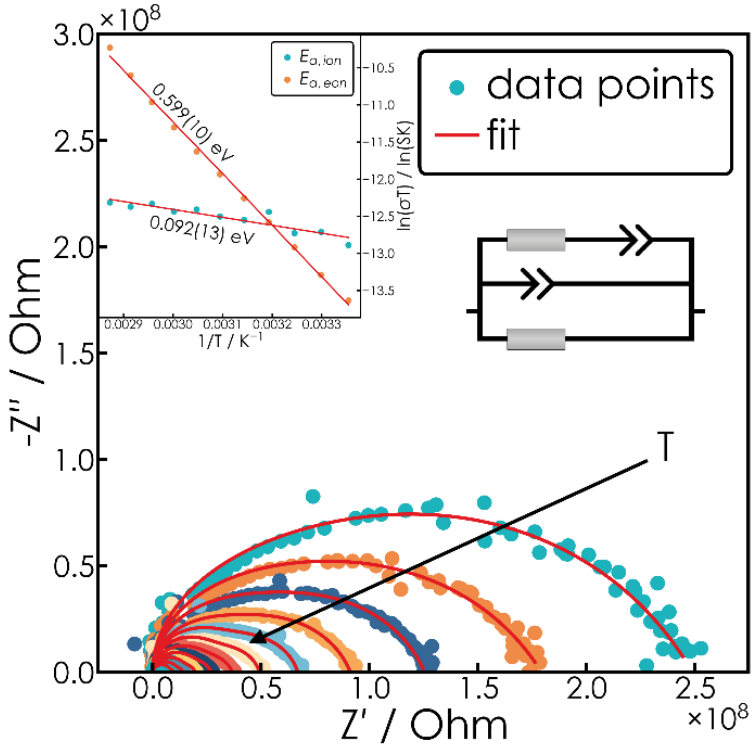

Figure 2. Electrochemical impedance spectroscopy. A cold pressed sample of Na_2BeS_2 was measured at 25 °C and the data (black dots) were fitted in a Nyquist diagram as a semicircle (red) to determine the capacitance. Details can be found in supporting information.

In summary, we showed that the novel substance class of ternary thioberyllates, represented by its first member Na_2BeS_2, carries great potential for further investigation. The accessibility through high temperature synthesis, starting from readily available precursors or even the elements, in this case Na_2S, Be and S, allows for a broad explorative search for unknown compounds. As the first member of this substance class already exhibits significant ion conduction properties, future investigations can focus either on the further expansion of the given substance class or on the detailed research of mixed phases with other network building anions. The further search for a hypothetical phase "Na_6BeS_4" as well as the interplay between thioberyllate phases with proven Na conducting phases, giving rise to solid solutions with the general composition $Na_{6-(x+y)}Be_{1-(x+y)}Si_xAl_yS_4$, is expected to deliver important insights into the structure-property relations of potentially new

ion conducting phases. Furthermore, rare earth doped alkaline earth thioberyllates might be of interest as phosphors for solid-state light conversion as sulfides already are in broad application as phosphors.[24]

6.2 Acknowledgements

The authors would like to thank the German Federal Ministry of Education and Research (BMBF) and the DFG Cluster of Excellence e-conversion for their financial support through the FestBatt project 03XP0430B and the grant EXC2089, respectively.

6.3 References

[1] Z. Shao, S. M. Haile, *Nature* **2004**, *431*, 170-173.

[2] M. Acosta, F. Baiutti, A. Tarancón, J. L. MacManus-Driscoll, *Adv. Mater. Interfaces* **2019**, *6*.

[3] N. Yabuuchi, K. Kubota, M. Dahbi, S. Komaba, *Chem. Rev.* **2014**, *114*, 11636-11682.

[4] M. D. Slater, D. Kim, E. Lee, C. S. Johnson, *Adv. Funct. Mater.* **2013**, *23*, 947-958.

[5] R. Berthelot, D. Carlier, C. Delmas, *Nat. Mater.* **2011**, *10*, 74-80.

[6] F. Sauvage, L. Laffont, J. M. Tarascon, E. Baudrin, *Inorg. Chem.* **2007**, *46*, 3289-3294.

[7] M. Jansen, U. Henseler, *J. Solid State Chem.* **1992**, *99*, 110-119.

[8] S. Harm, A. K. Hatz, C. Schneider, C. Hoefer, C. Hoch, B. V. Lotsch, *Front. Chem.* **2020**, *8*, 90.

[9] M. R. Buchner, *Z. Naturforsch., B* **2020**, *75*, 405-412.

[10] L. A. Harris, R. A. Potter, H. L. Yakel, *Acta Crystallogr.* **1962**, *15*, 615-616.

[11] E. Elzer, M. Weidemann, W. Schnick, *Eur. J. Inorg. Chem.* **2021**, *2021*, 4979-4983.

[12] The degree of condensation κ is given by the ratio of cationic tetrahederal centers to coordinating anions.

[13] BrukerAXS, Billerica, **2016**.

[14] A. A. Coelho, in *TOPAS Academic*, 6 ed., Brisbane (Australia), **2016**.

[15] G. M. Sheldrick, *Acta Crystallogr. Sect. A* **2008**, *64*, 112-122.

[16] G. M. Sheldrick, *Acta Crystallogr., Sect. C: Struct. Chem.* **2015**, *71*, 3-8.

[17] Deposition number 2302593 contains the supplementary crystallographic data for this paper. These data are provided free of charge by the joint Cambridge Crystallographic Data Centre and Fachinformationszentrum Karlsruhe Access Structures service. .

[18] B. Eisenmann, M. Somer, *Z. Naturforsch., B: Chem. Sci.* **1984**, *39*, 736-738.

[19] G. Bergerhoff, M. Berndt, K. Brandenburg, T. Degen, *Acta Crystallogr. Sect. B: Struct. Sci.* **1999**, *55*, 147-156.

[20] L. Pauling, *J. Am. Chem. Soc.* **1929**, *51*, 1010-1026.

[21] J. R. Glenn, J. B. Cho, Y. Wang, A. J. Craig, J. H. Zhang, M. Cribbs, S. S. Stoyko, K. E. Rosello, C. Barton, A. Bonnoni, P. Grima-Gallardo, J. H. MacNeil, J. M. Rondinelli, J. I. Jang, J. A. Aitken, *Dalton Trans.* **2021**, *50*, 17524-17537.

[22] R. A. Huggins, *Ionics* **2002**, *8*, 300-313.

[23] S. Ohno, T. Bernges, J. Buchheim, M. Duchardt, A.-K. Hatz, M. A. Kraft, H. Kwak, A. L. Santhosha, Z. Liu, N. Minafra, F. Tsuji, A. Sakuda, R. Schlem, S. Xiong, Z. Zhang, P. Adelhelm, H. Chen, A. Hayashi, Y. S. Jung, B. V. Lotsch, B. Roling, N. M. Vargas-Barbosa, W. G. Zeier, *ACS Energy Lett.* **2020**, *5*, 910-915.

[24] P. F. Smet, I. Moreels, Z. Hens, D. Poelman, *Materials* **2010**, *3*, 2834-2883.

7 Summary

7.1 Green-Emitting Oxonitridoberyllosilicate $Ba[BeSiON_2]:Eu^{2+}$ for Wide Gamut Displays

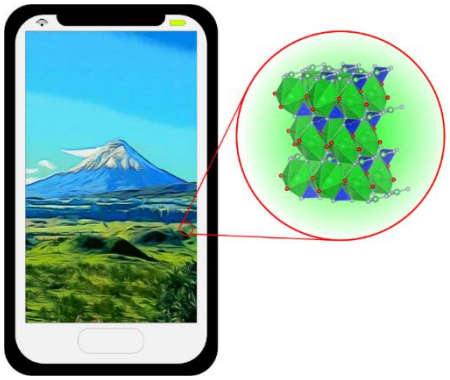

In this contribution, the unprecedented class of oxonitridoberyllosilicates is presented with its first member, $BaBeSiON_2$ (BBS). It is synthesized from industrially available starting materials. The structure of BBS is elucidated through a combination of X-ray and NMR measurements and features layers of $[SiON_3]$ tetrahedra connected by trigonal planar $[BeN_3]$ units. Upon doping with Eu^{2+}, BBS shows green luminescence with an emission wavelength of 526 nm and a *fwhm* of 1600 cm^{-1}. This makes BSS an outstanding phosphor for application in LED backlit LCD devices, where it helps to expand the covered color gamut.

7.2 Blue Emitting $SrBe_{1-x}Si_{2+x}O_{3-2x}N_{2+2x}:Eu^{2+}$ (x ≈ 0.1)

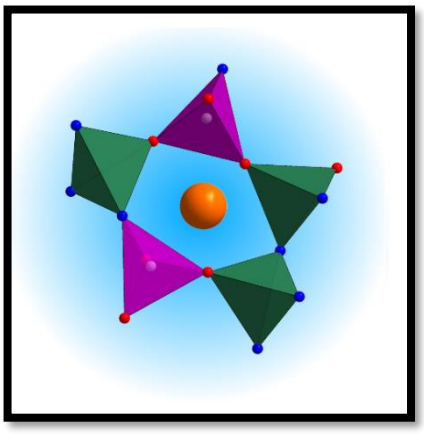

This contribution presents the second known oxonitridoberyllosilicate $SrBe_{1-x}Si_{2+x}O_{3-2x}N_{2+2x}:Eu^{2+}$($x \approx 0.1$), called SBS. The pale blue powder is synthesized at high temperatures from Sr_2N, BeO, SiO_2, Si_3N_4 and EuF_3. Under UV irradiation, it emits blue light at 465 nm. The crystal structure of SBS is an ordered variant of the $LaSi_3N_5$ structure type and therefore isotypic to the oxonitridoalumosilicate $SrSiAl_2O_3N_2$. The altered emission of SBS in comparison to the related alumo-compound shows a new pathway for phosphor fine-tuning.

7.3 The Nitridoberyllosilicate System AE$BeSi_2N_4$ (AE = Ca, Ba)

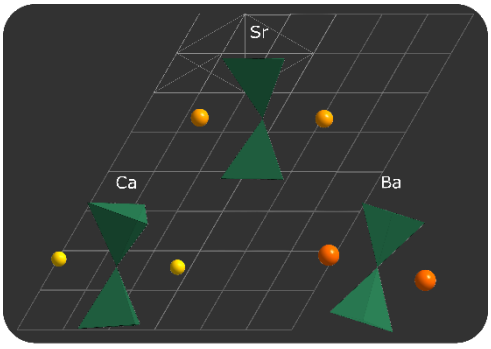

$CaBeSi_2N_4$ and $BaBeSi_2N_4$, presented in this contribution, expand the class of nitridoberyllosilicates. Both compounds are yielded from a high-temperature synthesis. The crystal structures of all three known *AE*$BeSi_2N_4$ (*AE* = Ca, Sr, Ba) phases are closely related. All show trigonal planar [BeN_3] units and [Si_2N_7] double tetrahedra. The different ionic radii of the alkaline earth cations lead to the adaption of these structural motifs. This highlights the resemblance between nitridosilicates and nitridoberyllosilicates.

7.4 Synthesis and Crystal Structure of the Strontium Beryllate $Sr_3Be_2O_5$

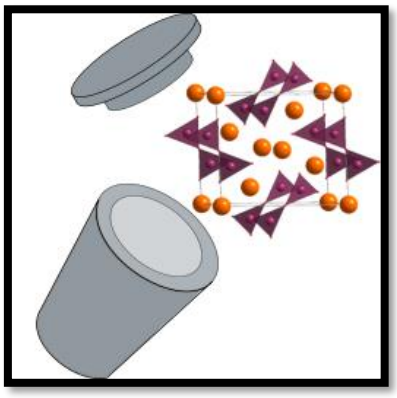

In the quasi-binary system SrO–BeO, a new strontium-rich compound $Sr_3Be_2O_5$ is presented. Colorless crystals of $Sr_3Be_2O_5$ were synthesized from SrO and BeO in a hot isostatic press at elevated pressure and high temperatures. The structure of $Sr_3Be_2O_5$ is elucidated by single crystal X-ray diffraction data. It consists of vertex sharing, trigonal planar [BeO_3] units, forming [Be_2O_5] doubles. Sr is found in an octahedral coordination. The structure of $Sr_3Be_2O_5$ can be derived from the related α-$SrBeO_2$ and SrO.

7.5 Introducing Ternary Thioberyllates – Na_2BeS_2

This contribution introduces Na_2BeS_2, the first ternary thioberyllate. The synthesis starting from Na_2S, Be and S, yields a pale yellow powder, that is sensitive to air and moisture. Na_2BeS_2 crystallizes in the K_2SiP_2 structure type, with columns of corner-sharing $[BeS_4]$ tetrahedra. The sodium atoms, in octahedral coordination, are highly mobile. Therefore, Na_2BeS_2 is a mixed ionic electronic conductor with a remarkably small activation energy for ion conduction.

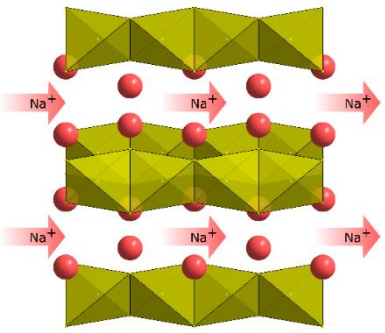

8 Concluding Remarks and Outlook

This thesis aims to study different application-related solid state compound classes with the common denominator beryllium. Fundamental and applied investigations are combined, while various preparational and analytical methods are exercised. The Chapters 2-4 focus on oxonitridoberyllosilicates, their high-temperature synthesis and the importance of their respective structural characteristics for possible applications. The subsequent Chapters 5 and 6 cover ternary chalkogenidoberyllates. Herein, the synthesis as well as structure elucidation are discussed and, in case of Na_2BeS_2, ion conduction properties are investigated.

The following chapter intends to elaborate the scientific relevance of these findings in the context of current and possible future research in addition to the separate discussions in the respective chapters. The three major issues stated at the beginning of this thesis serve as a guide for the discussion.

8.1 Oxonitridoberyllosilicates for pcLED Backlit Displays

The initially stated demand for a green phosphor, which is applicable in pcLEDs as display backlight, was discussed in detail in Chapter 2. The synthesized $Ba[BeSiON_2]$ (BBS) represents a new substance class of oxonitridoberyllosilicates and shows green emission upon doping with Eu^{2+}. With a narrow-band emission reaching its maximum at 526 nm, it meets the requirements for green phosphors in display backlights. As shown in Chapter 2, the occurrence of the desired efficient green emission in a thermally and chemically stable compound is unprecedented. The combined fulfillment of all requirements makes it the best available phosphor for application. Due to the low mass proportion of Be (4 wt.%) and the high chemical stability of BBS, technical implementation is not limited by the beryllium content.

The challenges for industrial application lie in the synthesis optimization and the usage of BeO as a starting material instead. It is known that optimized crystallite growth and their resulting habitus can further improve luminescence properties. Therefore, synthesis optimization is a common industrial process.[1] With respect to the health risks posed by

BeO, stated in Chapter 1.2.2, additional safety standards are required for BBS production. Nevertheless, BeO is already used on a large scale and handled industrially.[2] The resulting applicability of BBS gives a benchmark for pcLED backlit liquid crystal displays (LCD). In context of alternative display technologies like OLED (organic LED) and QLED (quantum dot converted LED backlit LCD), the competitiveness of pcLED based technologies shows that the research in phosphors is worth expanding.[3, 4]

Aside from the application-relevant materials properties, the class of oxonitridoberyllosilicates can be put in broader perspective from a structural point of view. $Ba[Si_2O_2N_2]$ can be structurally derived from $Ba[BeSiON_2]$ through formal substitution of half of the $[SiON_3]$ tetrahedra by trigonal planar $[BeN_3]$ units. However, this $[SiON_3]$ tetrahedron with a terminal O atom is no unique structural motif of $Ba[Si_2O_2N_2]$ and can be found in other SiAlONs as well.[5-7] Therefore, one possible pathway in future investigations aiming for structural expansion of the broader SiAlON compound class, may be the introduction of Be^{2+} into their structure chemistry, in substitution of a isovalent $[Si\text{-}O]^{2+}$ unit.

8.2 Beryllium in red pcLED Phosphors

In Chapter 4 the nitridoberyllosilicates $Ca[BeSi_2N_4]$ and $Ba[BeSi_2N_4]$ are presented. The structural relation between the $AE[BeSi_2N_4]$ phases (*AE* = Ca, Sr, Ba) is discussed and it is shown that different cationic radii of the alkaline-earth counter ions lead to an adaption of the anionic network. While topographical motifs remain preserved, the coordination sphere and symmetry of the cationic site change significantly. Therefore, instead of the orange nontypical emission of $Sr[BeSi_2N_4]:Eu^{2+}$, $Ba[BeSi_2N_4]:Eu^{2+}$ shows red emission comparable to $Ba_2Si_5N_8:Eu^{2+}$.[8] This effect of network adaption to the cation radius and subsequently altered luminescence is known from nitridosilicates systems like $AE_2[Si_5N_8]$.[9-12] It is herein presented for nitridoberyllosilicates, highlighting the analogies between these two compound classes. This is a first indication that general principles for nitridosilicates might also apply in the related Be containing class. This makes it all the more interesting to find further ways to change structures and subsequently properties in (oxo)nitridoberyllates.

Chapter 3 introduces the blue emitting oxonitridoberyllosilicate $Sr[BeSi_2O_3N_2]:Eu^{2+}$. Its structure is isotypic to the known $SrSiAl_2O_3N_2:Eu^{2+}$.[13] However, upon blue or UV irradiation $Sr[BeSi_2O_3N_2]:Eu^{2+}$ emits light at shorter wavelengths in comparison to the alumosilicate.[14] In this context, the net-isovalent substitution of combinations in the expanded spectrum of

network building cations Li-Al-Si-P by Be represents a new way of phosphor fine tuning, especially relevant for the red spectral region with already highly sophisticated materials in application. Without interfering with the network building structure and the involved anion composition, the first coordination sphere of the activator ion remains untouched. As shown in the system $SrBeSi_2O_3N_2:Eu^{2+}$/$SrSiAl_2O_3N_2:Eu^{2+}$, the change in the second coordination sphere leads to slightly different emission. In case of phosphor optimization, this might be highly beneficial. Industrially applied phosphors like $Sr[LiAl_3N_4]:Eu^{2+}$ conventionally are tuned by cation-balanced anion substitution, in this case to $Sr[Li_2Al_2O_2N_2]:Eu^{2+}$ or substitution of the counterion as in $AE[Si_2O_2N_2]:Eu^{2+}$ (*AE* = Ca, Sr, Ba).[15-17] The presented pathway may be applied in a complementary or substitutive way. For instance, in the lithonitridoaluminate $Sr[LiAl_3N_4]$, the net-isovalent formal substitution to an hypothetical "$AE[Be_2Al_2N_4]$" (*AE* = Ca, Sr) seems feasible, considering the existing $Sr_2[BeAl_3N_5]$ and $Ca[LiAl_3N_4]$.[18]

8.3 Thioberyllates in solid state ion conduction

The first thioberyllate Na_2BeS_2 presented in Chapter 6 exhibits columns of condensed $[BeS_4]$ tetrahedra and sodium in octahedral voids. The sodium ion conductivity is found to be $3.3 \cdot 10^{-9}$ S/cm at 25 °C. While this is by no means extraordinary, the calculated activation energy $E_{a,ion}$ = 0.092(±0.010) eV is remarkably low in comparison to other solid sodium electrolytes.[19-21]

As Na_2BeS_2 marks the starting point to thioberyllate chemistry, future investigations might expand this compound class. The inherent challenge for expansion in new compound classes is the lack of structural systematics and synthetic guidelines. A view at the lighter homologues compared to sulfides, might help at this point, since oxoberyllates have been studied at least to a small extent.

In Chapter 5, the structure of $Sr_3Be_2O_5$ is presented. Its corner sharing trigonal planar $[BeO_3]$ units are a recurring motif in strontium beryllates, alongside corner and edge sharing $[BeO_4]$ tetrahedra.[22, 23] This combination is also found in other beryllates as the sodium containing $Na_2[BeO_2]$ and $Na_6Be_8O_{11}$ and leads to a large variety of structures in this compound class.[24, 25] Hence, the related thioberyllates are offered a wide range of structural options. In contrast to oxides, however, the expression of corresponding trigonal planar $[BeS_3]$ units is unlikely, due to the relation of anionic to cationic radii.[26, 27] Nonetheless, this structural

motif, condensed or isolated, would be highly interesting. The easier accessible, already observed [BeS_4] tetrahedra, are expected to be found in various degrees of condensation and interconnections. In particular, the search for further sodium thioberyllates, as the desired "Na_6BeS_4", might lead to a thioberyllate with isolated [BeS_4] tetrahedra. Such low-condensed thioberyllates are of special interest for application as ion conductors[28].
Additionally, the low activation energy for ion conduction calculated for Na_2BeS_2 is likely due to the polarizability of the Be-S network.[29, 30] Therefore, it is expected to be found in other thioberyllates as well. In combination with the anticipated structural variety this makes thioberyllates in general a highly promising compound class.

8.4 Final Remarks

The introduction of beryllium to oxides, nitrides and sulfides was shown in this thesis to be highly promising in terms of structural chemistry and application. On the one hand, an actually applicable phosphor was found and on the other hand, pathways for future investigations on new compound classes were drawn. The structural diversity in oxonitridoberyllates and, in the broader context, Be-Si-Al-P-O-N-S-compounds allows for a broad variety of properties to be expected. Especially considering high-pressure investigations, it is obvious that the structural possibilities and feasible motifs are far from being studied completely. The understanding of network building structures and resulting properties based on the increased structural variety will subsequently lead to further expansion of solid state chemistry, or as *Victor Hugo* put it: "Scientists have searched for a perpetuum mobile; they have found it: it is science itself."

8.5 References

[1] W. M. Yen, S. Shionoya and H. Yamamoto, *Phosphor Handbook*, Taylor & Francis Group, Boca Raton, **2007**, ISBN:0-8493-3564-7

[2] K. A. Walsh, *Beryllium Chemistry and Processing*, ASM International, Materials Park, OH, **2009**, ISBN:0-87170-721-7

[3] J. Bauri, R. B. Choudhary and G. Mandal; Recent advances in efficient emissive materials-based OLED applications: a review, *J. Mater. Sci.* **2021**, *56*, 18837, doi:10.1007/s10853-021-06503-y.

[4] Y. Sun, Y. Jiang, X. W. Sun, S. Zhang and S. Chen; Beyond OLED: Efficient Quantum Dot Light-Emitting Diodes for Display and Lighting Application, *Chem. Rec.* **2019**, *19*, 1729, doi:10.1002/tcr.201800191.

[5] R. Lauterbach and W. Schnick; High-temperature synthesis and single-crystal X-ray structure determination of $Sr_{10}Sm_6Si_{30}Al_6O_7N_{54}$ — a layered sialon with an ordered distribution of Si, Al, O, and N, *Solid State Sci.* **2000**, *2*, 463, doi:10.1016/S1293-2558(00)00147-3.

[6] C. Maak, C. Hoch, P. J. Schmidt and W. Schnick; Oxonitridosilicate Oxides $RE_{26}Ba_6[Si_{22}O_{19}N_{36}]O_{16}:Eu^{2+}$ (*RE* = Y, Tb) with a Unique Layered Structure and Orange-Red Luminescence for *RE* = Y, *Inorg. Chem.* **2018**, *57*, 2242, doi:10.1021/acs.inorgchem.7b03124.

[7] C. Maak, R. Niklaus, F. Friedrich, A. Mähringer, P. J. Schmidt and W. Schnick; Efficient Yellow-Orange Phosphor $Lu_4Ba_2[Si_9ON_{16}]O:Eu^{2+}$ and Orange-Red Emitting $Y_4Ba_2[Si_9ON_{16}]O:Eu^{2+}$: Two Oxonitridosilicate Oxides with Outstanding Structural Variety, *Chem. Mater.* **2017**, *29*, 8377, doi:10.1021/acs.chemmater.7b02900.

[8] H. A. Höppe, H. Lutz, P. Morys, W. Schnick and A. Seilmeier; Luminescence in Eu^{2+}-doped $Ba_2Si_5N_8$: fluorescence, thermoluminescence, and upconversion, *J. Phys. Chem. Solids* **2000**, *61*, 2001, doi:10.1016/s0022-3697(00)00194-3.

[9] T. Schlieper, W. Milius and W. Schnick; Nitrido-Silicates. II. High Temperature Syntheses and Crystal Structures of $Sr_2Si_5N_8$ and $Ba_2Si_5N_8$, *Z. Anorg. Allg. Chem.* **1995**, *621*, 1380, doi:10.1002/zaac.19956210817.

[10] H. Huppertz and W. Schnick; Eu2Si5N8and EuYbSi4N7. The First Nitridosilicates with a Divalent Rare Earth Metal, *Acta Crystallographica Section C Crystal Structure Communications* **1997**, *53*, 1751, doi:10.1107/s0108270197008767.

[11] P. Bielec and W. Schnick; Increased Synthetic Control-Gaining Access to Predicted $Mg_2Si_5N_8$ and beta-$Ca_2Si_5N_8$, *Angew. Chem. Int. Ed.* **2017**, *56*, 4810, doi:10.1002/anie.201701361.

[12] M. Zeuner, P. J. Schmidt and W. Schnick; One-Pot Synthesis of Single-Source Precursors for Nanocrystalline LED Phosphors $M_2Si_5N_8:Eu^{2+}$ (M = Sr, Ba), *Chem. Mater.* **2009**, *21*, 2467, doi:10.1021/cm900341f.

[13] R. Lauterbach and W. Schnick; Synthese, Kristallstruktur und Eigenschaften eines neuen Sialons - $SrSiAl_2O_3N_2$, *Z. Anorg. Allg. Chem.* **1998**, *624*, 1154, doi:10.1002/(SICI)1521-3749(199807)624:7<1154::AID-ZAAC1154>3.0.CO;2-P.

[14] X. Wang, Z. Zhao, Q. Wu, Y. Li, C. Wang, A. Mao and Y. Wang; Synthesis, structure, and luminescence properties of $SrSiAl_2O_3N_2:Eu^{2+}$ phosphors for light-emitting devices and field emission displays, *Dalton Trans.* **2015**, *44*, 11057, doi:10.1039/c5dt00800j.

[15] G. J. Hoerder, M. Seibald, D. Baumann, T. Schröder, S. Peschke, P. C. Schmid, . . . H. Huppertz; $Sr[Li_2Al_2O_2N_2]:Eu^{2+}$-A high performance red phosphor to brighten the future, *Nat. Commun.* **2019**, *10*, 1824, doi:10.1038/s41467-019-09632-w.

[16] P. Pust, V. Weiler, C. Hecht, A. Tucks, A. S. Wochnik, A. K. Henss, . . . W. Schnick; Narrow-band red-emitting $Sr[LiAl_3N_4]:Eu^{2+}$ as a next-generation LED-phosphor material, *Nat. Mater.* **2014**, *13*, 891, doi:10.1038/nmat4012.

[17] V. Bachmann, C. Ronda, O. Oeckler, W. Schnick and A. Meijerink; Color Point Tuning for $(Sr,Ca,Ba)Si_2O_2N_2:Eu^{2+}$ for White Light LEDs, *Chem. Mater.* **2008**, *21*, 316, doi:10.1021/cm802394w.

[18] E. Elzer, P. Strobel, V. Weiler, P. J. Schmidt and W. Schnick; Illuminating Nitridoberylloaluminates: The Highly Efficient Red-Emitting Phosphor $Sr_2[BeAl_3N_5]:Eu^{2+}$, *Chem. Mater.* **2020**, *32*, 6611, doi:10.1021/acs.chemmater.0c02037.

[19] W. D. Richards, T. Tsujimura, L. J. Miara, Y. Wang, J. C. Kim, S. P. Ong, . . . G. Ceder; Design and synthesis of the superionic conductor $Na_{10}SnP_2S_{12}$, *Nat. Commun.* **2016**, *7*, 11009, doi:10.1038/ncomms11009

[20] N. Tanibata, K. Noi, A. Hayashi and M. Tatsumisago; Preparation and characterization of highly sodium ion conducting Na_3PS_4–Na_4SiS_4 solid electrolytes, *RSC Adv.* **2014**, *4*, 17120, doi:10.1039/c4ra00996g.

[21] S. Harm, A. K. Hatz, C. Schneider, C. Hoefer, C. Hoch and B. V. Lotsch; Finding the Right Blend: Interplay Between Structure and Sodium Ion Conductivity in the System Na_5AlS_4-Na_4SiS_4, *Front. Chem.* **2020**, *8*, 90, doi:10.3389/fchem.2020.00090.

[22] L. A. Harris and H. L. Yakel; The crystal structure of $SrBe_3O_4$, *Acta Crystallogr., Sect. B: Struct. Crystallogr. Cryst. Chem.* **1969**, *25*, 1647, doi:doi.org/10.1107/S0567740869004468.

[23] P. Strobel, R. Niklaus, P. J. Schmidt and W. Schnick; Oxoberyllates $SrBeO_2$ and $Sr_{12}Be_{17}O_{29}$ as Novel Host Materials for Eu^{2+} Luminescence, *Chem. - Eur. J.* **2018**, *24*, 12678, doi:10.1002/chem.201801951.

[24] D. Schuldt and R. Hoppe; Über Synthese und Aufbau von $Na_2[BeO_2]$: $Na_8[OBeO_2BeO_2BeO_2BeO]$, *Z. Anorg. Allg. Chem.* **2004**, *578*, 119, doi:10.1002/zaac.19895780114.

[25] R. Hoppe and D. Schuldt; Neue Beryllate der Alkalimetalle: $Na_6Be_8O_{11}$, *Z. Anorg. Allg. Chem.* **2004**, *564*, 61, doi:10.1002/zaac.19885640108.

[26] L. Pauling; The Principles Determining the Structure of Complex Ionic Crystals, *J. Am. Chem. Soc.* **1929**, *51*, 1010, doi:10.1021/ja01379a006.

[27] R. D. Shannon; Revised effective ionic radii and systematic studies of interatomic distances in halides and chalcogenides, *Acta Crystallogr., Sect. A* **1976**, *32*, 751, doi:10.1107/s0567739476001551.

[28] J. C. Bachman, S. Muy, A. Grimaud, H. H. Chang, N. Pour, S. F. Lux, . . . Y. Shao-Horn; Inorganic Solid-State Electrolytes for Lithium Batteries: Mechanisms and Properties Governing Ion Conduction, *Chem. Rev.* **2016**, *116*, 140, doi:10.1021/acs.chemrev.5b00563.

[29] T. Krauskopf, C. Pompe, M. A. Kraft and W. G. Zeier; Influence of Lattice Dynamics on Na^+ Transport in the Solid Electrolyte $Na_3PS_{4-x}Se_x$, *Chem. Mater.* **2017**, *29*, 8859, doi:10.1021/acs.chemmater.7b03474.

[30] K. Wakamura; Roles of phonon amplitude and low-energy optical phonons on superionic conduction, *Phys. Rev. B* **1997**, *56*, 11593, doi:10.1103/PhysRevB.56.11593.

A Supporting Information for Chapter 2

A.1 Methods

Safety Assessment.

As Be and Be containing compounds, like BeO are characterized as toxic and might be carcinogenic,[1-2] all operations with Be were performed in closed systems to prevent any exposure. For precaution, this also applies to the product. Although, multinary beryllates in general, as beryll and other minerals are not known to be harmful.

Synthesis.

$Ba[BeSiON_2]:Eu^{2+}$ was synthesized by mixing stoichiometric amounts of BaH_2 (Materion, 99.7%), BeO (Alfa Aesar, 99.95%) and Si_3N_4 (UBE, SNA-00), and EuF_3 (Sigma-Aldrich, 99.99%) in an agate mortar with 1 wt.% of BaF_2 (abcr, 99.999%) as mineralizing agent. Due to the moisture sensitivity and toxicity of the starting materials, all manipulations were carried out in a glovebox (Unilab, MBraun, Garching; O_2 <0.1 ppm, H_2O <1 ppm) under argon atmosphere. The mixture was transferred into a tungsten crucible and heated to 1375 °C within 45 minutes in an rf-furnace under nitrogen atmosphere with a five hour dwell at target temperature and subsequent cooling to 1100 °C over three hours.

Single Crystal X-Ray Diffraction.

Selected crystals of $Ba[BeSiON_2]:Eu^{2+}$ were isolated on MicroMounts (MiTeGen). Single-crystal X-ray diffraction data were collected on a Bruker D8 Quest (Mo-K_α radiation, graphite monochromator). Integration and multi-scan absorption correction were carried out using APEX3.[3] The crystal structure was solved with the SHELXS package (direct methods) and refined against F^2 by a full-matrix least-squares method with SHELXL.[4-5] The contained Eu^{2+} was neglected in refinement due to its low overall content and therefore, insignificant scattering effects.

Crystallographic Data.

Details concerning the crystal structure data and investigations are given at the Fachinformationszentrum Karlsruhe, 76344 Eggenstein-Leopoldshafen, Germany (Fax: +49-7247-808-666; E-Mail: crysdata@fiz-karlsruhe.de) under the depository number CSD-2191356.

Powder X-Ray Diffraction.

The Rietveld method (TOPAS Academic 6) was applied on powder X-ray diffraction data, that were collected on a STOE STADI P diffractometer (Mo-Kα radiation, Ge(111) monochromator, Mythen 1k detector) in a sealed glass capillary (Hilgenberg, d = 0.3 mm) on a rotary-head in modified Debye-Scherrer geometry.

Electron Microscopy.

The chemical composition was determined based on EDS data, collected of multiple crystallites on a SM-6500F scanning electron microscope (SEM, Jeol) with a Si/Li EDS detector (Oxford Instruments, model 7418) at 30 kV (Table S5). The given electron microscope was also used for crystal imaging (Figure S3).

NMR Spectroscopy.

Beryllium was detected based on NMR data, collected on a Bruker Avance-III 500 spectrometer via magic angle spinning at 8 kHz.

UV-vis Spectroscopy.

Diffuse reflectance UV−vis spectra of undoped and doped samples ranging from 240 to 800 nm were recorded on a UV/vis spectrophotometer (Jasco V-650) with a deuterium and a halogen lamp (JASCO, Pfungstadt, Germany, Czerny−Turner monochromator with 1200 lines/mm, concave grating, photomultiplier tube detector). The step size was 1 nm.

Luminescence.

Single-particle photoluminescence measurements were carried out on an Olympus BX51 microscope with a HORIBA Fluoromax4 spectrofluorimeter system attached. The excitation wavelength was 420 nm with a spectral width of 10 nm. Emission was measured from 480 to 820 nm with 1 nm step size. Particle images were taken on a ZEISS AXIO imager M1m microscope.

Powder sample photoluminescence measurements were carried out on an in-house-built system, based on a 5.3 ″ integrating sphere and an attached spectrofluorimeter. The spectrofluorimeter is equipped with a 150 W Xe lamp with a spectral range of 230−820 nm and two Czerny-Turner monochromators with a focal length of 500 mm and grating of 1800 g/mm, which are blazed at 250/500 nm.

For measurements of temperature-dependent quantum efficiencies between 6 and 300 K, a fiber-coupled spectroscopy system, consisting of a thermally stabilized LED light source and a fiber-optic spectrometer (HR2000+ES spectrometer, Ocean Optics) was utilized. For the duration of the measurement, the thick-bed powder layer was placed in an evacuated cooling chamber cooled by liquid He. The used He was provided by a compressor system (ARS4HW, Advanced Research System Inc., Macungie, Pennsylvania, USA). Relative quantum efficiency data was obtained by integration of emission spectra.

High temperature powder data, from 300 to 500 K, were obtained with an AvaSpec-2048 USB2 spectrometer, and scaled, relative to the 300 K values, to be comparable to low temperature data.

The internal quantum efficiency was measured in regard to a $BaSO_4$ standard and a reference phosphor (CASN; BR101A: Mitsubishi Chemicals).

A.2 Results

X-Ray Diffraction

Table S1 Crystallographic data of Rietveld refinement of $Ba[BeSiON_2]:Eu^{2+}$, (standard deviations in parentheses).

Formula	$Ba[BeSiON_2]:Eu^{2+}$
Crystal system	Orthorhombic
Space group	*Ama*2 (no. 40)
Lattice parameters (Å)	a = 5.6366(3), b = 11.6363(7), c = 4.9295(3)
Cell volume (Å^3)	323.32(3)
Z	4
Density (g · cm^{-3})	4.5662(1)
T (K)	297(2)
Diffractometer	STOE STADI P
Radiation (Å)	Mo-Kα_1 (λ = 0.71073)
Profile range (°)	5.0 ≤ θ ≤ 60.0
Data points	3886
Total number of reflections	287
Refined parameters	49
Background function	Shifted Chebyshev (14 parameters)
R values	R_P = 0.0667, R_P exp. = 0.0330,
	R_{wP} = 0.0880, $R(F^2)$ = 0.1296
	R_{Bragg} =0.0190
Goodness of fit	2.668

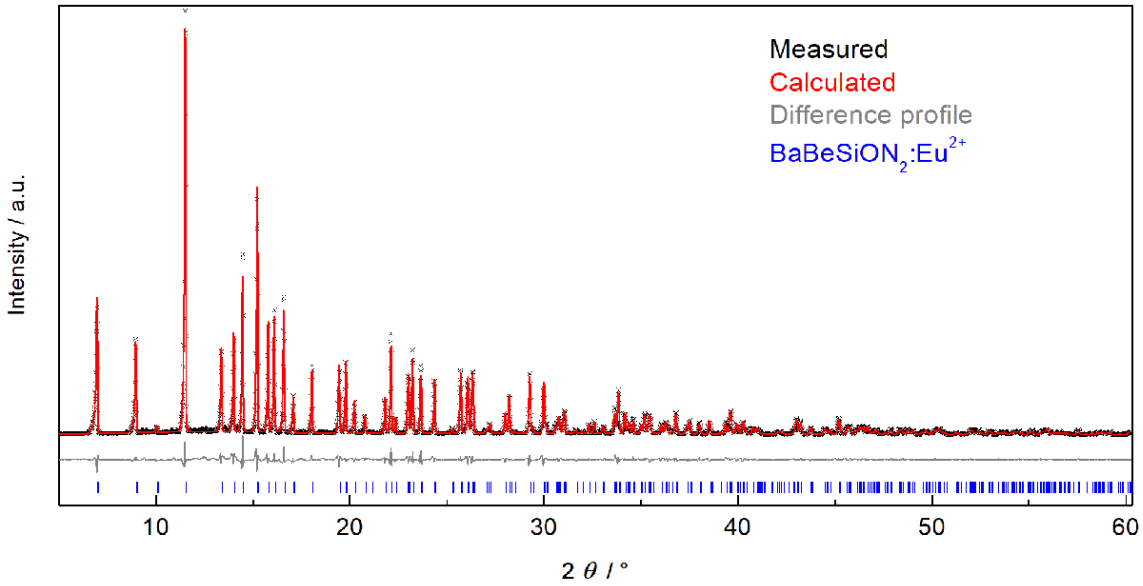

Figure S1. Crystal structure confirmation of $Ba[BeSiON_2]:Eu^{2+}$. Powder X-ray diffraction diagram of $Ba[BeSiON_2]:Eu^{2+}$ with the measured data (black crossmarks), pattern based on Rietveld refinement data (red line), difference curve (gray line) and reflection-tickmarks (blue).

Table S2. Crystallographic data of single-crystal XRD refinement of $Ba[BeSiON_2]:Eu^{2+}$, (standard deviations in parentheses).

Formula	$Ba[BeSiON_2]:Eu^{2+}$
Formula mass($g \cdot mol^{-1}$)	218.44
Crystal system	Orthorhombic
Space group	*Ama*2 (no. 40)
Lattice parameters (Å)	*a* = 5.6366(3) *b* = 11.6363(7) *c* = 4.9295(3)
Cell volume ($Å^3$)	323.32(3)
Z	4
Density ($g \cdot cm^{-3}$)	4.488
Experimental absorption coefficient [cm^{-1}]	12.416
F (000)	384
Crystal dimensions (μm^3)	25 × 15 × 5
Diffractometer	D8 Quest
Radiation	Mo-K_α (λ = 0.71073 Å)
T (K)	296(2)
Abs. correction	Multi-scan
θ range (°)	4.490 − 34.945
Measured reflns	5137
Independent reflns (I < 2 σ(I))	697 (685)
Friedel fraction coverage	0.966
R_{int}, R_σ	0.0328, 0.0221
Refined parameters	32
Restraints	1
Twin volume fraction	0.90639
R indices (I≥2σ(I))	*R*1 = 0.0124, *wR*2 = 0.0245
R indices (all data)	*R*1 = 0.0131, *wR*2 = 0.0247
GooF	1.116
$\Delta\rho_{max}$, $\Delta\rho_{min}$ / ($e \cdot Å^{-3}$)	0.556, -1.140

Table S3. Atomic coordinates and equivalent isotropic displacement parameters of $Ba[BeSiON_2]:Eu^{2+}$ (standard deviations in parentheses).

Atom (*Wyck.*)	*x*	*y*	*z*	U_{eq} (A^2)	*so f*
Ba1 (4b)	1/4	0.28252(2)	0.04265(5)	0.00847(6)	1
Si2 (4b)	1/4	0.05624(8)	0.4975(2)	0.0047(3)	1
N3 (4a)	0	0	0.6575(7)	0.0073(4)	1
N4 (4b)	1/4	0.0304(4)	0.1561(7)	0.0073(4)	1
O5 (4b)	1/4	0.1986(2)	0.543(2)	0.0096(4)	1
Be6 (4a)	0	0	0.000(1)	0.008(1)	1

Table S4. Selected bond lengths and angles in $Ba[BeSiON_2]:Eu^{2+}$, symmetry operations labeled as (i) x, y, -1+z; (ii) 1-x, 0.5-y, -0.5+z; (iii) -x, 0.5-y, -0.5+z; (iv) 0.5+x, 0.5-y, -0.5+z; (v) x, 0.5+y, -0.5+z; (vi) 0.5+x, -y, z. Standard deviations in parentheses.

Bond name	**Bond length / Å**	**Bond name**	**Bond length / Å**
Ba1—O5	2.652(10)	Si2—O5	1.672(3)
Ba1—$O5^{i}$	2.649(10)	Si2—N4	1.709(4)
Ba1—$O5^{ii}$	2.8268(2)	Si2—$N3^{vi}$	1.7426(18)
Ba1—$O5^{iii}$	2.8268(2)	Si2—N3	1.7426(18)
Ba1—$N3^{iv}$	2.9514(7)	Be6—N3	1.688(7)
Ba1—$N3^{v}$	2.9514(7)	Be6—$N4^{vi}$	1.644(4)
Ba1—N4	2.986(3)	Be6—$N4^{vii}$	1.644(4)
Angle name	**Angle / °**	**Angle name**	**Angle / °**
O5—Si2—N4	107.8(4)	$N3^{vi}$—Si2—N3	107.93(16)
O5—Si2—$N3^{vi}$	108.1(2)	N4—Be6—N4	124.2(5)
N4—Si2—$N3^{vi}$	112.32(13)	N4—Be6—N3	117.9(2)
O5—Si2—N3	108.1(2)	N4—Be6—N3	117.9(2)
N4—Si2—N3	112.32(13)		

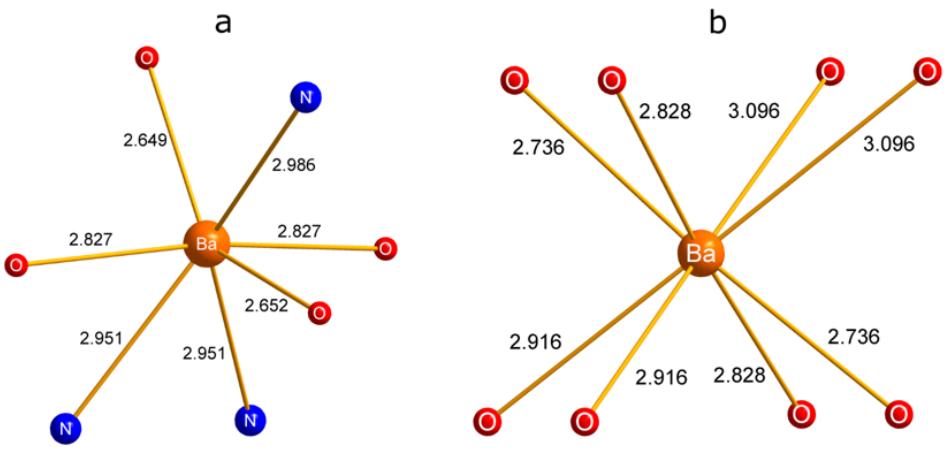

Figure S2. Comparison of coordinational environments. Barium (orange) coordinated by oxygen (red) and nitrogen (blue). **a** Sevenfold coordinated barium in $Ba[BeSiON_2]$, **b** eightfold coordinated barium in $Ba[Si_2O_2N_2]$.[6]

Scanning Electron Microscopy

Table S5. Energy dispersive X-ray spectroscopy (EDS) of $Ba[BeSiON_2]$ measured on eight sample points for elemental analysis.

	1	2	3	4	5	6	7	8	Ø
Ba	1	1	1	1	1	1	1	1	1
Si	1.0	1.0	1.0	0.9	0.9	0.6	1.0	1.0	0.9
O	1.2	1.3	1.1	0.9	0.9	0.5	1.5	1.2	1.1
N	2.1	2.5	2.0	1.6	1.7	1.0	2.6	2.1	2.0

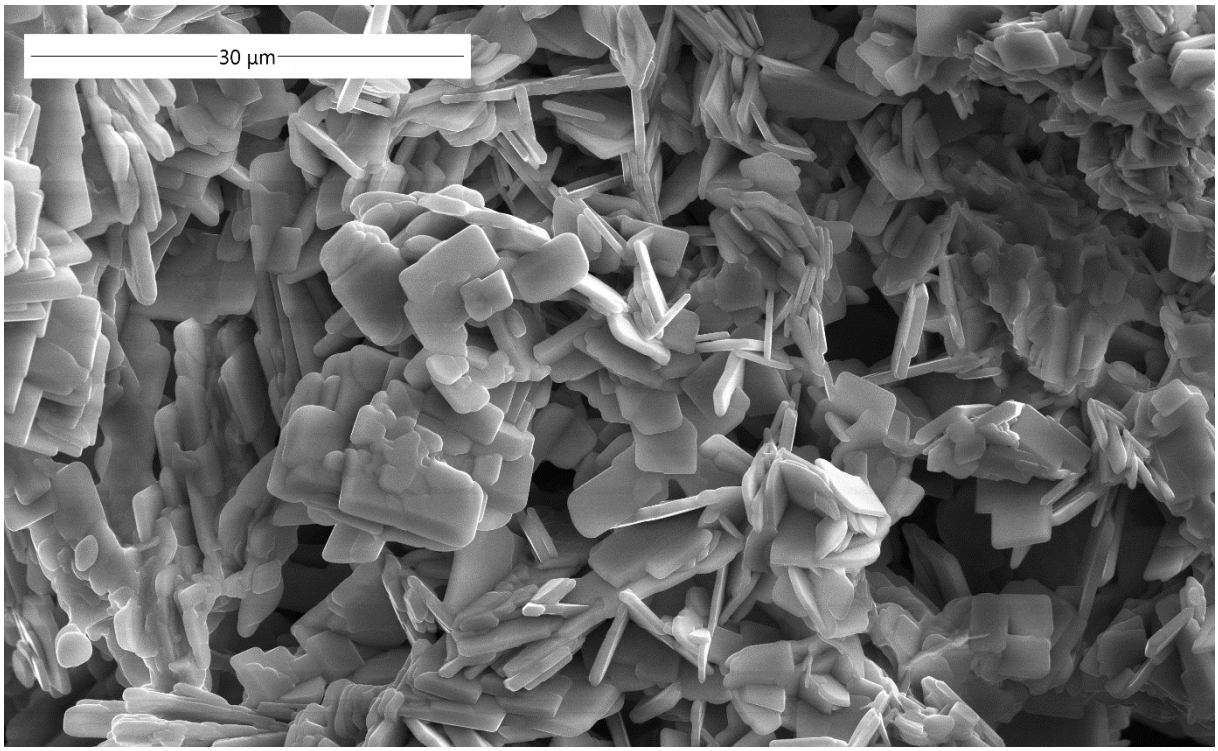

Figure S3. SEM image of agglomerated crystals of $Ba[BeSiON_2]:Eu^{2+}$. Agglomerates of crystals of $Ba[BeSiON_2]:Eu^{2+}$ are shown at an acceleration voltage of 30 kV. The respective crystallites have edge lengths in the range of several micrometers.

Nuclear Magnetic Resonance Spectroscopy

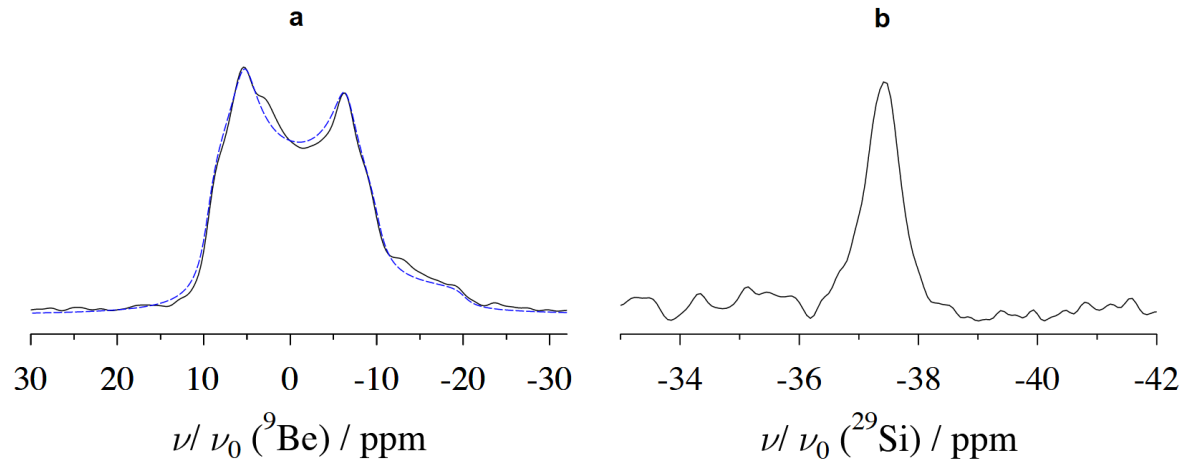

Figure S4. Solid state NMR spectra of Ba[BeSiON$_2$]:Eu^{2+} under 8 kHz magic-angle spinning (MAS). Solid-state NMR spectra of BBS **a** ^{9}Be-NMR, with the quadrupolar-broadened line shape of the central transition centered around 0 ppm (black: experimental spectrum, blue: simulated line shape); **b** ^{29}Si-NMR, with a single resonance at −37.4 ppm.

Figure S4 shows the results of the characterization of BBS by solid-state NMR. The central-transition signal in the ^{9}Be-NMR spectrum (Fig. S4a) shows the typical broadening caused by the quadrupolar interaction, as may be expected for a nuclide with spin I=3/2. The two peaks present in the spectrum belong to a single, broadened line shape, and are therefore compatible with the existence of one beryllium site in the crystal structure. Fitting the spectrum with the DMFIT program[7] returns a quadrupolar coupling constant of C_q = (1.59 ± 0.01) MHz, and an asymmetry parameter of η_q = (0.232 ± 0.001). The C_q value is among the largest observed so far for ^{9}Be, and consistent with the comparatively low symmetry of trigonal coordination. In the frequently occurring tetrahedral coordination, C_q does not exceed 0.7 MHz (see, e.g., Table 1 in Ref. [8]). The fit value for the isotropic chemical shift is δ_{iso}=(12.2 ± 0.1) ppm (with the shown spectrum being indirectly referenced by using the ^{1}H resonance of TMS). With the large quadrupolar coupling experienced by ^{9}Be in BBS, the position of the central-transition resonance in Fig. S4a is determined by both the chemical shift and the quadrupolar interaction. The latter contributes a quadrupolar-induced shift (QIS), which is customarily described by perturbation theory to second-order. Since the QIS has a negative sign, the entire line shape is moved to the right from the value of the isotropic chemical shift, and centered around 0 ppm. In contrast, ^{29}Si has spin I=1/2, and is therefore affected by chemical shift only. The ^{29}Si spectrum in Fig. S4b shows a single resonance, which is compatible with having a single silicon site in the crystal structure. The resonance position directly represents the isotropic chemical shift value, δ_{iso}=(−37.4 ± 0.1) ppm.

UV/Vis Spectroscopy

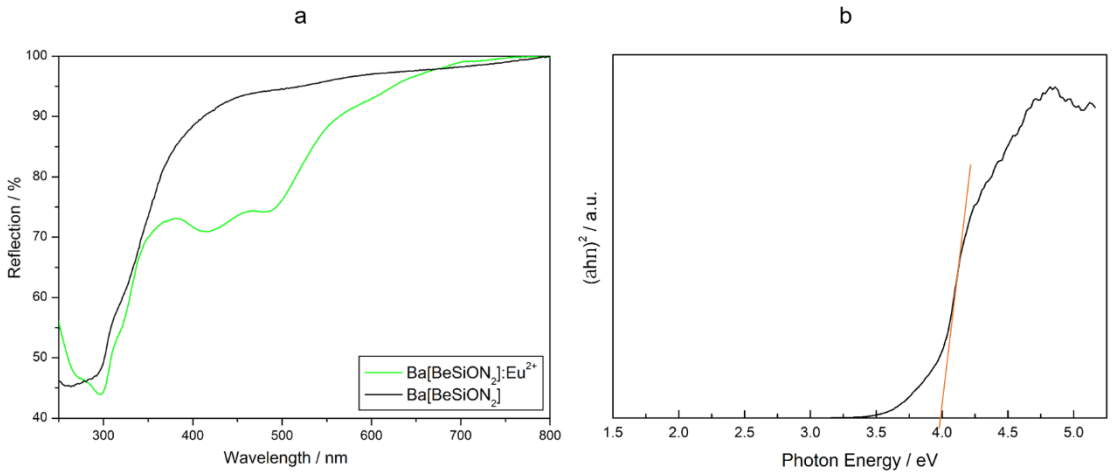

Figure S5. UV/Vis spectrum and Tauc-plot. a .UV/Vis plot of BBS. Doped sample in green, undoped sample in black; **b** Tauc plot of the Kubelka-Munk-calculated pseudo absorption (black), a linear data fit on the infliction point (orange).[9]

Luminescence

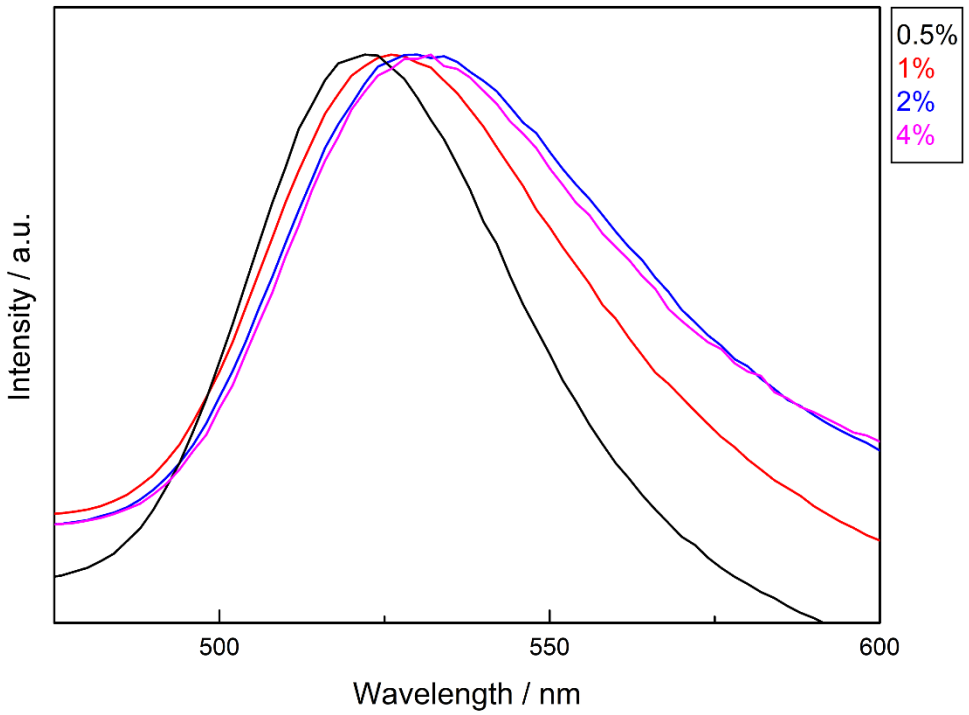

Figure S6. Dopant concentration dependent luminescence spectra. Emission spectra of BBS at given dopant concentrations.

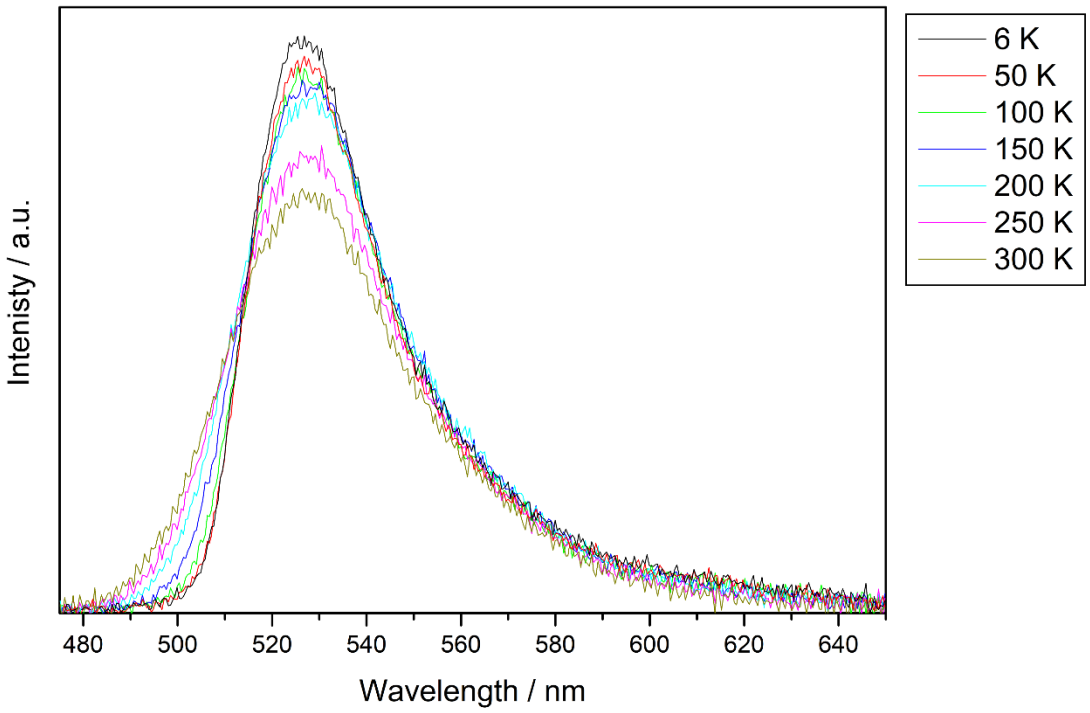

Figure S7. Temperature dependent luminescence spectra, low temperature. Emission spectra of BBS at the given temperatures.

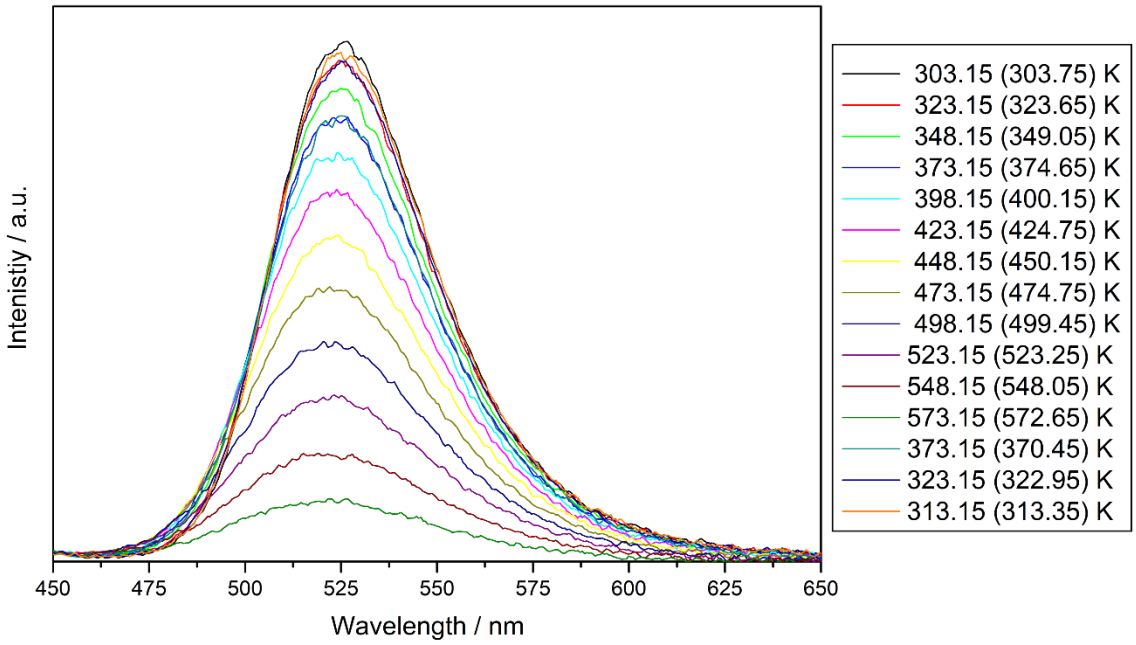

Figure S8. Temperature dependent luminescence spectra, high temperature. Emission spectra of BBS at the given temperatures; the exact temperatures are given in brackets.

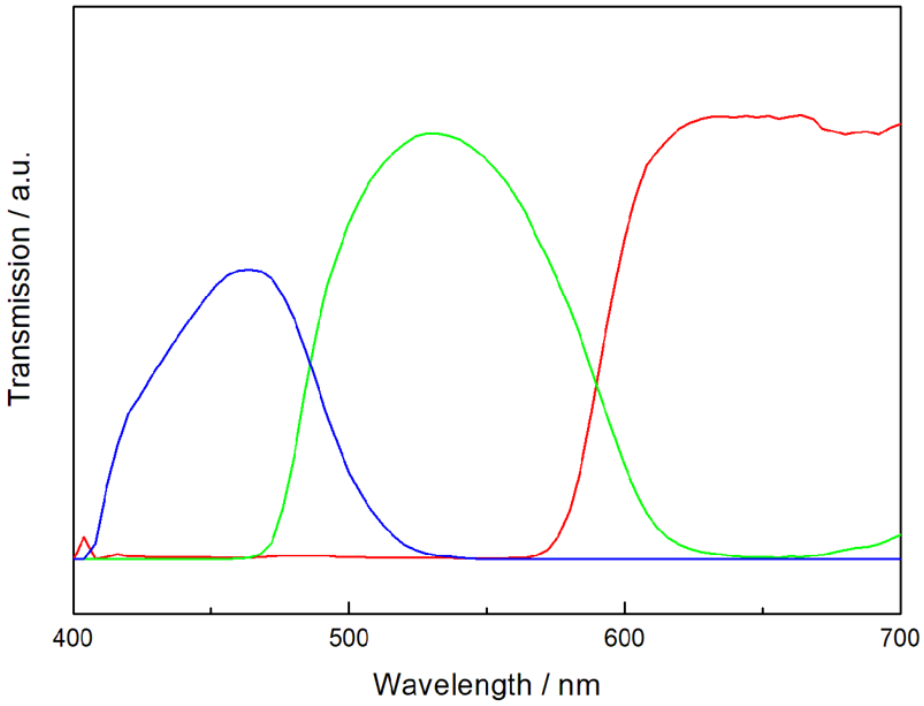

Figure S9. Filters applied for color gamut simulations. The three filter curves used for color gamut simulation, all filters are given in their respective color.

Table S6. Overview on green phosphors. Selected green phosphors, their emission maximum (λ_{em}) and full width at half maximum (*fwhm*).

	λ_{em} / nm	*fwhm* / nm	*fwhm* / cm^{-1}
$BaSiBeON_2:Eu^2$	526	45	1600
$Ba[Li_2(Al_2Si_2)N_6]:Eu^{2+}$[10]	532	57	1962
β-$SiAlON:Eu^{2+}$[11]	535	55	1560
$RbNa(Li_3SiO_4)_2:Eu^{2+}$[12]	523	41	1498
$Ba[Li(Si_7Al)N_{12}]:Eu^{2+}$[13]	515	61	2280
$Sr_2MgAl_{22}O_{36}:Mn^{2+}$[14]	518	26	969
$NaK_2Li[Li_3SiO_4]_4:Eu^{2+}$[15]	528	44	1569
$NaBaB_9O_{15}:Eu^{2+}$[16]	515	61	2294
$MgAl_2O_4:Mn^{2+}$[17]	525	35	1269
$LiK_7[Li_3SiO_4]_8:Eu^{2+}$[18]	509	42	1651
$Ba_2SiO_4:Eu^{2+}$[19]	505	52	2044
$LuAG:Ce^{3+}$	505	87	3226

A.3 References

[1] O. Kumberger and H. Schmidbaur; Warum ist Beryllium so toxisch?, *Chem. Unserer Zeit* **1993**, *27*, 310.

[2] D. Naglav, M. R. Buchner, G. Bendt, F. Kraus and S. Schulz; Off the Beaten Track-A Hitchhiker's Guide to Beryllium Chemistry, *Angew. Chem., Int. Ed.* **2016**, *55*, 10562, doi:10.1002/anie.201601809.

[3] BrukerAXS, Billerica, **2016**.

[4] G. M. Sheldrick; Crystal structure refinement with SHELXL, *Acta Crystallogr., Sect. C: Struct. Chem.* **2015**, *71*, 3, doi:10.1107/S2053229614024218.

[5] G. M. Sheldrick; A short history of SHELX, *Acta Crystallogr. Sect. A* **2008**, *64*, 112, doi:10.1107/S0108767307043930.

[6] V. Bachmann, C. Ronda, O. Oeckler, W. Schnick and A. Meijerink; Color Point Tuning for (Sr,Ca,Ba)$Si_2O_2N_2$:Eu^{2+} for White Light LEDs, *Chem. Mater.* **2009**, *21*, 316, doi:10.1021/cm802394w.

[7] D. Massiot, F. Fayon, M. Capron, I. King, S. Le Calvé, B. Alonso, . . . G. Hoatson; Modelling one- and two-dimensional solid-state NMR spectra, *Magn. Reson. Chem.* **2002**, *40*, 70, doi:10.1002/mrc.984.

[8] H. Eckert; Solid-state Be-9 NMR of beryllium compounds, *Z. Naturforsch., B* **2020**, *75*, 441, doi:10.1515/znb-2020-0026.

[9] P. Makula, M. Pacia and W. Macyk; How To Correctly Determine the Band Gap Energy of Modified Semiconductor Photocatalysts Based on UV-Vis Spectra, *J. Phys. Chem. Lett.* **2018**, *9*, 6814, doi:10.1021/acs.jpclett.8b02892.

[10] P. Strobel, S. Schmiechen, M. Siegert, A. Tücks, P. J. Schmidt and W. Schnick; Narrow-Band Green Emitting Nitridolithoalumosilicate Ba[Li_2(Al_2Si_2)N_6]:Eu^{2+} with Framework Topology *whj* for LED/LCD-Backlighting Applications, *Chem. Mater.* **2015**, *27*, 6109, doi:10.1021/acs.chemmater.5b02702.

[11] N. Hirosaki, R.-J. Xie, K. Kimoto, T. Sekiguchi, Y. Yamamoto, T. Suehiro and M. Mitomo; Characterization and properties of green-emitting β-SiAlON:Eu2+ powder phosphors for white light-emitting diodes, *Appl. Phys. Lett.* **2005**, *86*, 211905, doi:10.1063/1.1935027.

[12] H. Liao, M. Zhao, Y. Zhou, M. S. Molokeev, Q. Liu, Q. Zhang and Z. Xia; Polyhedron Transformation toward Stable Narrow-Band Green Phosphors for Wide-Color-Gamut Liquid Crystal Display, *Adv. Funct. Mater.* **2019**, *29*, 1901988, doi:10.1002/adfm.201901988.

[13] T. Takeda, N. Hirosaki, S. Funahshi and R.-J. Xie; Narrow-Band Green-Emitting Phosphor $Ba_2LiSi_7AlN_{12}:Eu^{2+}$ with High Thermal Stability Discovered by a Single Particle Diagnosis Approach, *Chem. Mater.* **2015**, *27*, 5892, doi:10.1021/acs.chemmater.5b01464.

[14] Y. Zhu, Y. Liang, S. Liu, H. Li and J. Chen; Narrow-Band Green-Emitting $Sr_2MgAl_{22}O_{36}:Mn^{2+}$ Phosphors with Superior thermal Stability and Wide Color Gamut for Backlighting Display Applications, *Adv. Opt. Mater.* **2019**, *7*, 1801419, doi:10.1002/adom.201801419.

[15] M.-H. Fang, C. O. M. Mariano, K.-C. Chen, J.-C. Lin, Z. Bao, S. Mahlik, . . . J. P. Attfield; High-Performance $NaK_2Li[Li_3SiO_4]_4:Eu$ Green Phosphor for Backlighting Light-Emitting Diodes, *Chem. Mater.* **2021**, *33*, 1893, doi:10.1021/acs.chemmater.1c00180.

[16] Y. Zhuo, S. Hariyani, J. Zhong and J. Brgoch; Creating a Green-Emitting Phosphor through Selective Rare-Earth Site Preference in $NaBaB_9O_{15}:Eu^{2+}$, *Chem. Mater.* **2021**, *33*, 3304, doi:10.1021/acs.chemmater.1c00447.

[17] E. H. Song, Y. Y. Zhou, Y. Wei, X. X. Han, Z. R. Tao, R. L. Qiu, . . . Q. Y. Zhang; A thermally stable narrow-band green-emitting phosphor $MgAl_2O_4:Mn^{2+}$ for wide color gamut backlight display application, *J. Mater. Chem. C* **2019**, *7*, 8192, doi:10.1039/c9tc02107h.

[18] D. S. Wimmer, M. Seibald, D. Baumann, S. Peschke, K. Wurst, G. Heymann, . . . H. Huppertz; Novel Narrow Band Cyan-Green Phosphor $LiK_7[Li_3SiO_4]_8:Eu^{2+}$ with Enhanced Suppression of Second Broad Band Emission, *Eur. J. Inorg. Chem.* **2021**, *2021*, 4470, doi:10.1002/ejic.202100550.

[19] M. Zhang, J. Wang, Q. Zhang, W. Ding and Q. Su; Optical properties of $Ba_2SiO_4:Eu^{2+}$ phosphor for green light-emitting diode (LED), *Mater. Res. Bull.* **2007**, *42*, 33, doi:10.1016/j.materresbull.2006.05.011.

B Supporting Information for Chapter 3

B.1 Elemental Analysis

Table S1. Energy dispersive X-ray spectroscopy (EDS) as elemental analysis of $SrBe_{0.87}Si_{2.13}O_{2.74}N_{2.26}:Eu^{2+}$

$SrBe_{0.87}Si_{2.13}O_{2.74}N_{2.26}:Eu^{2+}$	1	2	3	4	5	6	7	Ø	Σ
Sr	1	1	1	1	1	1	1	1	
Si	3.7	3.0	2.8	2.3	2.5	2.5	2.5	2.8	0.23
O	4.0	3.3	3.4	3.3	2.9	3.2	3.0	3.3	0.12
N	2.9	2.4	1.8	1.2	2.6	2.6	2.5	2.3	0.33

B.2 X-Ray Diffraction

For additional information and further details of the crystal structure investigations the crystal information file (.cif) can be obtained from the Fachinformationszentrum Karlsruhe, 76344 Eggenstein-Leopoldshafen, Germany (Fax, (+49)7247-808-666; email, crysdata@fiz-karlsruhe.de) upon quoting the depository number CSD-2291214.

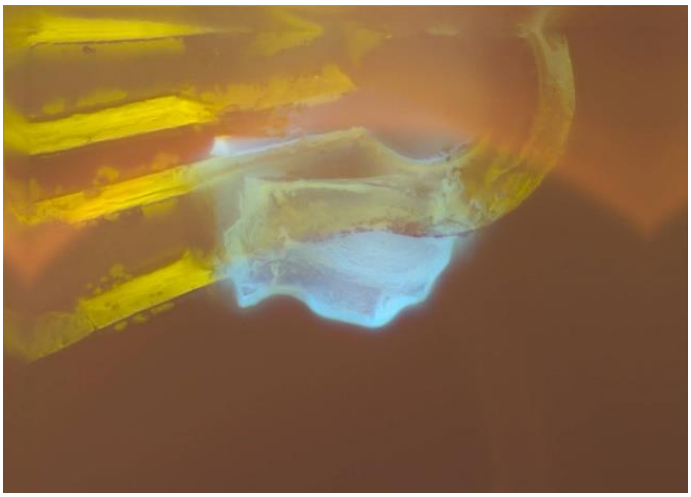

Figure S1 Image of a single crystal of $SrBe_{0.87}Si_{2.13}O_{2.74}N_{2.26}:Eu^{2+}$ on a micromount under UV-irradiation.

Table S2. SCXRD Crystallographic data

	$SrBe_{0.87}Si_{2.13}O_{2.74}N_{2.26}:Eu^{2+}$
Formula mass [g mol^{-1}]	230.79
Crystal system, space group	Orthorhombic, $P2_12_12_1$ (no. 19)
Lattice parameters [Å]	a = 4.7671(2)
	b = 7.7683(2)
	c = 10.9364(3)
Cell volume [Å^3]	405.00(2)
Formula units per cell Z	4
X-ray density [g cm^{-1}]	3.785
Linear absorption coefficient [cm^{-1}]	13.824
F(000)	436.2
Crystal dimensions (ca.) [mm^3]	0.025 × 0.025 × 0.02
Diffractometer	Bruker D8 Venture
Radiation	Mo-K_α (λ = 0.71073 Å)
Temperature [K]	297(2)
Abs correction	Multi-scan
θ range [°]	3.217 – 37.498
Measured reflections	19177
Independent reflections (I < 2 σ(I))	2131 (1964)
R_{int}/ R_σ	0.0517/0.0304
Min./max. transmission	0.858/1.000
Refined parameters	86
Restraints	1 (net charge neutrality)
Constraints	6
GooF	1.067
Flack parameter	0.547(8)
R indices ($F_o^2 \geq 2\sigma(F_o^2)$)	R1 = 0.0252, wR2 = 0.0314
R indices (all data)	R1 = 0.0452, wR2 = 0.0463
min./max. residual electron density [eÅ^{-3}]	-0.685/0.763

Table S3. Atomic coordinates and equivalent isotropic displacement parameters of $SrBe_{0.87}Si_{2.13}O_{2.74}N_{2.26}:Eu^{2+}$

Atom (*Wyck.*)	*x*	*y*	*z*	U_{eq} (A^2)	*sof*
Sr01 (4a)	0.51980(6)	0.44150(3)	0.16845(2)	0.01066(6)	1
Si02 (4a)	0.0056(2)	0.30042(8)	0.41768(6)	0.00628(12)	1
Si03 (4a)	0.51580(19)	0.03326(9)	0.04300(6)	0.00706(13)	1
Be04 (4a)	0.0075(6)	0.1646(3)	0.1569(2)	0.0076(6)	0.870(5)
Si04 (4a)	“	“	“	“	0.130(5)
O005 (4a)	0.0325(6)	0.3392(3)	0.07370(19)	0.0120(4)	1
O006 (4a)	0.6738(4)	0.1177(3)	0.1617(2)	0.0085(4)	0.87(2)
N006 (4a)	“	“	“	“	0.13(2)
O007 (4a)	0.1288(5)	0.2164(3)	0.2918(2)	0.0097(4)	0.87(2)
N007 (4a)	“	“	“	“	0.13(2)
N008 (4a)	0.1976(5)	0.6500(3)	0.0051(2)	0.0071(4)	1
N009 (4a)	0.3150(5)	0.0134(3)	0.5931(2)	0.0082(4)	1

Table S4. Selected bond lengths and angles in $SrBe_{0.87}Si_{2.13}O_{2.74}N_{2.26}:Eu^{2+}$ with symmetry operations (i) 1−*x*, 0.5+*y*, 0.5−*z*; (ii) 1+*x*, *y*, *z*; (iii) 0.5+*x*, 0.5−*y*, 1−*z*; (iv) −0.5+*x*, 0.5−*y*, 1−*z*; (v) −*x*, −0.5+*y*, 0.5−*z*; (vi) 0.5−*x*, 1−*y*, 0.5+*z*; (vii) 0.5+*x*, 0.5−*y*, −*z*; (viii) 0.5−*x*, −*y*, −0.5+*z*; (ix) −1+*x*, *y*, *z*; (x) 1−*x*, −0.5+*y*, 0.5−*z*; (xi) −0.5+*x*, 0.5−*y*, −*z*; (xii) −*x*, 0.5+*y*, 0.5−*z*; (xiii) 0.5−*x*, 1−*y*, −0.5+*z*; (xiv) 0.5−*x*, −*y*, 0.5+*z*.

Bond name	Bond length / Å	Bond name	Bond length / Å
Sr01—O006|N006^{i}	2.485(2)	Si02—N009^{iv}	1.712(2)
Sr01—O006|N006	2.621(2)	Si02—N008^{v}	1.737(3)
Sr01—O005	2.665(3)	Si02—N008^{vi}	1.750(3)
Sr01—O007|N007^{i}	2.749(2)	Si03—O005^{vii}	1.617(2)
Sr01—O005^{ii}	2.771(3)	Si03—O006|N006	1.638(2)
Sr01—N008	2.859(2)	Si03—N009^{viii}	1.709(3)
Sr01—O007|N007	2.890(2)	Si03—N008^{vii}	1.748(2)
Sr01—N009^{iii}	2.984(3)	Be04|Si04—O006|N006^{ix}	1.633(4)

Angle name	Angle / °	Angle name	Angle / °
O007|N007—Si02—N009^{iv}	118.05(12)	O006|N006—Si03—N009^{viii}	104.79(12)
O007|N007—Si02—N009^{iv}	118.05(12)	N009^{viii}—Si03—N008^{vii}	112.41(12)
O007|N007—Si02—N008^{v}	109.99(12)	O006|N006^{ix}—Be04|Si04—O007|N007	111.73(18)
N009^{iv}—Si02—N008^{v}	107.79(13)	O006|N006^{ix}—Be04|Si04—O005	105.9(2)
O007|N007—Si02—N008^{vi}	104.95(13)	O007|N007—Be04|Si04—O005	105.75(17)
N009^{iv}—Si02—N008^{vi}	106.31(12)	O006|N006^{ix}—Be04|Si04—N009^{viii}	107.76(16)
O005^{vii}—Si03—N008^{vii}	103.71(12)	O007|N007—Be04|Si04—N009^{viii}	112.35(19)
O005^{vii}—Si03—O006|N006	110.96(12)	O005—Be04|Si04—N009^{viii}	113.23(18)

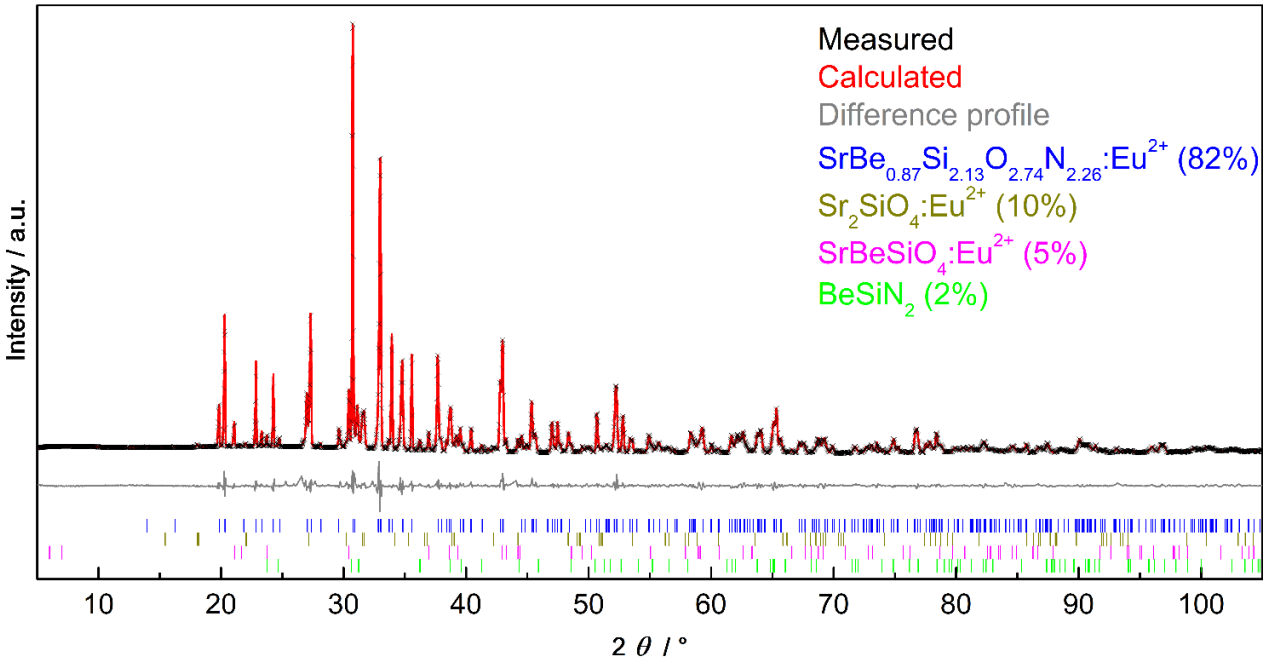

Figure S27 Rietveld refinement and crystal structure confirmation of $SrBe_{0.87}Si_{2.13}O_{2.74}N_{2.26}:Eu^{2+}$. Powder X-ray diffraction diagram of $SrBe_{0.87}Si_{2.13}O_{2.74}N_{2.26}:Eu^{2+}$ with the collected data (black crossmarks), calculated pattern based on Rietveld refinement data (red line), difference curve (grey line) and reflex-tick marks (blue, dark yellow, magenta and green).

Table S5. PXRD Crystallographic data

	$SrBe_{0.87}Si_{2.13}O_{2.74}N_{2.26}$
Formula mass [g mol^{-1}]	230.79
Crystal system, space group	Orthorhombic, $P2_12_12_1$ (no. 19)
Lattice parameters [Å]	a = 4.7652(3)
	b = 7.7783(2)
	c = 10.9032(4)
Cell volume [Å^3]	404.13(3)
Formula units per cell Z	4
X-ray density [g cm^{-1}]	3.7930(3)
Linear absorption coefficient [cm^{-1}]	237.00(2)
Radiation	Cu-$K_{\alpha1}$ (λ = 1.5406 Å)
Temperature	293(2)
2θ range [°]	5.000 − 105.485
Number of data points	6700
Number of parameters	96, thereof 12 background
GooF	3.7885
R_{wp}	0.0715
R_{exp}	0.0189
R_P	0.0507
R_{Bragg}	0.0205

B.3 Chardi and BVS

Table S6. Results of CHARDI and BVS calculations

Site	Expected Charge	CHARDI	BVS
Sr01	2	1.99	1.81
Si02	4	4.08	3.95
Si03	4	3.93	4.00
Be/Si04	2.26	2.26	2.05/3.89
O005	−2	−2.02	−1.98
O/N006	−2.13	−2.11	−2.16/−2.89
O/N007	−2.13	−2.15	−1.85/−2.46
N008	−3	−3.00	−3.02
N009	−3	−2.98	−2.87

C Supporting Information for Chapter 4

C.1 Crystallographic Data.

Details concerning the crystal structure data and investigations are given at the Fachinformationszentrum Karlsruhe, 76344 Eggenstein-Leopoldshafen, Germany (Fax: +49-7247-808-666; E-Mail: crysdata@fiz-karlsruhe.de) under the depository numbers CSD-2305743 (Ba) and CSD-2305744 (Ca).

C.2 X-Ray Diffraction

Table S1 Crystallographic data of Rietveld refinement of $Ca[BeSi_2N_4]$ with standard deviations in parentheses.

Formula	$Ca[BeSi_2N_4]$
Crystal system	Hexagonal
Space group	$P\bar{6}$ (no. 174)
Lattice parameters/ Å	$a = b$ =8.36867(2), c = 9.17822(3)
Cell volume/ $Å^3$	556.677(3)
Z	6
Density/ ($g \cdot cm^{-3}$)	2.887
T/ K	297(2)
Diffractometer	STOE STADI P
Radiation/ Å	Cu-Kα_1 (λ = 1.540596)
Data points	6572
Total number of reflections	237
Refined parameters	35
Background function	Shifted Chebyshev (12 parameters)
R values	R_P = 0.03529, R_P exp. = 0.02574,
	R_{WP} = 0.04800
	R_{Bragg} =0.0181
Goodness of fit	1.865

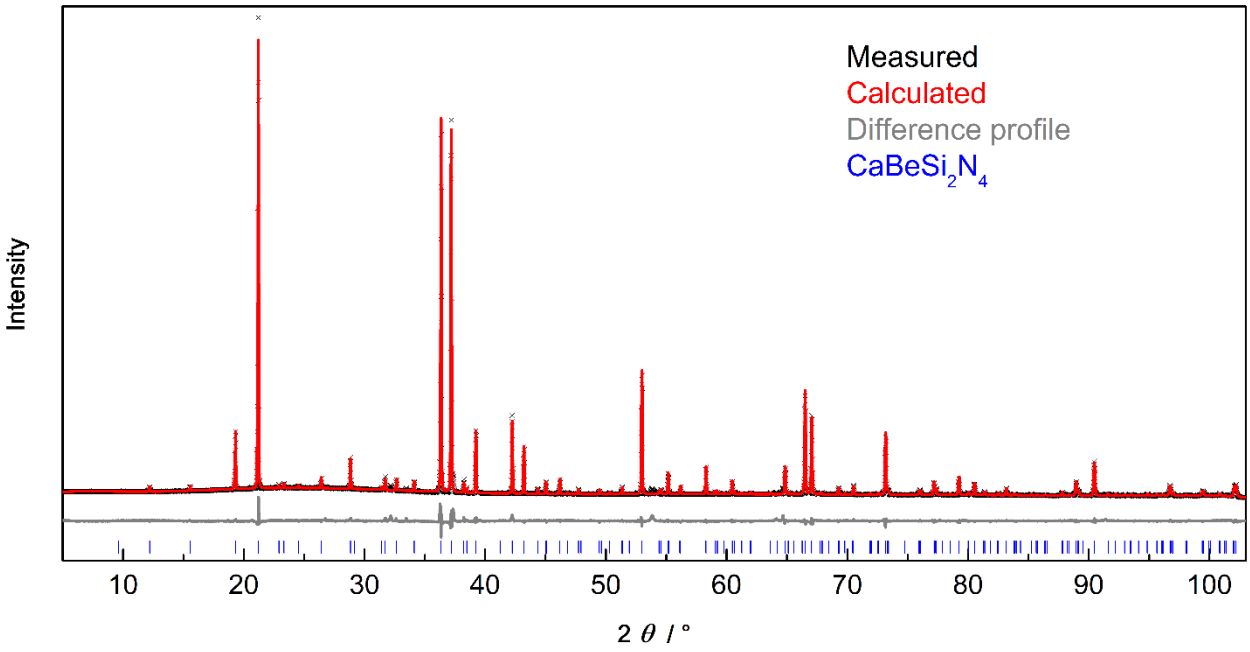

Figure S8. Crystal structure confirmation of Ca[$BeSi_2N_4$]. Powder X-ray diffraction diagram of Ca[$BeSi_2N_4$] with the measured data (black crossmarks), pattern based on Rietveld refinement data (red line), difference curve (gray line) and reflection-tickmarks of Ca[$BeSi_2N_4$] (blue) as well as Be_3N_2 (dark yellow).

Table S2. Crystallographic data of single-crystal XRD refinement of $Ca[BeSi_2N_4]$ with standard deviations in parentheses.

Formula	$Ca[BeSi_2N_4]^+$
Crystal system	Hexagonal
Space group	$P\bar{6}$ (no. 174)
Lattice parameters / Å	$a = b$ =8.369(1), c = 9.190(1)
Cell volume / Å^3	557.43(15)
Z	6
Density / g · cm^{-3}	2.833
Experimental absorption coefficient / cm^{-1}	0.226
F (000)	480
Crystal dimensions / µm^3	3 × 2 × 1
Diffractometer	ESRF Beamline ID11
Radiation	Synchrotron (λ = 0.30996 Å)
T / K	293(2)
Abs. correction	Empirical
θ range / °	1.56 − 18.6
Measured reflns	5416
Independent reflns (I < 2 σ(I))	1198 (1171)
Friedel fraction coverage	0.990
R_{int}, R_σ	0.0523, 0.0491
Refined parameters	81
Flack	-0.16(17)
R indices (I≥2σ(I))	R1 = 0.0275, wR2 = 0.0621
R indices (all data)	R1 = 0.0279, wR2 = 0.0623
GooF	1.126
$\Delta\rho_{max}$, $\Delta\rho_{min}$ / e·Å^{-3}	0.468, -0.961

Table S3. Atomic coordinates and equivalent isotropic displacement parameters of $Ca[BeSi_2N_4]$ with standard deviations in parentheses.

Atom (*Wyck.*)	*x*	*y*	*z*	U_{eq} (A^2)	*sof*
Ca1 (3*k*)	0.6805(3)	0.6561(4)	1/2	0.0121(3)	1
Ca2 (3*j*)	0.9877(3)	0.6756(5)	0	0.0108(3)	1
Si1 (6*l*)	0.9975(2)	0.6559(3)	0.68004(12)	0.0055(2)	1
Si2 (6*l*)	0.6723(2)	0.6787(3)	0.82097(13)	0.0059(2)	1
Be1 (2*h*)	1/3	2/3	0.7741(7)	0.0078(13)	1
Be2 (2*i*)	2/3	1/3	0.7638(11)	0.010(2)	1
Be3 (2*a*)	1	1	0.7198(10)	0.009(2)	1
N1 (6*l*)	0.7810(3)	0.5605(3)	0.7626(4)	0.0108(5)	1
N2 (6*l*)	0.7722(3)	0.8812(3)	0.7164(3)	0.0107(4)	1
N3 (6*l*)	0.4507(3)	0.8924(3)	0.7736(4)	0.0121(6)	1
N4 (3*k*)	0.9680(11)	0.6087(9)	1/2	0.0130(14)	1
N5 (3*j*)	0.712(1)	0.7338(10)	0	0.0144(13)	1

Table S4. Selected bond lengths and angles in $Ca[BeSi_2N_4]$ symmetry operations labeled as (i) 1−*y*, *x*−*y*, *z*; (ii) *x*, *y*, 1−*z*; (iii) −*x*+*y*, 1−*x*, 1−*z*; (iv) −*x*+*y*, 1−*x*, *z*; (v) 2−*y*, 1+*x*−*y*, *z*; (vi) *x*, *y*, 2−*z*; (vii) 2−*y*, 1+*x*−*y*, 2−*z*; (viii) 1−*y*, 1+*x*−*y*, *z*; (ix) 1−*x*+*y*, 1−*x*, *z*; (x) 1−*x*+*y*, 2−*x*, *z*.. Standard deviations in parentheses.

Bond name	Bond length / Å	Bond name	Bond length / Å
Ca1—N4^{i}	2.453(7)	Si1—N4	1.6903(19)
Ca1—N2	2.578(3)	Si1—N3^{v}	1.734(3)
Ca1—N2^{ii}	2.578(3)	Si1—N2^{v}	1.737(3)
Ca1—N4	2.627(8)	Si1—N1	1.746(3)
Ca1—N1^{ii}	2.801(3)	Si2—N5	1.696(2)
Ca1—N1	2.801(3)	Si2—N1	1.730(3)
Ca1—N3^{iii}	3.054(4)	Si2—N3^{iv}	1.731(3)
Ca1—N3^{iv}	3.054(4)	Si2—N2	1.755(3)
Ca2—N5^{v}	2.438(8)	Be1—N3^{iv}	1.637(2)
Ca2—N5	2.585(7)	Be1—N3	1.637(2)
Ca2—N1	2.648(4)	Be1—N3^{viii}	1.637(2)
Ca2—N1^{vi}	2.648(4)	Be2—N1	1.646(2)
Ca2—N3^{vii}	2.699(3)	Be2—N1^{ix}	1.646(2)
Ca2—N3^{v}	2.699(3)	Be2—N1^{i}	1.646(2)
Ca2—N2^{vii}	3.044(4)	Be3—N2^{v}	1.652(2)
Ca2—N2^{v}	3.044(4)	Be3—N2	1.652(2)
		Be3—N2^{x}	1.652(2)
Angle name	**Angle / °**	**Angle name**	**Angle / °**
N4—Si1—N3^{v}	115.2(2)	N1—Si2—N3^{iv}	107.73(15)
N4—Si1—N2^{v}	112.8(2)	N5—Si2—N2	109.6(3)
N3^{v}—Si1—N2^{v}	106.94(14)	N1—Si2—N2	104.46(13)
N4—Si1—N1	108.7(3)	N3^{iv}—Si2—N2	108.07(14)
N3^{v}—Si1—N1	104.08(13)	N2^{v}—Be3—N2	119.96(2)
N2^{v}—Si1—N1	108.62(13)	N2^{v}—Be3—N2^{x}	119.97(2)
N5—Si2—N1	111.7(3)	Si1^{ii}—N4—Si1	156.4(5)
N5—Si2—N3^{iv}	114.8(3)	Si2—N5—Si2^{vi}	151.9(5)

Table S5 Crystallographic data of Rietveld refinement of $Ba[BeSi_2N_4]$ with standard deviations in parentheses.

Formula	$Ba[BeSi_2N_4]^+$
Crystal system	Orthorhombic
Space group	*Ama*2 (no. 40)
Lattice parameters / Å	a = 8.1377(1), b =9.9995 (2), c = 4.80545(7)
Cell volume / Å^3	391.04(1)
Z	4
Density / g · cm^{-3}	4.391
T / K	297(2)
Diffractometer	STOE STADI P
Radiation / Å	Ag-Kα (λ = 0.5593268)
Data points	4257
Total number of reflections	870
Refined parameters	50
Background function	Shifted Chebyshev (10 parameters)
R values	R_P = 0.05735, R_P exp. = 0.02729,
	R_{wP} = 0.07452
	R_{Bragg} =0.0261
Goodness of fit	2.731

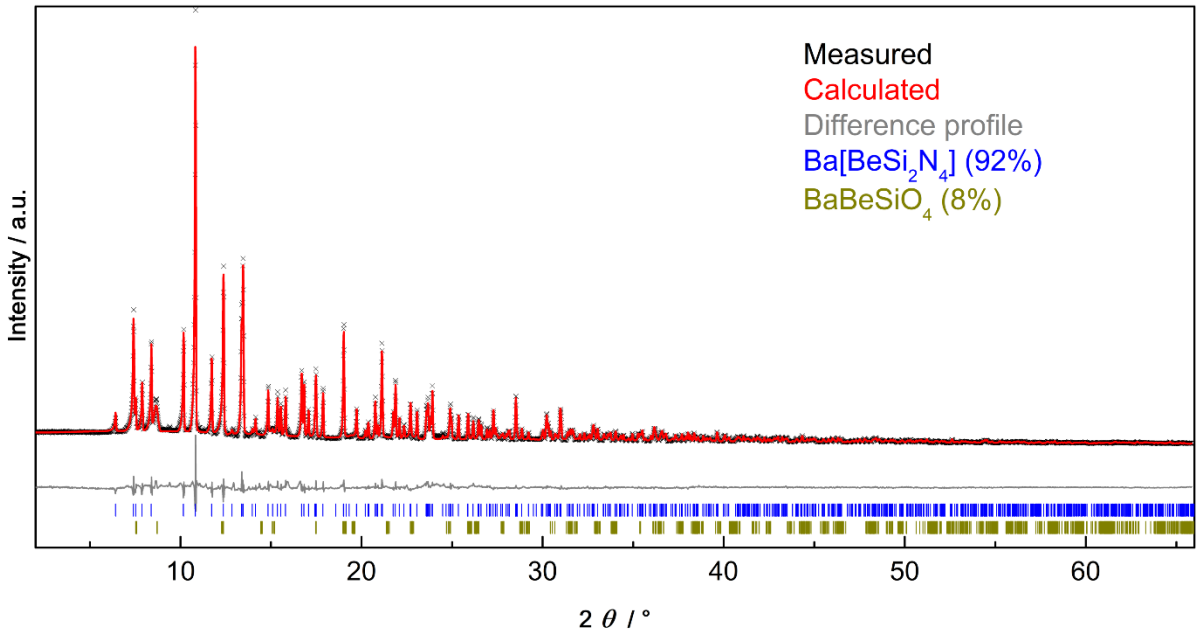

Figure S2. Crystal structure confirmation of $Ba[BeSi_2N_4]$. Powder X-ray diffraction diagram of $Ba[BeSi_2N_4]$ with the measured data (black crossmarks), pattern based on Rietveld refinement data (red line), difference curve (gray line) and reflection-tickmarks of $Ba[BeSi_2N_4]$ (blue) as well as $BaBeSiO_4$ (dark yellow).

Table S6. Crystallographic data of single-crystal XRD refinement of $Ba[BeSi_2N_4]$ with standard deviations in parentheses.

Formula	$Ba[BeSi_2N_4]$
Crystal system	Orthorhombic
Space group	*Ama*2 (no. 40)
Lattice parameters / Å	*a* = 8.1314(4), *b* =9.9947(6), *c* = 4.8017(3)
Cell volume / $Å^3$	390.24(4)
Z	4
Density / $g \cdot cm^{-3}$	4.401
Experimental absorption coefficient / cm^{-1}	10.611
F (000)	464
Crystal dimensions / µm	15 × 10 × 5
Diffractometer	Bruker D8 Venture
Radiation	Mo *K*α (λ = 0.71073 Å)
T / K	293(2)
Abs. correction	Multi-scan
θ range / °	4.078 – 39.211
Measured reflns	7593
Independent reflns (I < 2 σ(I))	1171 (1084)
Friedel fraction coverage	0.846
R_{int}, R_σ	0.0491, 0.0336
Refined parameters	43
Restraints	1
Flack	0.54(3)
R indices (I≥2*σ*(I))	*R*1 = 0.0227, *wR*2 = 0.0372
R indices (all data)	*R*1 = 0.0272, *wR*2 = 0.0379
GooF	1.152
$\Delta\rho_{max}$, $\Delta\rho_{min}$ / ($e \cdot Å^{-3}$)	1.233, -1.765

Table S77. Atomic coordinates and equivalent isotropic displacement parameters of $Ba[BeSi_2N_4]$ with standard deviations in parentheses.

Atom (*Wyck.*)	*x*	*y*	*z*	U_{eq} (A^2)	*sof*
Ba1 (4*b*)	1/4	0.44578(3)	0.05734(8)	0.00839(6)	1
Be2 (4*b*)	1/4	0.2233(6)	0.5257(18)	0.0056(13)	1
Si3 (8*c*)	0.05932(11)	0.16404(9)	0.01788(18)	0.00287(18)	1
N4 (4*b*)	1/4	0.6881(4)	0.3564(8)	0.0043(7)	1
N5 (4*a*)	0	0	0.0000(9)	0.0080(8)	1
N6 (8*c*)	0.0778(4)	0.2256(3)	0.3564(6)	0.0047(5)	1

Table S8. Selected bond lengths and angles in $Ba[BeSi_2N_4]$, symmetry operations labeled as (i) *x*, −0.5+*y*, −0.5+*z*; (ii) *x*, 0.5+*y*, −0.5+*z*; (iii) 0.5−*x*, *y*, *z*; (iv) 0.5−*x*, 0.5+*y*, 0.5+*z*; (v) *x*, 0.5+*y*, 0.5+*z*; (vi) 0.5−*x*, 0.5+*y*, −0.5+*z*; (vii) *x*, −0.5+*y*, 0.5+*z*; (viii) 0.5+*x*, 0.5−*y*, 0.5+*z*; (ix) −*x*, 0.5−*y*, 0.5+*z*; (x) −*x*, 0.5−*y*, −0.5+*z*; (xi) *x*, *y*, 1+*z*; (xii) −*x*, −*y*, *z*. Standard deviations in parentheses.

Bond name	**Bond length / Å**	**Bond name**	**Bond length / Å**
Ba1—N4^{i}	2.750(4)	Be2—N6	1.620(5)
Ba1—N4	2.816(4)	Be2—N6^{iii}	1.620(5)
Ba1—N6^{iii}	2.978(3)	Be2—N4^{vii}	1.626(10)
Ba1—N6	2.978(3)	Si3—N5	1.7111(10)
Ba1—N5^{iv}	2.991(3)	Si3—N6	1.745(3)
Ba1—N5^{v}	2.991(3)	Si3—N6^{x}	1.749(3)
Ba1—N6^{vi}	3.273(3)	Si3—N4^{i}	1.750(2)
Ba1—N6^{ii}	3.273(3)		
Angle name	**Angle / °**	**Angle name**	**Angle / °**
N6—Be2—N6^{iii}	119.7(6)	N6—Si3—N6^{x}	104.2(1)
N6—Be2—N4^{vii}	119.6(3)	N5—Si3—N4^{i}	111.06(17)
N5—Si3—N6	114.13(18)	N6—Si3—N4^{i}	106.75(17)
N5—Si3—N6^{x}	113.73(14)	Si3—N5—Si3^{xii}	174.3(3)

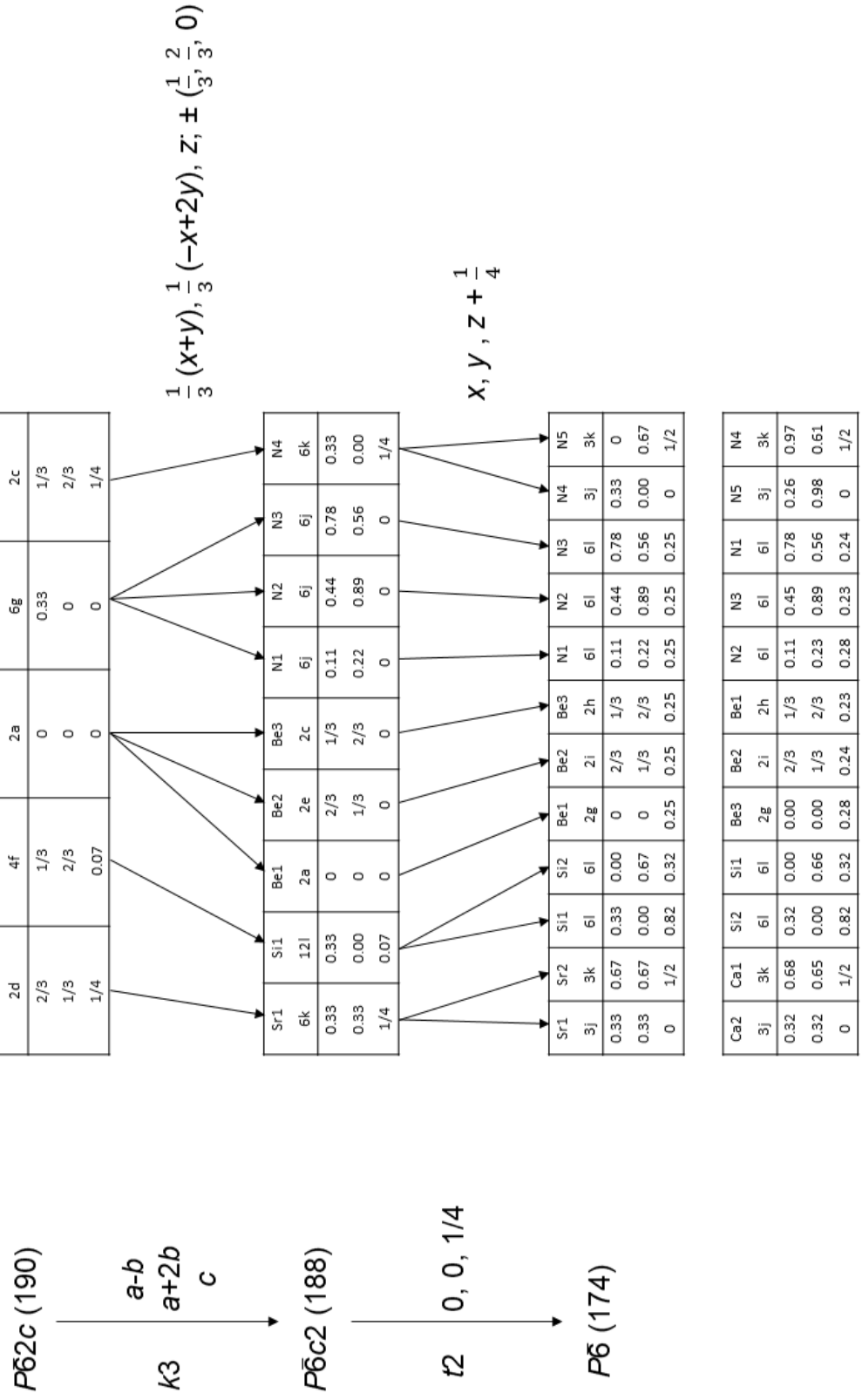

Figure S39. *Bärnighausen* tree of the symmetry descent from *P*6̄2*c* to *P*6̄. *Bärnighausen* tree and of the symmetry descent from *P*6̄2*c* to *P*6̄ and comparison of atomic coordinates between Sr[$BeSi_2N_4$] and Ca[$BeSi_2N_4$].

C.3 Scanning Electron Microscopy

Table S98. Energy dispersive X-ray spectroscopy (EDS) of $Ca[BeSi_2N_4]$. Eight sample points taken for elemental analysis. N was not quantified due to surface hydrolysis.

	1	2	3	4	5	6	7	8	Ø
Ca	1	1	1	1	1	1	1	1	1
Si	2.2	2.2	2.2	2.2	2.0	1.7	2.2	1.9	2.1

Table S10. Energy dispersive X-ray spectroscopy (EDS) of $Ba[BeSi_2N_4]$. Eight sample points taken for elemental analysis.

	1	2	3	4	5	6	7	8	Ø
Ba	1	1	1	1	1	1	1	1	1
Si	2.0	2.0	1.9	1.9	2.0	1.9	2.1	2.1	2.0
N	3.6	3.6	3.0	3.3	3.5	3.3	4.7	4.7	3.7

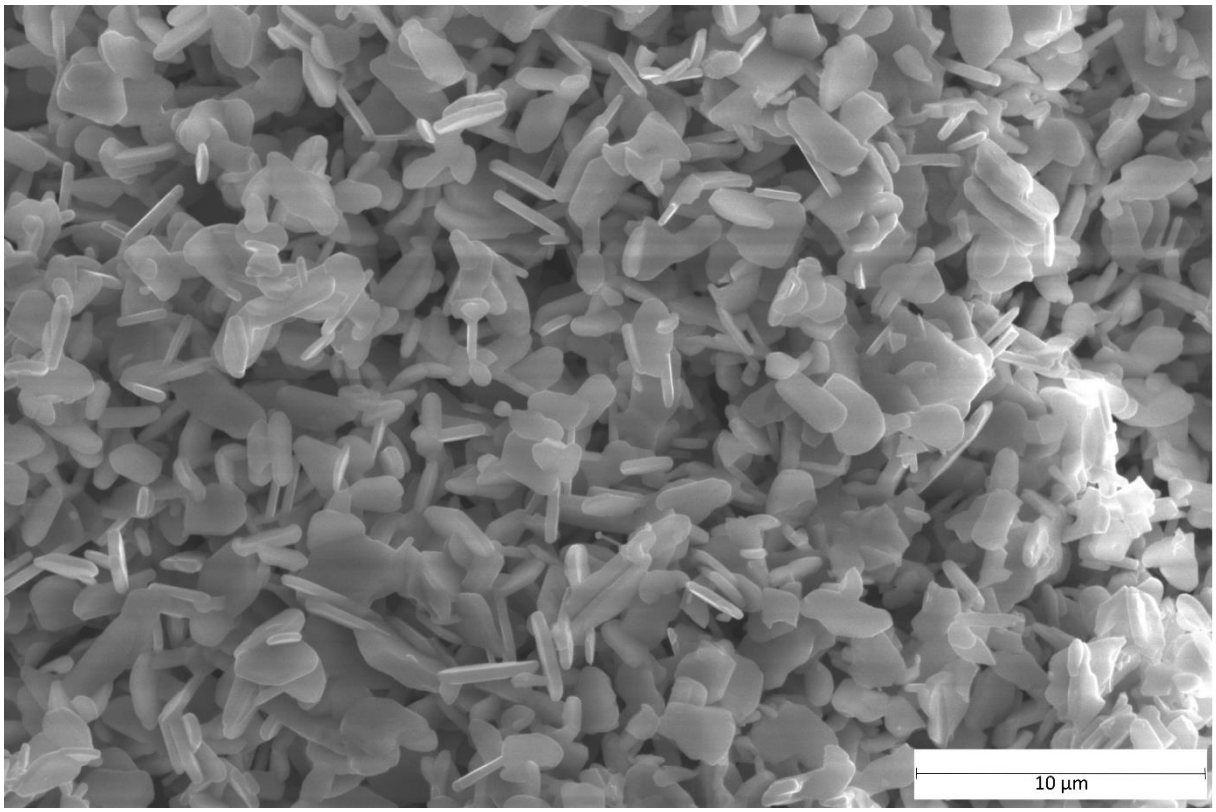

Figure S4. SEM image of crystal agglomerates of $Ba[BeSi_2N_4]$. Agglomerated crystals of $Ba[BeSi_2N_4]$ are shown at an acceleration voltage of 20 kV. The single crystallites have edge lengths in the range of micrometers and below.

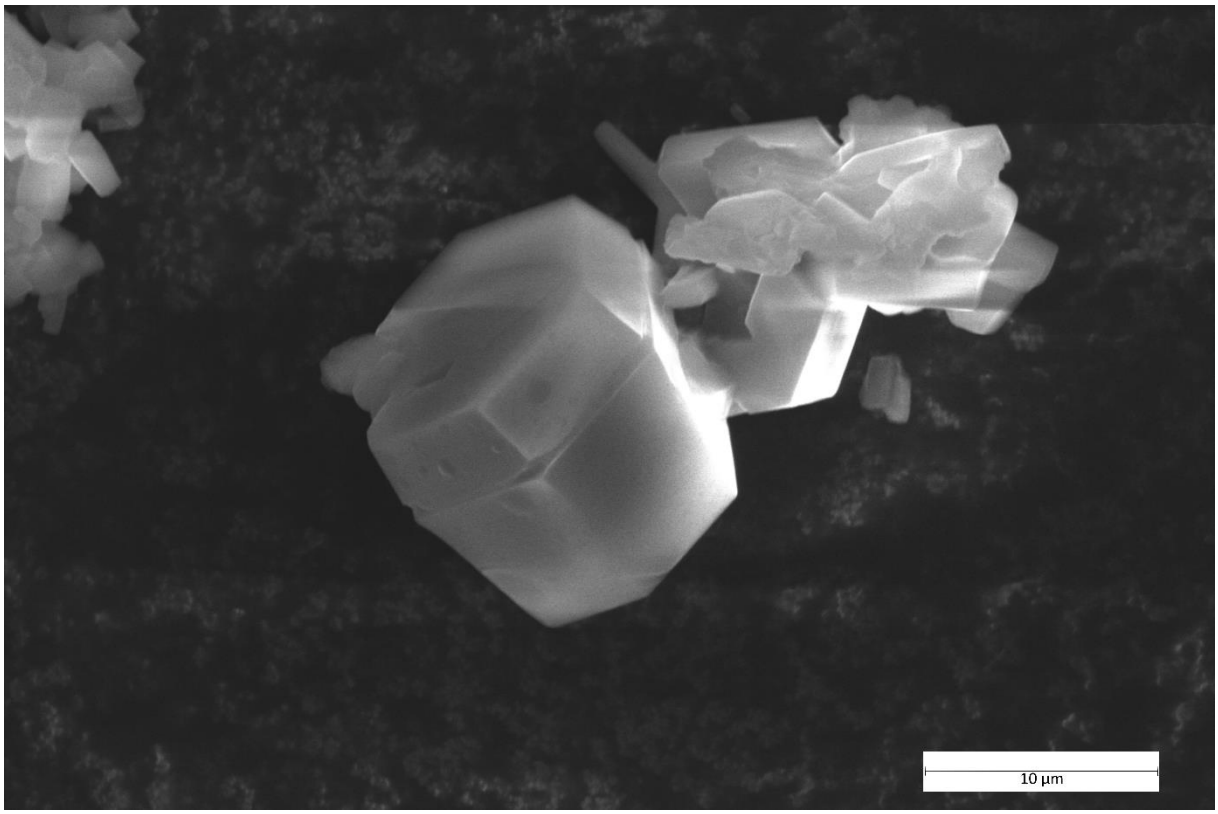

Figure S510. SEM image of crystal agglomerates of $Ca[BeSi_2N_4]$. Agglomerated crystals of $Ca[BeSi_2N_4]$ are shown at an acceleration voltage of 20 kV. The single crystallites have edge lengths in the range of several micrometers.

C.4 Luminescence

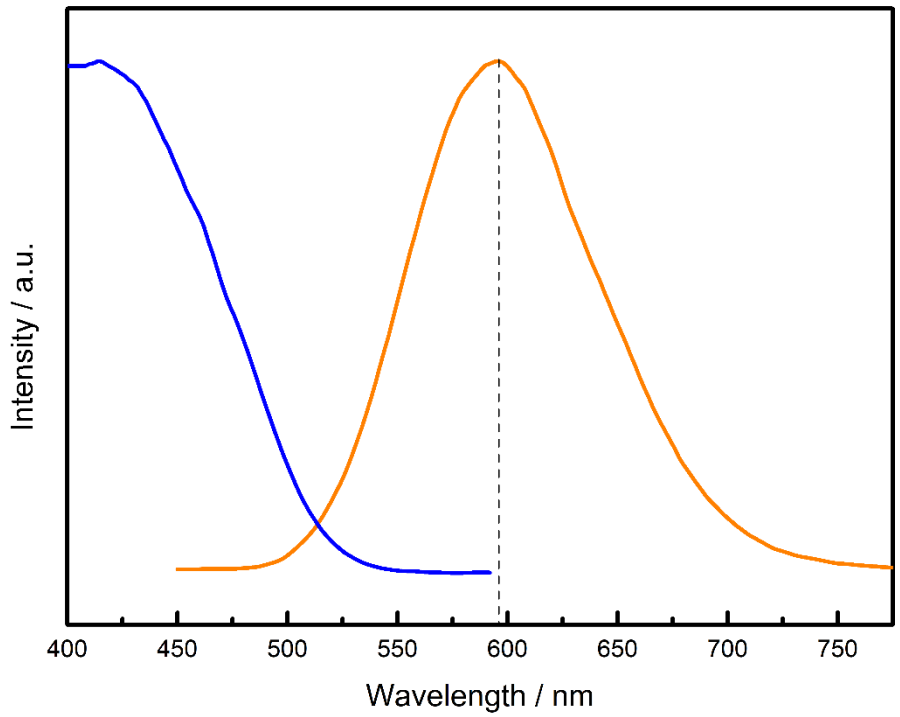

Figure S6. Luminescence plot of $Ba[BeSi_2N_4]:Eu^{2+}$. Excitation spectrum in blue, emission spectrum in orange. Maximum emission highlighted by the dashed black line.

D Supporting Information for Chapter 5

D.1 Elemental Analysis.

The elemental composition of $Sr_3Be_2O_5$ was determined by energy dispersive X-ray spectroscopy (EDS) on a Dualbeam Helios Nanolab G3 UC scanning electron microscope (SEM, FEI) with X-Max 80 SDD detector (Oxford Instruments). EDS data was obtained at an accelerating voltage of 20 kV from several particles.

Table S1. Elemental Analysis by energy dispersive X-ray spectroscopy (EDS) of $Sr_3Be_2O_5$

		1	2	3	4	Ø
$Sr_3Be_2O_5$	Sr	1	1	1	1	1
	O	1.7	1.9	1.6	1.9	1.8

D.2 X-ray Diffraction.

Single crystals of $Sr_3Be_2O_5:Eu^{2+}$ were selected and fixed on a glass filament. X-ray diffraction data was collected on a Bruker D8 Venture rotary anode diffractometer with Goebel mirror optics for selection and focussing of Mo-Kα radiation (λ = 0.71073 Å). APEX3 was used for integration and absorption correction. The crystal structures were solved by Direct Methods (SHELXS) and refined by full-matrix least-squares methods (SHELXL).

For powder X-ray diffraction the sample was ground and sealed in a glass capillary (Hilgenberg, *d* = 0.3 mm) and mounted on a rotary head of a STOE STADI P diffractometer (Cu $K\alpha_1$ radiation, Ge(111) monochromator, Mythen 1k detector) with modified Debye-Scherrer geometry. TOPAS 6 was used for crystal structure refinement by the Rietveld method.

Further details of the crystal structure investigations can be obtained from the Fachinformationszentrum Karlsruhe, 76344 Eggenstein-Leopoldshafen, Germany (Fax, (+49)7247-808-666; email, crysdata@fiz-karlsruhe.de) upon quoting the depository number CSD-1959979.

Table S2. Crystallographic data from SCXRD

	$Sr_3Be_2O_5:Eu^{2+}$
Formula mass [g mol^{-1}]	360.88
Crystal system / space group	Monoclinic, $P2_1/c$ (no. 14)
Lattice parameters [Å,°]	a = 3.7000(7)
	b = 9.600(2)
	c = 7.900(2)
	β = 99.00(3)
Cell volume [Å^3]	277.15(10)
Formula units per cell Z	2
X-ray density [g cm^{-1}]	4.324
Linear absorption coefficient [cm^{-1}]	28.699
F(000)	324
Crystal dimensions (mm^3)	0.02 × 0.01 × 0.01
Diffractometer	D8 Quest
Radiation	Mo-K_α (λ = 0.71073 Å)
Temperature [K]	297(2)
Abs correction	Multi-scan
θ range [°]	3.365 − 24.121
Measured reflns	5067
Independent reflns (I < 2 σ(I))	635 (606) [R_{int} = 0.0817]
Min./max. transmission	0.2788/1.000
Refined params	49
GooF	1.179
R indices (Fo2 ≥ 2σ(Fo2))	R1 = 0.0199, wR2 = 0.0462
R indices (all data)	R1 = 0.0213, wR2 = 0.0467
min./max. residual electron density (eÅ^{-3})	-1.288/0.793

Table S3. Atomic coordinates and equivalent isotropic displacement parameters of $Sr_3Be_2O_5:Eu^{2+}$

Atom (*Wyck.*)	*x*	*y*	*z*	U_{eq} (A^2)	*sof*
Sr1 (4e)	0.43613(9)	0.31897(3)	0.15501(5)	0.0074(2)	1
Sr2 (2a)	0	0	0	0.0050(2)	1
Be1 (4e)	0.8656(13)	0.1059(5)	0.3557(6)	0.0079(10)	1
O1 (4e)	0.5768(6)	0.0598(3)	0.2046(3)	0.0076(6)	1
O2 (4e)	0.0153(7)	0.7604(3)	0.1181(4)	0.0106(6)	1
O3 (2c)	0	1/2	0	0.0191(10)	1

Table S4. Selected bond lengths and angles in $Sr_3Be_2O_5:Eu^{2+}$

Bond name	**Bond length / Å**	**Bond name**	**Bond length / Å**
Sr1—O3	2.5505(6)	Sr2—O2^{iv}	2.480(2)
Sr1—O2^{i}	2.555(2)	Sr2—O2	2.480(2)
Sr1—O1^{ii}	2.560(2)	Sr2—O1^{iv}	2.486(2)
Sr1—O1^{iii}	2.567(2)	Sr2—O1	2.486(2)
Sr1—O2^{iv}	2.623(2)	Sr2—O1^{viii}	2.532(2)
Sr1—O2^{iii}	2.692(2)	Sr2—O1^{ii}	2.532(2)
Sr1—O3^{ii}	3.1101(6)	O1—Be1^{ix}	1.548(4)
		O2—Be1^{x}	1.549(4)

Angle name	**Angle / °**	**Angle name**	**Angle / °**
O1—Be1—O3	118.892	O2^{iii}—Sr2—O1	89.76(7)
O2—Be1—O3	118.895	O2^{ix}—Sr2—O1	90.24(7)
O1—Be1—O2	121.554	O1^{x}—Sr2—O1	84.99(7)
O2^{iii}—Sr2—O2^{ix}	180.00(4)	O1^{xi}—Sr2—O1	95.01(7)
O2^{iii}—Sr2—O1^{x}	87.05(7)	O2^{iii}—Sr2—O1^{xii}	90.24(7)
O2^{ix}—Sr2—O1^{x}	92.95(7)	O2^{ix}—Sr2—O1^{xii}	89.76(7)
O2^{iii}—Sr2—O1^{xi}	92.95(7)	O1^{x}—Sr2—O1^{xii}	95.01(7)
O2^{ix}—Sr2—O1^{xi}	87.05(7)	O1^{xi}—Sr2—O1^{xii}	84.99(7)
O1^{x}—Sr2—O1^{xi}	180.00(13)	O1—Sr2—O1^{xii}	180.000

Table S5. Crystallographic data from PXRD

	$Sr_3Be_2O_5$
Formula mass [g mol^{-1}]	360.88
Crystal system / space group	Monoclinic, $P2_1/c$ (no. 14)
Lattice parameters [Å,°]	a = 3.70237(6)
	b = 9.6069(2)
	c = 7.9004(1)
	β = 99.0076(4)
Cell volume [Å^3]	277.539(8)
Formula units per cell Z	2
X-ray density [g cm^{-1}]	4.2227(1)
Linear absorption coefficient [cm^{-1}]	364.53(1)
Radiation	Cu-$K_{\alpha1}$ (λ = 1.5406 Å)
Temperature	293(2)
2θ range [°]	5.000 − 106.820
Number of data points	6789
Number of observed reflections	333
Number of parameters	46, thereof 12 background
GooF	2.2073
R_{wp}	0.0717
R_{exp}	0.0324
R_P	0.0531
R_{Bragg}	0.0486

E Supporting Information for Chapter 6

E.1 Experimental Details

High-temperature synthesis

Due to their moisture sensitivity and toxicity, the starting materials, S (GRÜSSING, sublimed *in vacuo*), Be (abcr, 99+%, 325 mesh) and Na_2S (ALFA AESAR, 99%) were handled under argon atmosphere in a glovebox (Unilab, MBraun, Garching, < 0.1 ppm H_2O, O_2). All starting materials were ground in a tungsten carbide mortar and filled in a boron nitride crucible (Henze, Kempten). The crucible was sealed in an argon filled quartz ampule. The ampule was heated with 25 K/h in a tube furnace to 600 °C. This temperature was maintained for 72 h. Subsequently, the specimen was cooled down by shutting down the furnace. Na_2BeS_2 was obtained as a pale yellow, moisture and air sensitive powder.

Single-crystal X-ray diffraction (SCXRD)

Single crystals of Na_2BeS_2 were isolated in a capillary (Hilgenberg, Malsfeld) under paraffin. The single-crystal X-ray diffraction data were collected on a Bruker D8 Venture TXS diffractometer (Mo-Kα radiation, λ = 0.71073 Å, rotating anode, multilayer monochromator) by performing a combination of ω- and φ-scans. The corresponding APEX 3 software-package was used for indexing and integration, as well as multi-scan semi-empiric absorption correction. [1,2]

The resulting structure was solved and refined with SHELX-97 in the WinGX software package. Hereby, the structure solution was based on direct methods and refined against F^2 by the full-matrix least-square method. [3–5]

Diamond 3 and VESTA were used for structure visualization. [6,7]

Powder X-ray diffraction (PXRD)

Samples of Na_2BeS_2 were ground in a tungsten carbide mortar, sealed in glass capillaries (0.5 mm, Hilgenberg, Malsfeld) and mounted on the rotary head of a STOE Stadi P diffractometer (STOE & Cie GmbH, Darmstadt, Cu-$K\alpha_1$ radiation, λ = 1.5406 Å, Ge(111) monochromator). Data was collected in modified Debye-Scherrer geometry with a MYTHEN 1K Si strip detector.

TOPAS 6 Academic software was used for Rietveld refinement. Herein the background was accounted by a shifted Chebyshev polynomial and peak profiles were described by pseudo-Voigt-terms that were modeled based on a fundamental parameters approach. Possible preferred crystal orientation was described by a spherical harmonics function of sixth order. [8-11]

Electrochemical analysis

The sample was ground thoroughly prior to measurement and compacted by uniaxial cold pressing (1000 MPa/2 t) to a pellet of about 0.785 mm thickness, 5 mm diameter with a relative pellet density of 83.9%. Platinum was sputtered onto the pellet with a Quorum Q150 GB to enhance electrode/sample-contact. No reactions were observed between Pt and the sample.

Electrochemical Impedance Spectroscopy (EIS) and Chronopotentiometry (CP) were performed using an Ivium compactstat.h and a TSC SW closed impedance cell from rhd instruments kept under argon. EIS was performed in a two-electrode setup, while CP was performed in a pseudo-four-electrode setup. All measurements were conducted at a pressure of 720 kPa.

For the impedance measurement, an AC voltage of 100 mV was applied. Impedance measurements were carried out between 3 MHz and 0.5 Hz in a temperature range between 25 °C and 75 °C to determine the activation energies using the Arrhenius equation. The impedance spectra were analyzed using the RelaxIS3 software from rhd instruments.

For the CP measurement, a current of 5 nA was applied before the current was switched off again.

E.2 Results and Discussion

Structure determination

SCXRD

Table S1. Crystallographic data of SCXRD of Na_2BeS_2. Standard deviations are given in brackets.

Formula	**Na_2BeS_2**
Crystal system	orthorhombic
Space group	*Ibam* (no. 72)
Molecular weight / g·mol^{-1}	119.11
Lattice parameters / Å	a = 6.0015(4)
	b = 11.1701(7)
	c = 5.5179(4)
Cell volume / Å^3	369.91(4)
Formula units per cell	4
Calculated X-ray density / g·cm^{-3}	2.139
Linear absorption coefficient / cm^{-1}	1.406
T_{min}/ T_{max}	0.718
Radiation	Mo-Kα (λ = 0.71073 Å)
Diffractometer	Bruker D8 Venture
θ-range / °	3.648< θ < 31.433
Temperature / K	293(2)
F(000)	232
Observed reflections	2099
Independent reflections (> 2σ)	336 (290)
Number of parameters	16
R_{int}; R_σ	0.0596; 0.0438
Final R indices [I > 2 σ(I)]	R1 = 0.0305; wR2 = 0.0445
Final R indices (all data)	R1 = 0.0369; wR2 = 0.0462
Goodness of fit (GooF)	1.099
Residual electron density / e·Å^{-3}	0.52; −0.348

Table S2. SCXRD refined atom coordinates and equivalent isotropic atomic displacement parameters. Standard deviations are given in brackets.

Atom	Position	*x*	*y*	*z*	U_{eq} / Å²
S1	8j	0.19157(8)	0.39560(4)	1/2	0.01178(13)
Na2	8j	0.16471(15)	0.14518(8)	1/2	0.0196(2)
Be3	4b	0	1/2	1/4	0.0133(7)

Table S3. SCXRD refined anisotropic atomic displacement parameters (Å^2). Standard deviations are given in brackets.

Atom	U_{11}	U_{22}	U_{33}	U_{23}	U_{13}	U_{12}
S1	0.0128(2)	0.0119(2)	0.0106(2)	0	0	0.0038(2)
Na2	0.0200(4)	0.0181(4)	0.0207(5)	0	0	0.0025(3)
Be3	0.0137(16)	0.0148(15)	0.0114(17)	0	0	0

Table S4. Interatomic distances of Na_2BeS_2 (Å). Standard deviations are given in brackets.

Be3–S1	2.1412(4)	Na2–S1	2.9182(10)	Na2–Be3	2.9295(8)
Na2–S1	2.8019(10)	Na2–S1	2.9263(4)	Na2–Be3	2.9295(8)
Na2–S1	2.8758(10)	Na2–S1	2.9263(4)	Na2–S1	3.1946(10)

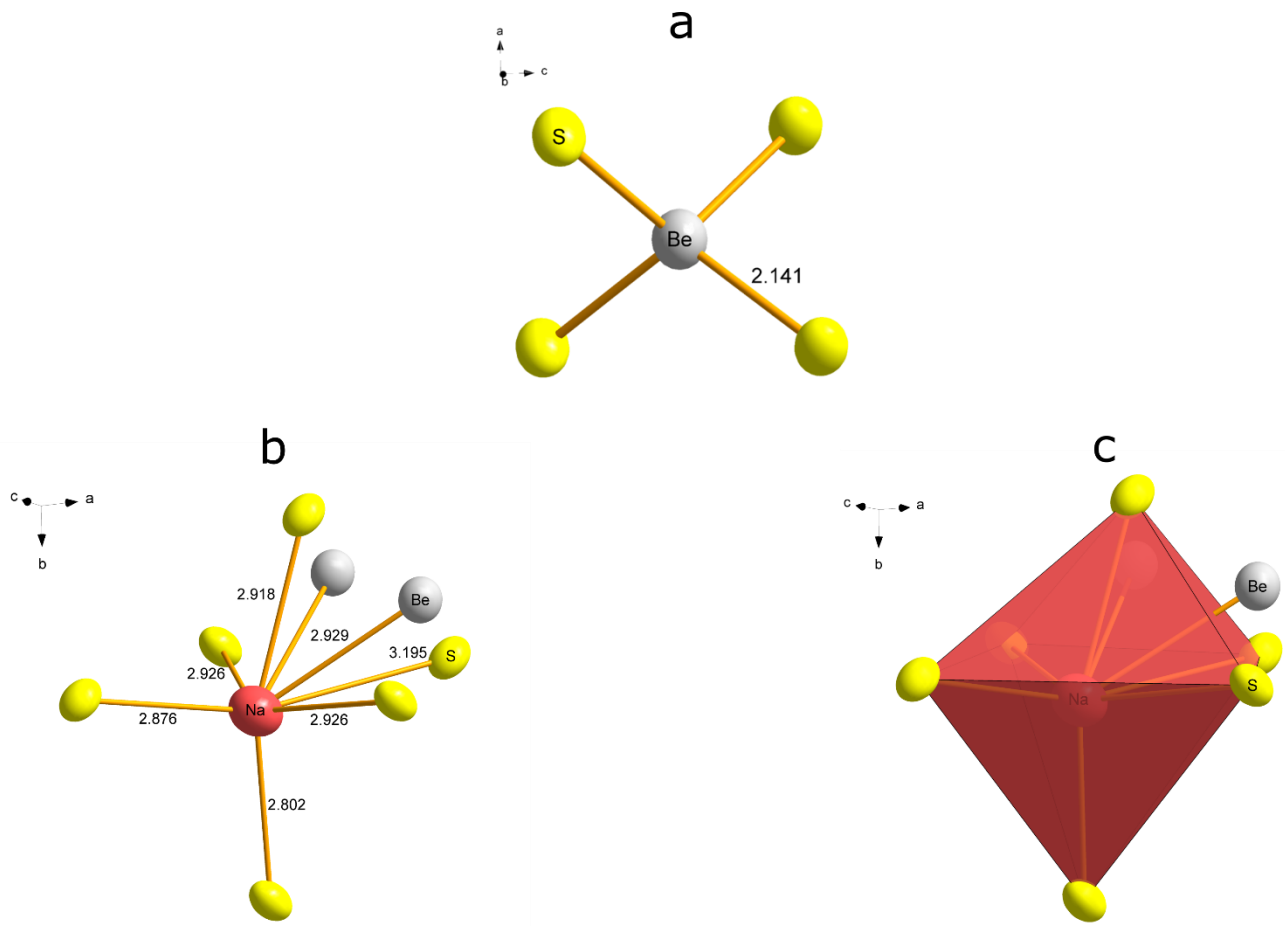

Figure S1. Interatomic distances (Å) and coordination polyhedra of Na_2BeS_2. Ellipsoids are displayed at 95% probability level. **a** Tetrahedral coordination of Be by S **b** 5+2+1 coordination of Na by S and Be **c** Distorted octahedron of S in Na coordination sphere.

Rietveld refinement

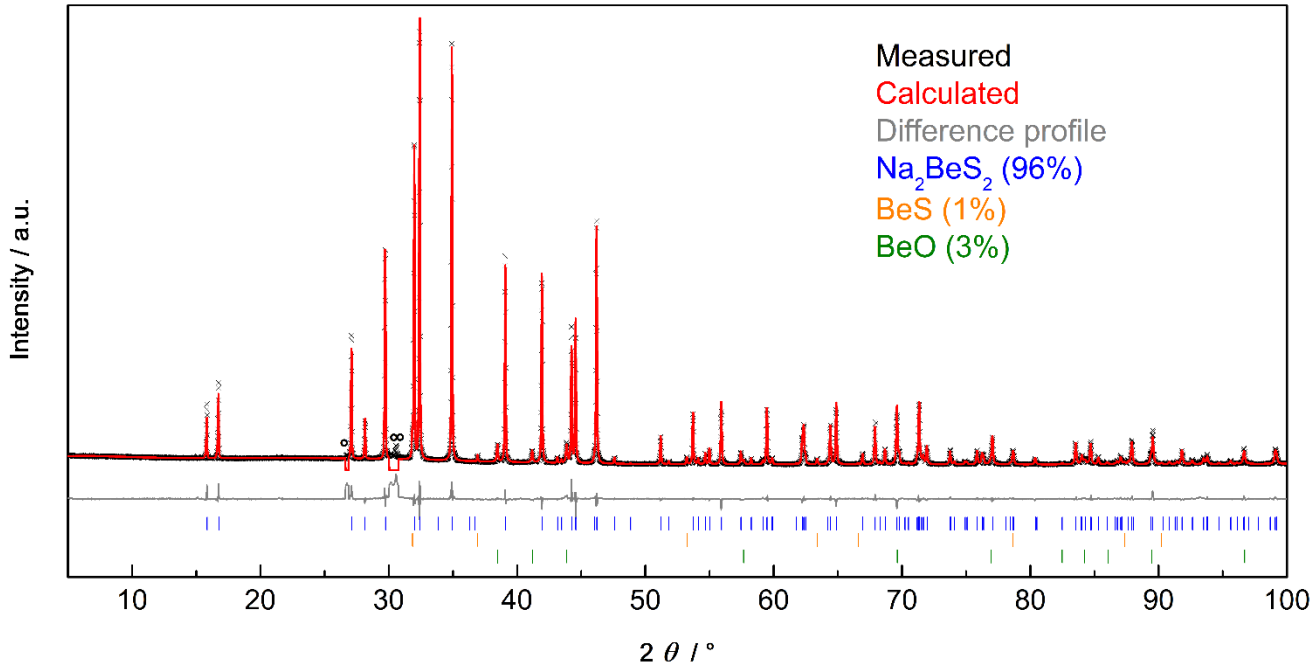

Figure S2. Measured (black crosses) as well as calculated (red line) PXRD data and difference profile (gray) from Rietveld refinement of Na_2BeS_2. All identified Bragg reflections are marked by vertical lines. Reflections of an unidentified, minor side phase are tagged (°). The residual difference is due to the profile fit, since the profile resulting of small domains is not fitted perfectly. Details in Table S5.

Table S5. Detailed crystallographic data of the Rietveld refinement of Na_2BeS_2.

Formula	**Na_2BeS_2**
Crystal system	orthorhombic
Space group	*Ibam* (no. 72)
Lattice parameters / Å	a = 6.00133(3) b = 11.17358(5) c = 5.51616(2)
Cell volume / Å^3	369.894(3)
Formula units per cell	4
Calculated X-ray density / g·cm^{-3}	2.13906(2)
Linear absorption coefficient / cm^{-1}	131.822(1)
Radiation	Cu-Kα_1 (λ = 1.540596 Å)
Monochromator	Ge(111)
Diffractometer	STOE Stadi P
Detector	MYTHEN 1K
2θ-range	5° < 2θ < 101°
Temperature / K	293
Data points	6432
Number of observed reflections	112
Number of parameters (thereof background)	43(12)
Profile function	fundamental parameter approach[14]
Background function	Shifted Chebyshev
R indices	R_{Bragg} = 0.02444 R_p = 0.03580 R_{wp} = 0.09487 R_{exp} = 0.02546
Goodness of fit	1.930

Calculation of MAPLE values

Table S6. The calculation of MAPLE values shows a 1.7% difference in the Madelung part of lattice energy of the sum of the respective binary sulfides Na_2S and BeS to the target phase Na_2BeS_2.[12]

	Na_2S + BeS	→	Na_2BeS_2	
Na_2S:	2472 kJ·mol^{-1}		Na_2BeS_2:	6680 k J·mol^{-1}
BeS:	4322 kJ·mol^{-1}			
	6794 kJ·mol^{-1}			**1.7% difference**

Crystal structure comparison

The crystal structure of Na_2BeS_2 was compared to the structure of K_2SiP_2 based on the method of G. Bergerhoff. [13,14]

Wyckoff Position	**General Coordinates**	**Atom 1**	**Atom 2**
4b	(1/2,0,1/4)	Be	Si
8j	(*x*,*y*,0)	S	P
8j	(*x*,*y*,0)	Na	K

Chronopotentiometry

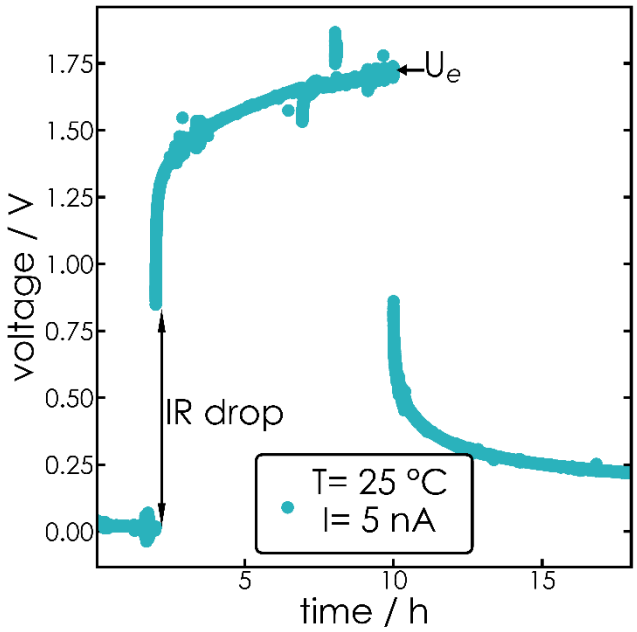

Figure S3: Room temperature chronopotentiometry measurement of the Na_2BeS_2 sample (d=0.785) using a current of 5 nA. The IR drop and the saturation voltage U_e are annotated.

To separate the ionic and electronic contribution to the total conductivity, CP was measured with blocking electrodes (c.f. Figure S3). Therefore, after an initial open-circuit potential phase (I=0 A), a current of 5 nA was applied for 8 h (data points were collected every 0.2 s). Even after this time, the sample did not reach a steady state, rendering the determined electronic conduction an upper limit. The electronic and total conductivities of the sample can be calculated using equation 1 and 2, respectively.

$$\sigma_{eon} = \frac{1}{R_{eon}}\frac{d}{A} \; with \; R_{eon} = \frac{U_e}{I} \qquad \text{(Eq. 1)}$$

$$\sigma_{total} = \frac{1}{R_{IR}}\frac{d}{A} \; with \; R_{IR} = \frac{U_{IR}}{I} \qquad \text{(Eq. 2)}$$

From these values, the ionic conductivity can be calculated by equation 3:

$$\sigma_{ion} = \sigma_{total} - \sigma_{eon} \qquad \text{(Eq. 3)}$$

Description of the Equivalent Circuit

The equivalent circuit used to fit the impedance data is shown in Figure 2. It consists of a resistor and constant phase element (CPE) in series, connected to a CPE and to another resistor. The resistor and CPE in series represent the ionic conduction process, the single resistor represents the resistance of the electronic conduction process and the single CPE is the geometrical capacitance. Unlike other equivalent circuits used to fit ionic conductors, there is no low frequency tail because the interface resistance is bridged by the electronic current.

Transference number

The ionic transference number is calculated according to equation 4 using the conductivity values obtained by EIS:[15]

$$t_{ion} = \frac{\sigma_{ion}}{\sigma_{ion}+\sigma_{eon}} = \frac{3.3\cdot10^{-9}}{3.3\cdot10^{-9}+1.6\cdot10^{-9}} = 0.67 \qquad \text{(Eq. 4)}$$

E.3 References

[1] BrukerAXS, Billerica, **2016**.

[2] XPREP Reciprocal Space Exploration, Vers. 6.12, Bruker-AXS, Karlsruhe, **2001**.

[3] G. M. Sheldrick, University of Göttingen **1997**.

[4] G. M. Sheldrick; A short history of SHELX, *Acta Crystallogr. Sect. A* **2008**, *64*, 112, doi:10.1107/S0108767307043930.

[5] L. J. Farrugia; WinGXsuite for small-molecule single-crystal crystallography, *J. Appl. Crystallogr.* **1999**, *32*, 837, doi:10.1107/s0021889899006020.

[6] G. Bergerhoff, M. Berndt and K. Brandenburg; Evaluation ofCrystallographic Data with the Program DIAMOND, *J. Res. Natl. Inst. Stand. Technol.* **1996**, *101*, 221.

[7] K. Momma and F. Izumi; VESTA 3 for three-dimensional visualization of crystal, volumetric and morphology data, *J. Appl. Crystallogr.* **2011**, *44*, 1272, doi:10.1107/S0021889811038970.

[8] H. M. Rietveld; A profile refinement method for nuclear and magnetic structures, *J. Appl. Crystallogr.* **1969**, *2*, 65, doi:10.1107/s0021889869006558.

[9] A. A. Coelho, 4.1 ed., Brisbane, Australia, **2007**.

[10] R. W. Cheary and A. Coelho; A fundamental parameters approach to X-ray line-profile fitting, *J. Appl. Crystallogr.* **1992**, *25*, 109, doi:10.1107/s0021889891010804.

[11] R. W. Cheary, A. A. Coelho and J. P. Cline; Fundamental Parameters Line Profile Fitting in Laboratory Diffractometers, *J. Res. Natl. Inst. Stand. Technol.* **2004**, *109*, 1, doi:10.6028/jres.109.002.

[12] R. Hoppe; On the Madelung Part of Lattice Energy, *Zeitschrift für Naturforschung A* **1995**, *50*, 555, doi:10.1515/zna-1995-0607.

[13] B. Eisenmann and M. Somer; K_2SiP_2, ein Phosphidopolysilikat(IV), *Z. Naturforsch., B: Chem. Sci.* **1 984**, *39*, 736.

[14] G. Bergerhoff, M. Berndt, K. Brandenburg and T. Degen; Concerning inorganic crystal structure types, *Acta Crystallogr. Sect. B: Struct. Sci.* **1999**, *55*, 147, doi:10.1107/s0108768198010969.

[15] R. A. Huggins; Simple method to determine electronic and ionic components of the conductivity in mixed conductors a review, *Ionics* **2002**, *8*, 300, doi:10.1007/bf02376083.

F Miscellaneous

F.1 List of Publications, Manuscripts and Patents

The following list contains all publications, patents and manuscripts of this thesis including authors, author contributions and (if applicable) citations.

1. Synthesis and Crystal Structure of the Strontium Beryllate $Sr_3Be_2O_5$

Tobias Giftthaler, *Philipp Strobel and Wolfgang Schnick*

Zeitschrift für anorganische und allgemeine Chemie, **2019**

DOI: 10.1002/zaac.201900281

T.G., P.S. and W.S. conceived and designed the project. T.G. conducted the majority of experimental work. The data were measured and analyzed by T.G., P.S. and W.S.. All authors discussed the results and took part in producing the manuscript.

2. Green-Emitting Oxonitridoberyllosilicate $Ba[BeSiON_2]:Eu^{2+}$ for Wide Gamut Displays

Tobias Giftthaler, *Philipp Strobel, Volker Weiler, Arthur Haffner, Andreas Neuer, Jennifer Steinadler, Thomas Bräuniger, Simon D. Kloß, Stefan Rudel, Peter J. Schmidt and Wolfgang Schnick*

Advanced Optical Materials, **2023**

DOI: 10.1002/adom.202302343

T.G., P.S., P.J.S. and W.S. conceived and designed the project. T.G. conducted the majority of experimental work with significant help from A.N., P.S., S.R. and J.S.. The data were measured and analyzed by T.G., P.S., V.W., A.H., J.S., T.B., S.D.K., S.R., P.J.S. and W.S.. All authors discussed the results and took part in producing the manuscript.

3. Blue Emitting $SrBe_{1-x}Si_{2+x}O_{3-2x}N_{2-2x}:Eu^{2+}$ ($x \approx 0.1$)

Tobias Giftthaler, *Marwin Dialer, Philipp Strobel, Peter J. Schmidt and Wolfgang Schnick*

Zeitschrift für anorganische und allgemeine Chemie, **2023**

DOI: 10.1002/zaac.202300208

T.G., M.D., P.S., P.J.S. and W.S. conceived and designed the project. T.G. and M.D. conducted the majority of experimental work. The data were measured and analyzed by T.G., M.D., P.S., P.J.S. and W.S.. All authors discussed the results and took part in producing the manuscript.

4. Introducing Ternary Thioberyllates – Na_2BeS_2

Tobias Giftthaler, *Robert Calaminus, Sascha Harm, Bettina V. Lotsch and Wolfgang Schnick*

Published as part of this thesis

T.G., R.C., S.H., B.V.L. and W.S. conceived and designed the project. T.G. and R.C. conducted the majority of experimental work. The data were measured and analyzed by T.G., R.C., S.H., B.V.L. and W.S.. All authors discussed the results and took part in producing the manuscript.

5. The Nitridoberyllosilicate System *AE*$BeSi_2N_4$ (*AE* = Ca, Ba)

***Tobias Giftthaler**, Lucien Eisenburger, Philipp Strobel, Oliver Oeckler and Wolfgang Schnick*

Published as part of this thesis

T.G., L.E., P.S., O.Oe. and W.S. conceived and designed the project. T.G., P.S. and L.E. conducted the majority of experimental work. The data were measured and analyzed by T.G., L.E., P.S., O.Oe. and W.S.. All authors discussed the results and took part in producing the manuscript.

6. Oxonitridoberyllosilicate Phosphors

***Tobias Giftthaler**, Philipp Strobel, Peter J. Schmidt, Hans-Helmut Bechtel and Wolfgang Schnick*

Patent granted
PCT/US2022/049598

T.G., P.S., P.J.S. and W.S. conceived and designed the project. T.G. conducted the majority of experimental work with significant help from P.S.. and H.-H.B.. The data were measured and analyzed by T.G., P.S., H.-H.B., P.J.S. and W.S.. All authors discussed the results and took part in the patent draw.

F.2 Publication beyond this Thesis

Understanding of Luminescence Properties Using Direct Measurements on Eu^{2+}-Doped Wide Bandgap Phosphors

Muhammad Ruhul Amin, Philipp Strobel, Amir Qamar, Tobias Giftthaler, Wolfgang Schnick, Alexander Moewes

Advanced Optical Materials, **2020**

DOI: 10.1002/adom.202000504

F.3 Conference Contributions and Presentations

Irgendwas mit Beryllium

Tobias Giftthaler, and Wolfgang Schnick

Talk, 5. Obergurgl-Seminar für Festkörperchemie, **2020**, Obergurgl, Austria

Be Green Lantern

Tobias Giftthaler, and Wolfgang Schnick

Talk, 6. Obergurgl-Seminar für Festkörperchemie, **2023**, Obergurgl, Austria

Nitridoberyllosilicates – Promising Host Materials for Solid-state Lighting

Tobias Giftthaler, Philipp Strobel, Lucien Eisenburger, Oliver Oeckler and Wolfgang Schnick

Talk and Poster, International Symposium on Nitrides, **2019**, Barcelona, Spain

F.4 Deposited Crystallographic Data

The Crystallographic Information Files (CIFs) of all compounds introduced in this thesis are deposited at and provided free of charge by the joint Cambridge Crystallographic Data Centre and Fachinformationszentrum Karlsruhe All data can be obtained quoting the respective depository number.

Table F.1. List of compounds that are introduced within this thesis with corresponding depository number.

Compound	**CSD**
$BaBeSiON_2$	2191356
$SrBeSi_2O_3N_2$	2291214
$CaBeSi_2N_4$	2305744
$BaBeSi_2N_4$	2305743
$Sr_3Be_2O_5$	1959979
Na_2BeS_2	2302593